



RETURNING MATERIALS:  
Place in book drop to  
remove this checkout from  
your record. FINES will  
be charged if book is  
returned after the date  
stamped below.

--	--	--

STRUCTURAL AND DYNAMICAL STUDIES  
OF  
LAYERED SOLIDS

BY

YIBING FAN  
B.S., Peking University, 1983

DISSERTATION

Submitted to partial fulfillment of the requirements for  
the degree of Doctor of Philosophy in Physics  
in Michigan State University, 1988

East Lansing, Michigan

536890X

ABSTRACT

STRUCTURES AND DYNAMICS STUDIES  
OF LAYERED SOLIDS

YiBing Fan, Ph.D.

Department of Physics and Astronomy, 1988

The structural and dynamical properties of graphite intercalation compounds and vermiculate clays intercalated with trimethylammonium were studied by x-ray scattering, elastic, inelastic and quasi-elastic neutron scattering.

We have measured the in-plane and c-axis elastic neutron scattering from the ternary potassium-ammonia graphite intercalation compound  $K(ND_3)_{4.3}C_{24}$  at room temperature. The c-axis scans establish that the graphite layers stack in an eclipsed configuration and that there is no correlation between the intercalant layers. The in-plane diffuse scattering from the intercalant layers is well accounted for by a computer-generated structural model in which each potassium ion is symmetrically 4-fold coordinated to ammonia molecules to form closely-packed, five-membered clusters. This model had been previously applied to explain the in-plane diffuse X-ray scattering results from  $K(NH_3)_{4.38}C_{24}$ . Discrepancies between the calculated and measured diffraction patterns are attributed to a relaxation of the 4-fold symmetry of the K-ND<sub>3</sub> clusters.

The results of an inelastic neutron scattering study of the [001] L lattice dynamics of stage-1 potassium-ammonia graphite compounds  $K(ND_3)_x C_{24}$

with  $x = 3.1$  and  $4.3$  are presented in chapter III. The results show that a librational mode splits the acoustic phonon branch of these compounds at an energy of 7 meV. The mechanisms of this coupling are discussed based on a force constant model and the split phonon dispersion curves are described by a linear chain model coupled with a transverse rotational oscillation of the potassium-ammonia complex. In addition, the interlayer force constants in the compound are found to be appreciably softer than in the stage-2 binary counterpart.

The quasi-elastic neutron scattering results for  $K(NH_3)_x C_{24}$ , which show the coexistence of molecular rotational and translational diffusion of the ammonia are reported in chapter IV.

For clays, neutron scattering has been used to study the basal spacing and vibrational excitations of high oriented samples of  $(CH_3)_3NH^+$ -Vermiculite and its deuterated form  $(CD_3)_3ND^+$ -vermiculite. Both forms exhibit a basal spacing of  $12.71\text{\AA}$  and a rich vibrational spectrum in the range 20-140 meV for Q perpendicular and parallel to the c-axis. Peaks at 28 and 37 meV are assigned as torsional modes of the methyl group, while the peak at 51 meV is identified as a  $\delta(C_3N)$  bending mode. The peaks above 80 meV are assigned as the inplane optical modes of the silicate sheet. These results are compared with infrared measurements over the same energy range and a good agreement is obtained.

## Acknowledgements

It was very joyful for me to spend my last 5 years at Michigan State University. Many people have made significant contributions to the successful completion of this thesis. Some, however, are deserving of special mention.

First of all, my advisor, Stuart A. Solin, has spent countless hours with me over the past five years for which I am very grateful. He introduced me to this research field and his rich experiences guided me through every stage of this work. I truly appreciated his frank criticisms and other generous help in the time of need.

I would like to thank my colaborator Dr. D.A. Neumann who has taught me a great deal about neutron scattering. I have also appreciated his generous hospitality and his guidance during my visits to the National Bureau of Standards for neutron scattering experiments.

I have benefited much from working with my fellow students who have worked in Dr. Solin's group over the years. Xiao-wen Qian has made special contributions to my understanding of x-ray scattering and of physics when I first joined the group. Yiyun Huang has always been helpful whenever I need a favor, and was particularly helpful with sample preparation. I also thank S. Lee, and P. Zhou for many interesting discussions.

The clay sample for chapter V were made in Professor Pinnavaia's laboratory. I really appreciated H. Kim's patience in helping me synthesize the clay samples.

Interactions with those people mentioned above made my stay at Michigan State University very joyful and this author will remember my MSU years for a long time to come.

Finally, research is not free. Financial support from the National Science Foundation under grant DMR-85-17223 and from the MSU Center for Fundamental Materials Research are also acknowledged.

## Table of Contents

Chapter I. Overview.....	1
1.1 Graphite Intercalation Compounds.....	1
1.2 Neutron Scattering.....	14
1.3 Neutron Scattering Instruments.....	26
References.....	37
Chapter II. Elastic Neutron Scattering Studies of the Structure of Graphite Intercalated with Potassium and Ammonia.....	40
2.1 Introduction.....	40
2.2 EXperimental Methods and Results.....	42
2.3 Calculations and Analysis.....	50
2.4 The Structural Model.....	57
2.5 Calculating the Diffraction Pattern.....	60
2.6 Summary and Conclusions.....	66
References.....	68
Chapter III. Inelastic Neutron Scattering Study of Stage 1 and Stage 2 K-Ammonia Intercalated Graphite.....	70
3.1 Introduction.....	70
3.2 Experiment and Results.....	72
3.3 Discussions.....	82
3.4 Conclusions.....	98
References.....	99
Chapter IV. Quasielastic Neutron Scattering Study of Rotations and Diffusion in Stage 1 K-Ammonia Intercalated Graphite.....	102
4.1 Introduction.....	102
4.2 Translational Diffusive Motion.....	102
4.3 Translational Jump Diffusion.....	103

4.4	Rotational Jump Diffusion.....	106
4.5	General Case.....	110
4.6	Experiment.....	111
4.7	Results and Discussions.....	112
	References.....	126
Chapter V. Neutron Scattering Studies of Trimethylammonium Vermiculite Clay Intercalation Compounds.....		
5.1	Introduction.....	129
5.2	Experiments.....	132
5.3	Results and Discussions.....	137
	Elastic Scattering.....	137
	Inelastic Scattering.....	147
5.4	Conclusions.....	152
	References.....	153

## Chapter I. OVERVIEW

For last two decades, one of the major themes of condensed matter physics has been the study of the low dimensional, particularly two-dimensional, phenomena. To explore the fascination of two-dimensional physics, many efforts have been made on layered materials, such as superlattices, graphite intercalation compounds, boron nitride, transition metal dichalcogenides, and layered silicates. As a matter of fact, advances in the synthesis of layered materials have led to many exciting discoveries, including the Quantum Hall Effect<sup>1</sup> for which Klaus von Klitzing won the 1985 Nobel prize in physics. Additionally, the anisotropy of layered solids enriched the study of effects of dimensionality in physics. In fact, most efforts have centered around the dimensional cross-over phenomena, i.e., from one to two dimensions, and two to three dimensions. Moreover, such studies have led to some practical new devices such as the MOSFET. Thus, this author believes that the study of low dimensional phenomena will continue to be a major focus for a long time to come as an area of basic physical phenomena.

### 1.1 Graphite Intercalation Compounds

The family of layered materials, can be divided into two general categories, naturally layered materials and deliberately structured layered materials. The former are characterized by strong intralayer interactions and weak interlayer interactions. Examples of this type of material are graphite, transition metal dichalcogenides, some silicates and metal chlorides, clays, polymers and gels. The latter are typically prepared by advanced techniques through a controlled layer by layer deposition of the

constituent species under high vacuum conditions and computer control such as sputtering, metal organic chemical vapor deposition (MOCVD) and most importantly, molecular beam epitaxy (MBE)<sup>2</sup>. Since our interest is on the graphite intercalation compounds and clays, I will only briefly mention the studies of other layered materials with the stress on the structural and dynamical properties. However, the connection between graphite intercalation compound (GIC) and clay intercalation compound (CIC) to the other layered materials will be noted where applicable.

During the past century graphite has become one of the most well studied solids known to physicists and chemists. It has a prototypical layered structure which is shown in Fig. 1.1. The carbon atoms are covalently bonded into a hexagonal lattice plane with a C-C distance of 1.42Å, and the planes are then bonded by Van der Waals interactions with an ABAB... or ABCABC... stacking period of 6.70Å along c-axis direction. The anisotropy engendered by the strong covalent intraplanar bonding and the weak van der Waals interplanar bonding is clearly reflected in the in-plane versus the out-of-plane atomic spacings. The weak van der Waals bond can be easily broken by charge transfer to or from the graphite carbon layer with the resultant formation of the so called graphite intercalation compounds (GIC)<sup>3-4</sup>. It has been reported that more than a hundred chemicals have sufficient chemical activity to form GIC's<sup>3</sup>. Depending upon the charge transfer to or from the host, the GIC is classified as a donor compound if charge is transferred to the host while it is an acceptor compound if charge is transferred from the host. Some of the chemical species that can form GIC's are listed in Table 1.1 under the category of donor and acceptor.

An unusual characteristic of GIC's is the phenomenon<sup>5</sup> of staging in which a periodic sequence of host galleries is filled with guest species. A

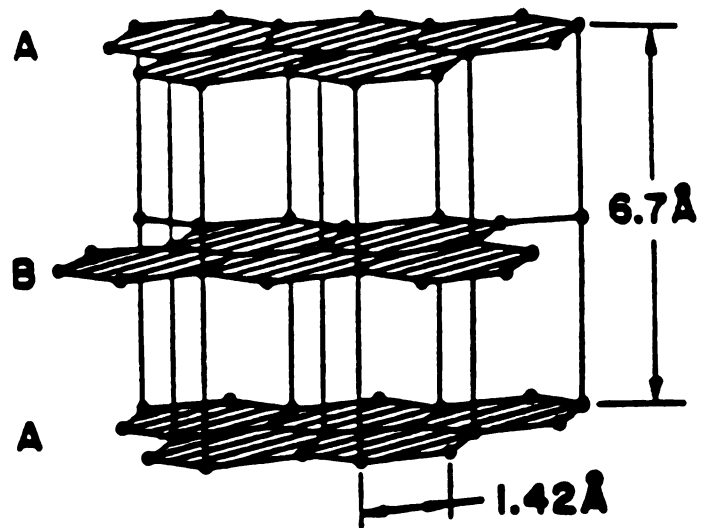


Fig. 1.1 The structure of pristine graphite.

Donors	Acceptors
Li, K, Rb, Cs, Ba, Eu, Yb, Sr, Sm, Ca	NiCl <sub>2</sub> , CoCl <sub>2</sub> , MnCl <sub>2</sub> , FeCl <sub>3</sub> , AsF <sub>5</sub> , HNO <sub>3</sub> , SbCl <sub>5</sub>

Table 1.1 Some examples of donor and acceptor intercalants of graphite.

stage  $n$  compound is one in which  $n$  carbon layers separate two adjacent intercalant layers as shown in Fig. 1.2. Staged structures with  $n$  up to 10 have been reported for alkali-metal GIC's<sup>3</sup>. The physical basis for the staging phenomenon<sup>6</sup> is the strong interatomic intercalant-intercalant interaction relative to the intercalant-graphite interaction, thereby favoring a close-packed in-plane intercalant arrangement. The introduction of each intercalate layer adds a substantial strain energy as the crystal expands to accommodate it, thereby favoring the insertion of a minimum number of intercalate layers, consistent with a given average intercalate concentration. In addition, the ionized intercalant produces a static electric field giving rise to a long range but screened repulsive interaction between intercalants in different layers, also favoring their maximum separation. Thus for a given intercalate concentration, the minimal energy state corresponds to a close-packed in-plane intercalate arrangement with the largest possible separation between a minimum number of intercalant layers. This collective interaction results in the staging phenomenon. The fact that the only stage-1 intercalated clays have been reported is probably due to relatively strong ionic bonding between intercalant and host. The situation for the intercalate transition metal dichalcogenide, where only stage-1 and stage-2 have been reported, is between the above two cases. The staging phenomenon undoubtedly enriches the study of layered materials.

The most heavily studied GIC system is the alkali-metal intercalation compounds. These donor compounds are easily synthesized and display a variety of interesting physical phenomena including staging disorder<sup>7-8</sup>, two dimensional melting<sup>9-11</sup> and diffusion<sup>12-13</sup>, complex in-plane discommensuration-domain structures<sup>14-16</sup>, and superconductivity<sup>17-19</sup>. The

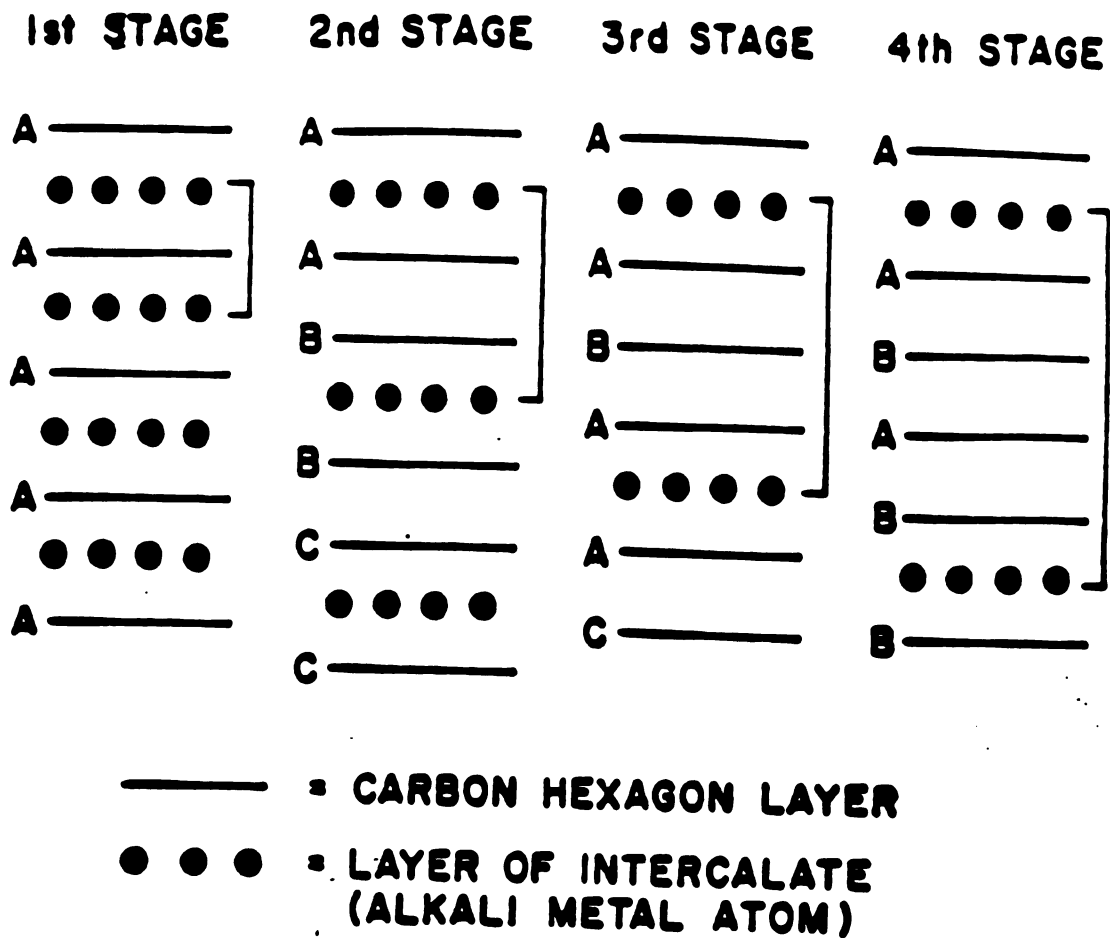


Fig. 1.2 A schematic representation of phenomenon of staging. The symbols C and G represent carbon and guest layers, respectively. The solid lines represent the carbon layers and indicate the lateral displacement of the carbon atoms (solid circles). The dashed lines represent the intercalated layers.

so called two-zone method for synthesis<sup>20</sup> of the alkali-metal compounds is shown in Fig. 1.3. Fig. 1.4 shows the K/C ratio vs. temperature difference between the two zones. The plateaus in the diagram correspond to pure stages. As can be seen, the higher the stage, the narrower the temperature range over which it exists. This means that the synthesis of pure high stage samples is more difficult than that of low stages. Although stages as high as stage-10 have been reported, these are not likely to be pure stage materials and no doubt consist of an admixture of several stages<sup>7</sup>. The relative temperatures of the zones for different alkali metals and different stages are listed in table 1.2.

Recently, solid state physicists have shifted their attention from the binary compounds (BGICs), in which a single chemical species is intercalated into the host, to ternary compounds (TGICs) which contain two different intercalants. The TGICs dramatically extend the range of composition which can be studied at constant stage and, therefore, enhance the variety of properties and phenomena that can be explored using these layered solids. These TGICs can be generally divided into four types<sup>21</sup>, namely: homogeneous, heterogeneous, trilayer and localized TGIC's (Fig. 1.5). The structures shown in Fig. 1.5. are limited to the stage-1 stacking sequence and represent only the most highly ordered inplane structure in each type. Several other structural forms within a given category are possible since the particular structure which a given TGIC exhibits will depend on external parameters such as pressure and temperature. For instance,  $\text{K}(\text{NH}_3)_{4.3}\text{C}_{24}$  is a type I TGIC, it exhibits a disordered in-plane structure at room temperature and shows an ordered in-plane structure below 185 K. We now discuss the four types of TGIC individually.

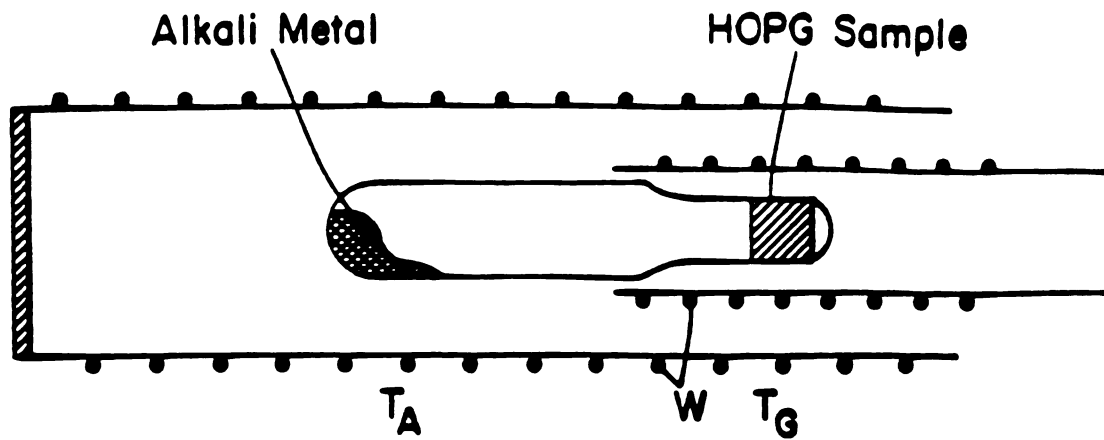


Fig. 1.3 A schematic diagram of the two-zone method used to make alkali-graphite intercalation compounds.  $T_A$  is the alkali temperature and  $T_G$  is the graphite temperature, and W is the heater wire.

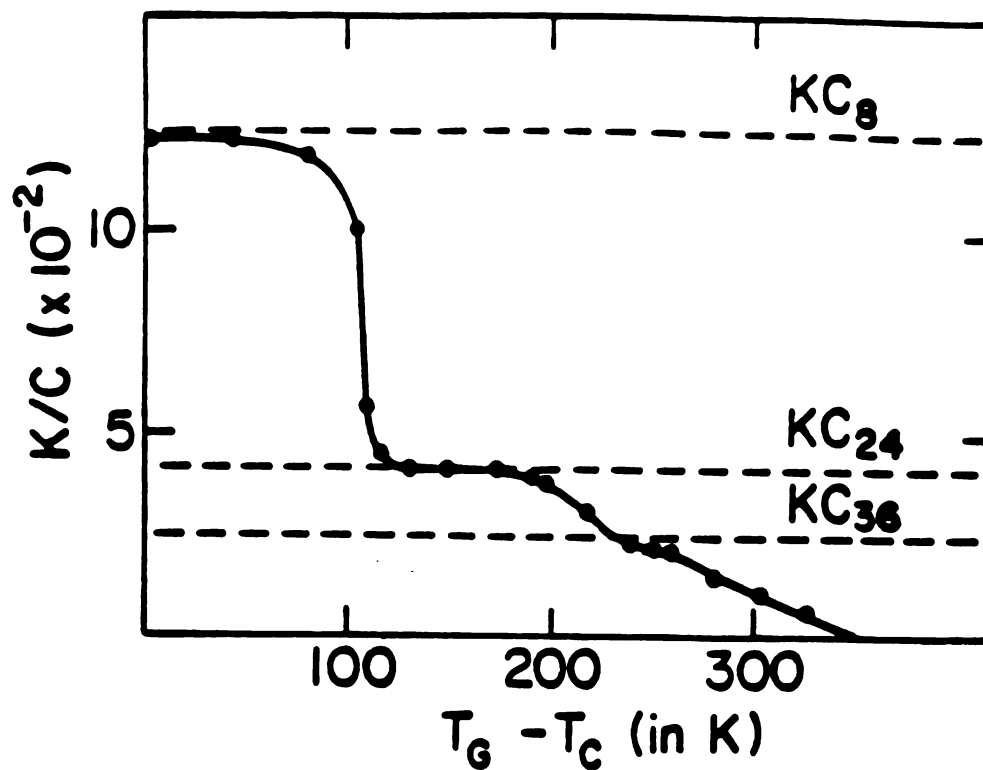
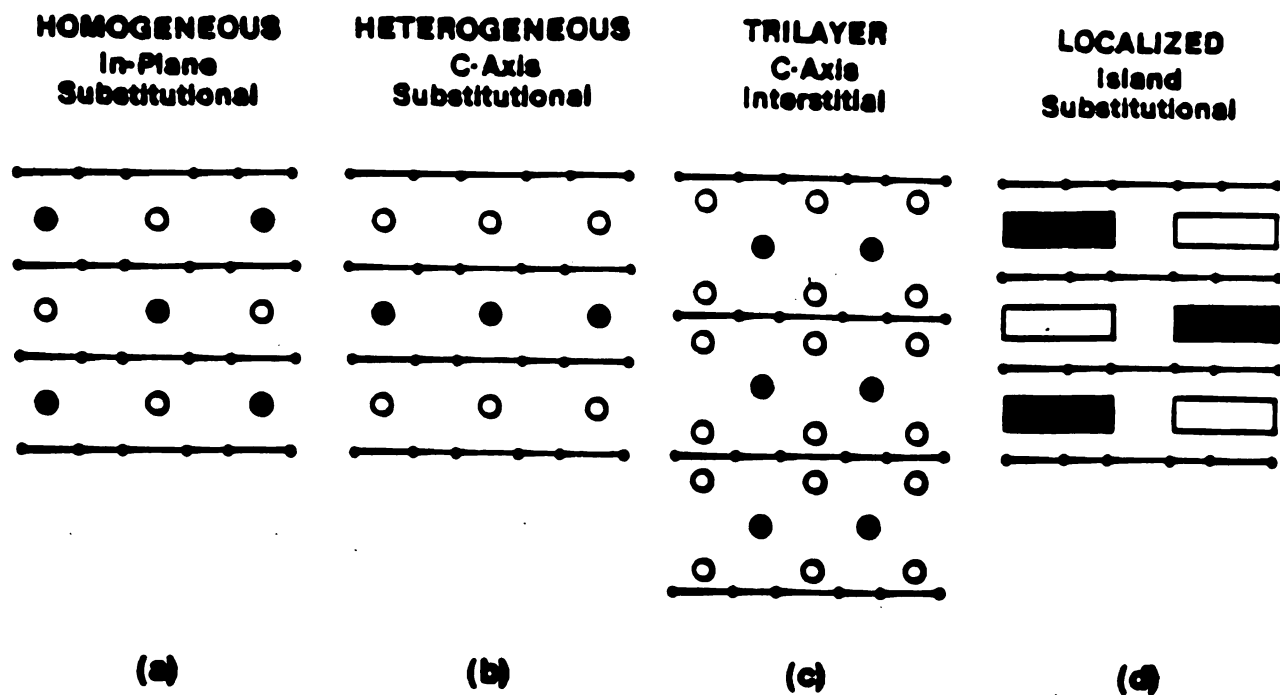


Fig. 1.4 Isobar for growth of graphite-K compounds showing intercalant uptake versus temperature difference  $T_G - T_A$  between graphite and intercalant (From ref. 20). Note the temperature ranges for staging stability, as indicated for different stage compounds.

	K $T_A = 250^\circ\text{C}$	Rb $T_A = 208^\circ\text{C}$	Cs $T_A = 194^\circ\text{C}$
Stage	$T_G(^\circ\text{C})$	$T_G(^\circ\text{C})$	$T_G(^\circ\text{C})$
1	225-320	215-330	200-425
2	350-400	375-430	475-530
3	450-480	450-480	550

Table 1.2  $T_A$  and  $T_G$  for preparation of alkali metal compounds with stages

$1 < n < 3$ .



**Fig. 1.5** A schematic representation of the four basic types of ternary graphite intercalation compound. The solid lines represent the carbon layers and indicate the lateral displacement of the carbon atoms (small solid circles). The large open and closed circles and rectangles represent intercalated species.

The type I TGIC is the homogeneous (Fig. 1.5a) form in which the mixed intercalant layers in each gallery are indistinguishable from one another. The two intercalating species form a monolayer in the same gallery and they can form commensurate, incommensurate, discommensurate ordered structures or disordered structures depending upon the external parameters and the internal interactions in the compound. Non-crystalline layers can also exhibit both compositional and topological disorder. In the compositional disorder case, the hexagonal sites of the graphite layers are randomly occupied by species A or B for which the terms "lattice-gas" or "lattice-liquid" apply<sup>22</sup>. In the topological disorder case, the 2D structure of the intercalate layers may be that of a binary liquid or even a glass both of which may exhibit short-range correlations. The lateral positional c-axis correlation between layers in a type I TGIC may be long range ordered or short range ordered or even uncorrelated as is the case for a lattice-gas/liquid or glass.

When the two intercalating species are confined to different galleries in the host structure, the second type of TGIC is formed, i.e., the heterogeneous structure shown in Fig. 1.5b. As in the case of the homogeneous TGIC's the most highly ordered form is a 3D superlattice. There are derivative structures of lower order in which the intercalate layers are incommensurate, or topologically disordered. A new form of disorder, the 1 dimensional lattice-gas/liquid, may result from a c-axis random stacking sequence. In addition, many other variations are possible. As is the case in the homogeneous TGIC's, the c-axis correlations in the heterogeneous form span the gamut from infinite range to very short range order.

When the two intercalating species form separate layers within the same gallery, the resultant compound is referred to as a trilayer TGIC. The most highly ordered form is 3D superlattice structure shown in Fig. 1.5c. Many

derivative structures from that shown in Fig. 1.5c are possible and the c-axis correlations will vary correspondingly. Since the detailed discussion of each of these structures is not of import in this thesis, and the reader is referred elsewhere for this information<sup>21</sup>.

The last type of TGIC depicted in Fig. 1.5d is the localized TGIC. In this type of TGIC, each intercalating species appears to be a single phase, and they are phase separated structurally or chemically into two distinct entities or islands. In principle, the two types of islands may have a 3D superlattice form in analogy with the other TGIC's and will also have many deviative structural forms and their associated c-axis correlations.

The TGICs no doubt broaden the field of GIC study as noted above. One of the important features of the TGIC is the ability to vary the composition at constant stage. The BGIC's, though simple in their structural and chemical properties and in the ease with which they can be synthesized impose intrinsic limitations on the types of measurements and phenomena which can be explored using them. For instance, the staging phenomenon which is so fundamentally intriguing gives rise to a relatively narrow range of compositions over which a given stage can exist in BGIC's. However, this intrinsic limitation encountered in BGIC's can be eliminated if one considers the TGIC's. Because TGIC's can contain two species in the same gallery, the stoichiometry of one of them, relative to the carbon atoms, may be held constant while the stoichiometry of the other may be varied over a large range without altering the stage of the GIC. The composition "handle" makes TGIC's an ideal arena for studying order-disorder and order-order structural phase transitions in a 2D binary alloy in analogy to the famous studies of 3d  $\text{Cu}_3\text{Au}$ <sup>23</sup>. The prototypical study of this problem can be addressed by forming the dual-alkali TGIC's system  $\text{M}_{1-x}\text{M}'_x\text{C}_y$  where M and M' are heavy

alkali metals<sup>24</sup> where  $y = 8$  for the stage-1 compound and  $12n$ ,  $n \geq 2$ , for higher stages, and  $0 < x < 1$ . Of further significance is the fact that the structure of the mixed intercalated layer in at least one TGIC  $K(NH_3)_{4.3}C_{24}$ , is that of a simple 2D liquid<sup>25-27</sup> instead of the complex domain structures of the BGIC's. This system also provides a testing ground for 2D kinetic<sup>28</sup> studies.

The TGIC'S not only expand the range of structurally based properties and phenomena which can be probed with graphite materials, but also provide new opportunities for electromagnetic investigations. With TGIC's it is possible to prepare mixed donor-acceptor compounds which exhibit intriguing behavior. For example,  $K(NH_3)_x C_{24}$  exhibits a constant stage composition dependent metal-insulator transition<sup>29</sup>. Another TGIC which contains an admixture of magnetic and nonmagnetic species displays very unusual magnetic phenomena<sup>30</sup>.

## 1.2 Neutron Scattering<sup>31-34</sup>

The neutron scattering technique has been one of the most powerful tools in condensed matter physics because of the basic properties of neutron.

The energy  $E$  of a neutron with a wave vector  $k$  is

$$E = \hbar^2 k^2 / 2m \quad (1.1)$$

where  $m$  is the neutron mass. Using  $m = 9.383 \times 10^{-31}$  kg, we have

$$(\hbar^2 / 2m) = 2.08 \text{ meV } \text{Å}^2 \quad (1.2)$$

From this equation we see that a neutron with a wave vector  $k$  a few  $\text{Å}^{-1}$  possesses an energy of about a few meV which is the typical energy of a lattice vibration and of spin excitations in magnetic insulators. If we rewrite the

energy in terms of the neutron de Broglie wavelength, we have the following relation:

$$\lambda = (h^2/2mE)^{1/2} = 9.04E^{-1/2} \text{ \AA} \quad (1.3)$$

where E is in units of meV. From this formula we see that a neutron with energy E = 25meV has a wavelength  $\lambda = 1.81 \text{ \AA}$  which is on the order of the interatomic distance in condensed matter. In consequence, the diffraction of neutrons from condensed matter can display pronounced interference effects.

There are other energy units frequently used in neutron spectroscopy. We list the conversion of them for convenience.

$$\begin{aligned} 1\text{THz} &= 10^{12} \text{ s}^{-1} = 4.14\text{meV} \\ 1\text{meV} &= 0.24 \text{ THz} = 8.07 \text{ cm}^{-1} = 11.61 \text{ K} \\ 1 \text{ THz} &= 33.35 \text{ cm}^{-1} = 48.02 \text{ K}. \end{aligned} \quad (1.4)$$

The penetration depth of neutrons in matter is very long, because they are uncharged, and are only scattered by nuclear forces. Therefore, neutron scattering is well suited to the study of bulk properties. The nature of the nuclear force results in a random variation of the scattering cross section for various nuclei, in contrast to the smooth dependence of the scattering cross-section on atomic number as in the case of x-ray diffraction. The scattering length for different isotopes can be very different, for instant, hydrogen has a scattering length of  $-3.74 \text{ cm}^{-1}$ , while the deuteron has a length of  $0.667 \text{ cm}^{-1}$ . This fact provides us an advantage for many neutron scattering studies.

In a neutron scattering event, there are two conditions that have to be satisfied, namely, energy conservation and momentum conservation. The conservation of energy requires that the energy transferred to the target be equal to the energy loss of the scattered neutron, i.e.,

$$h\omega = E - E' = (\hbar^2/2m)(k^2 - k'^2) \quad (1.5)$$

where  $E$  and  $E'$  are the initial and final energy of the neutron respectively. The conservation of momentum requires that

$$\vec{Q} = \vec{k} - \vec{k}' = \vec{G} + \vec{q} \quad (1.6)$$

where  $\vec{Q}$  is defined as the scattering vector,  $\vec{k}$  and  $\vec{k}'$  are the initial and final neutron wavevectors,  $\vec{G}$  is a reciprocal lattice vector and  $\vec{q}$  is the deviation of  $\vec{Q}$  from the reciprocal lattice vector. Note that if  $\vec{q} = 0$  and  $k = k'$ , we simply get Bragg's Law, written as

$$\lambda = 2d \sin \theta \quad (1.7)$$

where  $\theta$  is the half scattering angle and  $d$  is the interplanar spacing.

In a neutron experiment, one actually measures the so called double differential cross-section  $\frac{d^2\sigma}{d\Omega dE'}$ , this quantity can be generally expressed as

$$\frac{d^2\sigma}{d\Omega dE'} = \frac{k'}{k} \overline{\sum_{\lambda\lambda'} p_{\lambda} |\langle \vec{k}'\lambda' | \hat{V} | \vec{k}\lambda \rangle|^2 \delta(h\omega + E_{\lambda} - E_{\lambda'})} \quad (1.8)$$

where  $V$  is the scattering potential,  $|\vec{k}\rangle$  and  $|\vec{k}'\rangle$  are the initial and final states of the neutron, and  $|\lambda\rangle$  and  $|\lambda'\rangle$  are the initial and final states of the target system. The weight  $p_{\lambda}$  for the state  $|\lambda\rangle$  satisfies a normalization condition.

$$\sum_{\lambda} p_{\lambda} = 1 \quad (1.9)$$

The horizontal bar stands for any relevant average over and above those included in the weights  $p_{\lambda}$ .

We can calculate the scattering intensity for any neutron scattering process for a specific system from Eq. (1.8), however those calculations are usually very lengthy. There are many texts where this is done in great detail.<sup>31-34</sup> Here, following the treatment of Lovesey<sup>31</sup>, we reiterate a few of the highlights.

## STATIC APPROXIMATION

The static approximation amounts to neglecting the term  $E_{\lambda'} - E_{\lambda}$ , in the  $\delta$ -function in Eq. (1.8). This means that the energy transferred to and from the scattering system is much smaller than the energy of the incident neutron or equivalently the condition for the validity of the static approximation is that the time taken for the neutron to cross from one atom to the next is small compared to the characteristic oscillation or relaxation time of the scattering system. The cross-section then reduces to

$$\frac{d^2\sigma}{d\Omega dE'} = \sum_{\lambda\lambda'} p_{\lambda} |\langle \vec{k}' \lambda' | \hat{V} | \vec{k} \lambda \rangle|^2 \delta(h\omega). \quad (1.10)$$

Note that the factor  $(k'/k)$  in (1.8) is unity since the scattering is elastic. Integration with respect to  $E'$ , yields the final form

$$\frac{d\sigma}{d\Omega} = \langle |k' | V | k \rangle^2 \rangle. \quad (1.11)$$

Here we have used a notation that will be used throughout this chapter, namely,

$$\langle (\dots) \rangle = \sum_{\lambda} p_{\lambda} \langle \lambda | (\dots) | \lambda \rangle,$$

and the condition

$$\sum_{\lambda} |\lambda\rangle \langle \lambda| = 1. \quad (1.12)$$

It is worth noting that the static approximation is distinct from purely elastic scattering. In the latter case, the final states are identical with the initial states, i.e.,  $\lambda' = \lambda$  in (1.10). In contrast, the static approximation includes all possible final states.

In chapter 2, we use this approximation to determine the structure of  $K(\text{NH}_3)_2\text{C}_{24}$  where the rotational energy of  $\text{NH}_3$  is small compared with the incident thermal neutron energy, therefore it would be valid to sum over all the rotational states.

## COHERENT AND INCOHERENT SCATTERING

The scattering interaction between a neutron and a nucleus can be described by the Fermi pseudopotential<sup>35</sup>. In a system with a rigid array of  $N$  nuclei, the position vector of the  $l$ th nucleus being denoted by  $\vec{R}_l$ , and the scattering length of  $l$ th nucleus being described as  $b_l$ , then the interaction potential is

$$\hat{V}(\vec{r}) = \frac{2\pi\hbar^2}{m} \sum_l b_l \delta(\vec{r} - \vec{R}_l). \quad (1.13)$$

Insert (1.11) into (1.12), and after some manipulations, one has

$$\frac{d\sigma}{d\Omega} = \sum_{l,l'} \exp(i\vec{k} \cdot (\vec{R}_l - \vec{R}_{l'})) b_l^* b_{l'}. \quad (1.14)$$

For  $l \neq l'$ , we have

$$b_l^* b_{l'} = b_l^* b_{l'} = |\bar{b}|^2$$

But if  $l' = l$ ,  $b_l^* b_l = |b_l|^2 = |b|^2$ ,

so that in general

$$b_l^* b_{l'} = |\bar{b}|^2 + \delta_{l,l'} (|b|^2 - |\bar{b}|^2). \quad (1.15)$$

The scattering which derives from the first term in (1.15) is called coherent scattering, and that from second term refers to incoherent scattering. Then from (1.15) and (1.14) we have

$$\frac{d\sigma}{d\Omega} = \left(\frac{d\sigma}{d\Omega}\right)_{\text{coh}} + \left(\frac{d\sigma}{d\Omega}\right)_{\text{incoh}},$$

where the coherent cross-section is

$$\left(\frac{d\sigma}{d\Omega}\right)_{\text{coh}} = |\bar{b}|^2 \left| \sum_l \exp(i\vec{k} \cdot \vec{R}_l) \right|^2 \quad (1.16)$$

and the incoherent cross-section

$$\left(\frac{d\sigma}{d\Omega}\right)_{\text{incoh}} = N(|b|^2 - |\bar{b}|^2) = N|b - \bar{b}|^2 \quad (1.17)$$

There are two physical origins of incoherent scattering. First, it originates from different isotopes of the atom from which the neutron is

scattered. Since the neutron interacts with the nuclei, the scattering power varies from isotope to isotope. Because these isotopes are randomly distributed throughout the sample, the scattering length varies from site to site. The second source of incoherent scattering is the coupling of the neutron spin with the nuclear spins. If the nucleus has a spin of  $I$ , then the neutron-nuclear system possesses two spin values  $I + \frac{1}{2}$  or  $I - \frac{1}{2}$ . These two spin states produce different scattering lengths, and they are randomly distributed in the sample resulting in spin incoherence. Table 1.3 lists the scattering lengths, the coherent and total cross-sections for the elements involved in this thesis.

As can be seen from Eqs. (1.16) and (1.17) coherent scattering reflects strong interference effects allowing the study of collective properties whereas incoherent scattering only contains information about an individual nucleus. The physical reasons for this are as follows: Because the scattering length varies from one isotope to another and also depends on the nuclear spin orientation (relative to the neutron), the neutron does not see a crystal of uniform scattering potential but one in which the scattering length varies from one point to the next. It is only the average scattering potential that can give interference effects and thus coherent scattering proportional to  $|\bar{b}|^2$ . The deviations from the average potential are randomly distributed and therefore reflect the individual nucleus; they

Table 1.3 Scattering lengths, coherent and total cross-sections for the isotopes and elements of relevance in this thesis.

	$\bar{b}$	$\sigma_c$	$\sigma_{tot}$
O	0.58	4.23	4.24
H	-0.374	1.76	81.50
D	0.667	5.59	7.60
Mg	0.52	3.40	3.7
Fe	0.95	11.34	11.8
Al	0.35	1.54	1.5
Ca	0.49	3.02	3.1
Si	0.42	2.22	2.2
C	0.665	5.6	5.6
N	0.937	11.0	11.5
K	0.379	2.19	2.30

Scattering length  $\bar{b}$  in units of  $10^{-12}$  cm, cross-section in units of  $10^{-24}$  cm<sup>2</sup>.

therefore give incoherent scattering proportional to the mean-square deviation, i.e. to  $|\overline{b-\bar{b}}|^2$ .

#### DOUBLE DIFFERENTIAL CROSS-SECTION

In the previous paragraph, we discussed the coherent and incoherent scattering in the static approximation. This approximation does not hold in general. We now write the double differential cross-section in terms of the coherent and incoherent scattering cross-sections. Then

$$\frac{d^2\sigma}{d\Omega dE'} = N \frac{k'}{k} \left[ \frac{\sigma_c}{4\pi} S_{\text{coh}}(\vec{Q}, \omega) + \frac{\sigma_i}{4\pi} S_{\text{inc}}(\vec{Q}, \omega) \right] \quad (1.18)$$

Here  $S_{\text{coh}}(\vec{Q}, \omega)$  and  $S_{\text{inc}}(\vec{Q}, \omega)$  represent the dynamic structure factors for the coherent and incoherent parts of the scattering including both elastic and inelastic contributions. One finds that

$$S_{\text{coh}}(\vec{Q}, \omega) = \frac{1}{2\pi\hbar N} \sum_{jj'} \int_{-\infty}^{\infty} \langle \exp(-i\vec{Q}\cdot\vec{r}_{j'}(0)) \exp(i\vec{Q}\cdot\vec{r}_j(t)) \rangle e^{-i\omega t} dt \quad (1.19)$$

and

$$S_{\text{inc}}(\vec{Q}, \omega) = \frac{1}{2\pi\hbar N} \sum_j \int_{-\infty}^{\infty} \langle \exp(i\vec{Q}\cdot\vec{r}_j(0)) \exp(i\vec{Q}\cdot\vec{r}_j(t)) \rangle e^{-i\omega t} dt \quad (1.20)$$

For most complex problems it is convenient to deal with the intermediate scattering function  $I(Q, t)$  defined as

$$I(Q, t) = \frac{1}{N} \sum_{jj'} \langle \exp(-i\vec{Q}\cdot\vec{r}_{j'}(0)) \exp(i\vec{Q}\cdot\vec{r}_j(t)) \rangle \quad (1.21)$$

Then

$$S_{\text{coh}}(\vec{Q}, \omega) = \frac{1}{2\pi\hbar} \int_{-\infty}^{\infty} \exp(-i\omega t) I(Q, t) dt \quad (1.22)$$

We can further express  $I(\vec{Q}, t)$  into the  $\vec{Q}$  space Fourier transform of a function of real space and time, the pair correlation function,  $G(\vec{r}, t)$ , which represents the ensemble averaged probability of finding a particle at position  $\vec{r}_j$  at time  $t$  if a particle was at the origin at time 0. Therefore,

$$S_{\text{coh}}(\vec{Q}, \omega) = \frac{1}{2\pi\hbar} \int I(\vec{Q}, t) e^{-i\omega t} dt$$

$$= \frac{1}{2\pi\hbar} \int [ \int G(\vec{r}, t) \exp(i\vec{Q} \cdot \vec{r}) d\vec{r} ] e^{-i\omega t} dt \quad (1.23)$$

Similar arguments apply to the incoherent scattering, in this case, we have the time dependent self-correlation function  $G_S(\vec{r}, t)$  which in turn is the probability of finding a particle at  $\vec{r}$  at time  $t$  if the same particle is at the origin at  $t = 0$ . Then

$$\begin{aligned} S_{\text{inc}}(\vec{Q}, \omega) &= \frac{1}{2\pi\hbar} \int I_S(\vec{Q}, t) e^{-i\omega t} dt \\ &= \frac{1}{2\pi\hbar} \int [ \int G_S(\vec{r}, t) \exp(i\vec{Q} \cdot \vec{r}) d\vec{r} ] e^{-i\omega t} dt \end{aligned} \quad (1.24)$$

where  $I_S(\vec{Q}, t)$  defined as

$$I_S(\vec{Q}, t) = \frac{1}{N} \sum_j \langle \exp(-i\vec{Q} \cdot \vec{r}_j(0)) \exp(i\vec{Q} \cdot \vec{r}_j(t)) \rangle \quad (1.25)$$

Now we are going to calculate the coherent and incoherent one-phonon scattering function. In general we can write

$$G(\vec{r}, t) = G(\vec{r}, \infty) + G'(\vec{r}, t) \quad (1.26)$$

So that

$$\lim_{t \rightarrow \infty} G'(\vec{r}, t) = 0$$

where  $G(\vec{r}, \infty)$  is known as the Patterson function giving rise to the elastic scattering and is used as an aid to structure determination in x-ray scattering and neutron diffraction by crystals.

Similarly, we define

$$G_S(\vec{r}, t) = G_S(\vec{r}, \infty) + G'_S(\vec{r}, t) \quad (1.26a)$$

Here again  $\lim_{t \rightarrow \infty} G'_S(\vec{r}, t) = 0$

Therefore,

$$\left( \frac{d^2\sigma}{d\Omega dE'} \right)_{\text{coh}}^{\text{inel}} = \frac{N^0 c}{4\pi} \frac{k'}{k} \frac{1}{2\pi\hbar} \int_{-\infty}^{\infty} dt e^{-i\omega t} \int d\vec{r} \exp(i\vec{Q} \cdot \vec{r}) G'(\vec{r}, t) \quad (1.27)$$

$$\left( \frac{d^2\sigma}{d\Omega dE'} \right)_{\text{inc}}^{\text{inel}} = \frac{N^0 c}{4\pi} \frac{k'}{k} \frac{1}{2\pi\hbar} \int_{-\infty}^{\infty} dt e^{-i\omega t} \int d\vec{r} \exp(i\vec{Q} \cdot \vec{r}) G'_S(\vec{r}, t) \quad (1.28)$$

One-phonon process

Now we consider a Bravais lattice of  $N$  atoms with their equilibrium positions given by the lattice vectors

$$\vec{\ell} = \ell_1 \vec{a}_1 + \ell_2 \vec{a}_2 + \ell_3 \vec{a}_3,$$

The displacement of the atom at the  $\ell$ th site is denoted by  $\vec{u}(\ell)$ . Thus the position vector of this atom is

$$\vec{R}_\ell = \vec{\ell} + \vec{u}(\ell) \quad (1.29)$$

It can be shown that the correlation function is

$$G(\vec{r}, t) = \frac{1}{(2\pi)^3 N} \sum_{\ell, \ell'} \int d\vec{k} \exp(-i\vec{k} \cdot \vec{r}) \exp[i\vec{k} \cdot (\vec{\ell}' - \vec{\ell})] \langle \exp[i\vec{k} \cdot \hat{u}(\ell)] \exp[i\vec{k} \cdot \hat{u}(\ell', t)] \rangle \quad (1.30)$$

and that

$$G_S(\vec{r}, t) = \frac{1}{(2\pi)^3 N} \sum_{\ell} \int d\vec{k} \exp(-i\vec{k} \cdot \vec{r}) \langle \exp[i\vec{k} \cdot \hat{u}(\ell)] \exp[i\vec{k} \cdot \hat{u}(\ell, t)] \rangle \quad (1.30a)$$

To calculate the double differential cross-section we need to evaluate the relation

$$\begin{aligned} & \langle \exp[-i\vec{k} \cdot \hat{u}(\ell)] \exp[i\vec{k} \cdot \hat{u}(\ell', t)] \rangle \\ &= \exp\left\{\frac{1}{2} \langle -[\vec{k} \cdot \hat{u}(\ell)]^2 - [\vec{k} \cdot \hat{u}(\ell')]^2 + 2\vec{k} \cdot \hat{u}(\ell) \vec{k} \cdot \hat{u}(\ell', t) \rangle\right\} \\ &= \exp\{-2W(\vec{k})\} \exp\{\langle \vec{k} \cdot \hat{u}(\ell) \vec{k} \cdot \hat{u}(\ell', t) \rangle\} \\ &\approx \exp\{-2W(\vec{k})\} \cdot [1 + \langle \vec{k} \cdot \hat{u}(\ell) \vec{k} \cdot \hat{u}(\ell', t) \rangle + \dots] \end{aligned} \quad (1.31)$$

where  $\exp\{-2W(\vec{k})\}$  is the Debye-Waller factor, and the formula is expanded to the one-phonon process, and we also need

$$\hat{u}_\alpha(\ell) = \sum_{j, \vec{q}} \left\{ \frac{\hbar}{2NM\omega_j(\vec{q})} \right\}^{1/2} \sigma_\alpha^j(\vec{q}) \exp(i\vec{q} \cdot \vec{\ell}) \{ \hat{a}_j(\vec{q}) + \hat{a}_j^\dagger(-\vec{q}) \} \quad (1.32)$$

which describes the displacements in terms of annihilation and creation operators  $\hat{a}_j(\vec{q})$  and  $\hat{a}_j^\dagger(\vec{q})$ , the polarization components  $\sigma_\alpha^j(\vec{q})$  and a mode index  $j$ . In other words, we expand the displacements by normal modes. Subtracting the elastic scattering from Eqs. (1.26) and (1.26a), we obtain the one-phonon coherent and incoherent inelastic scattering cross-sections

$$\left(\frac{d^2\sigma}{d\Omega dE'}\right)_{\text{coh}}^{\text{inel}} = \frac{0_{\text{ck}'}}{4\pi k} \frac{(2\pi)^3}{v_0} \frac{1}{2M} \sum_{\vec{q}} \exp[-2W(\vec{Q})] \sum_{\vec{q}} \frac{|\vec{Q} \cdot \vec{\sigma}^J(\vec{q})|^2}{\omega_j(\vec{q})} \\ \times [n_j(\vec{q}) \delta(\omega + \omega_j(\vec{q})) \delta(\vec{Q} + \vec{q} - \vec{\tau}) + [n_j(\vec{q}) + 1] \delta(\omega - \omega_j(\vec{q})) \delta(\vec{Q} - \vec{q} - \vec{\tau})] \quad (1.33)$$

$$\left(\frac{d^2\sigma}{d\Omega dE'}\right)_{\text{inc}}^{\text{inel}} = \frac{0_i}{8\pi} \frac{k'}{k} \frac{1}{M} \exp[-2W(\vec{Q})] \sum_{\vec{q}} \frac{|\vec{Q} \cdot \vec{\sigma}^J(\vec{q})|^2}{\omega_j(\vec{q})} \\ \times [n_j(\vec{q}) \delta(\omega + \omega_j(\vec{q})) + [n_j(\vec{q}) + 1] \delta(\omega - \omega_j(\vec{q}))] \quad (1.34)$$

where  $n_j(\vec{q})$  is the Bose-Einstein thermal occupation factor given by

$$n_j(\vec{q}) = \frac{1}{\exp(\hbar\omega_j(\vec{q})/kT) - 1} \quad (1.35)$$

The cross-section in Eq. (1.33) is the sum of two terms. The first, which contains the expression  $\delta(\omega + \omega_j(\vec{q})) \delta(\vec{Q} + \vec{q} - \vec{\tau})$ , represents a scattering process in which one phonon is annihilated and the second term, containing  $\delta(\omega - \omega_j(\vec{q})) \delta(\vec{Q} - \vec{q} - \vec{\tau})$ , represents a process in which one phonon is created.

The two  $\delta$ -functions in each process represent conservation of energy and momentum, i.e.

$$E' = E \pm \hbar\omega_j(\vec{q}) \\ \vec{k}' = \vec{k} \pm \vec{Q} - \vec{\tau}. \quad (1.36)$$

These conditions determine the phonon dispersion relations  $\omega_j(\vec{q})$  as a function of  $\vec{q}$ . In chapter 3, we will address to this equation again.

The one-phonon incoherent cross-section Eq. (1.34) can be further reduced to

$$\left(\frac{d^2\sigma}{d\Omega dE'}\right)_{\text{inc}}^{\text{inel}} = \frac{3N^0_i}{8\pi M} \frac{k'}{k} \exp[-2W(\vec{Q})] \{|\vec{Q} \cdot \vec{\sigma}^J(\vec{q})|^2\}_{\text{av}} \frac{Z(\omega)}{\omega} [n(\omega) + 1] \quad (1.34a)$$

where the average  $\{|\vec{Q} \cdot \vec{\sigma}^J(\vec{q})|^2\}_{\text{av}}$  is taken over modes with frequency  $\omega$ ,  $Z(\omega)$  is the phonon density of states.

The generalization of these results to non-Bravais lattice is straightforward. It can be shown that the one-phonon inelastic coherent cross-section becomes

$$\left(\frac{d^2\sigma}{d\Omega dE'}\right)_{\text{coh}}^{\text{inel}} = \frac{k'}{k} \frac{(2\pi)^3}{v_0} \sum_{\vec{\tau}} \sum_{j, \vec{q}} \frac{1}{2\omega_j(\vec{q})} \left| \sum_{\vec{d}} \bar{b}_{\vec{d}} \exp\{-W_{\vec{d}}(\vec{Q}) + i\vec{Q} \cdot \vec{d}\} \{\vec{Q} \cdot \vec{\sigma}_{\vec{d}}^j(\vec{q})\} M^{-1/2} \right|^2 \\ \times [n_j(\vec{q}) \delta(\omega + \omega_j(\vec{q})) \delta(\vec{Q} + \vec{q} - \vec{\tau}) + \{n_j(\vec{q}) + 1\} \delta(\omega - \omega_j(\vec{q})) \delta(\vec{Q} - \vec{q} - \vec{\tau})] \quad (1.33a)$$

where  $\vec{d}$  is the  $d$ th atom in a unit cell, and we define the dynamic structure factor for the unit cell,

$$H_{\vec{q}}^j(\vec{Q}) = \sum_{\vec{d}} \bar{b}_{\vec{d}} \exp\{-W_{\vec{d}}(\vec{Q}) + i\vec{Q} \cdot \vec{d}\} \{\vec{Q} \cdot \vec{\sigma}_{\vec{d}}^j(\vec{q})\} M^{-1/2} \quad (1.37)$$

Similarly, we can obtain the one-phonon inelastic incoherent cross-section

$$\left(\frac{d^2\sigma}{d\Omega dE'}\right)_{\text{inc}}^{\text{inel}} = \frac{k'}{k} \sum_{\vec{d}} \{ |b_{\vec{d}}|^2 - |\bar{b}_{\vec{d}}|^2 \} \exp\{-2W_{\vec{d}}(\vec{Q})\} \frac{1}{M_{\vec{d}}} \sum_{j, \vec{q}} |\vec{Q} \cdot \vec{\sigma}_{\vec{d}}^j(\vec{q})|^2 \\ \times \frac{1}{2\omega_j(\vec{q})} [n_j(\vec{q}) \delta(\omega + \omega_j(\vec{q})) + \{n_j(\vec{q}) + 1\} \delta(\omega - \omega_j(\vec{q}))] \quad (1.34b)$$

This formula is not as useful as that for a simple lattice, because the weight  $|\vec{Q} \cdot \vec{\sigma}_{\vec{d}}^j(\vec{q})|^2$  in general is unknown. However, for a hydrogenated sample, the incoherent scattering will be dominated by the contribution from the protons, so we get back to the Eq. (1.34) approximately.

### 1.3 Neutron Scattering Instruments

The neutron scattering measurements in this thesis were performed with a triple axis spectrometer (BT-4) at the National Bureau of Standards Reactor. The total power of the reactor is  $10^5$  W giving a total flux of  $10^{15}$  neutrons  $s^{-1}$ . A schematic diagram of a triple-axis neutron spectrometer is depicted in Fig. 1.6. A beam of neutrons from the reactor passes through a collimator and impinges on a monochromator which selects a particular wavelength from the distribution in the reactor by use of a Bragg reflection. The monochromatic beam then passes through a second collimator before being diffracted by the sample, where the angle  $\psi$  in Fig. 1.6 defines the sample orientation with respect to the incoming beam, and the angle  $\phi$  defines the scattering angle. A third collimator was placed before an analyzer crystal which measures the final energy of the scattered neutrons, again via the Bragg law. The neutrons then pass through a final collimator before entering a  $^3\text{He}$  detector. Several crystals can be used as monochromators and analyzers, the most common being pyrolytic graphite and copper as is the case at BT-4.

The triple axis spectrometer is ideal for constant scattering vector ( $\vec{Q}$ ) measurements and for quasi-elastic scattering. Two modes of operation are possible. The most desirable one is the fixed final energy mode so that the analyzer crystal is fixed at a certain angle selecting a constant final energy and the monochromator is scanned giving a varying initial energy. The energy resolution for this mode is shown in Fig. 1.7. There are two distinguishing features in this diagram. First, the energy resolution is degraded as the energy transfer increases, and second, the resolution change takes place before the monitor detector placed just before the sample. The first feature gives an advantage for phonon creation measurement, since the

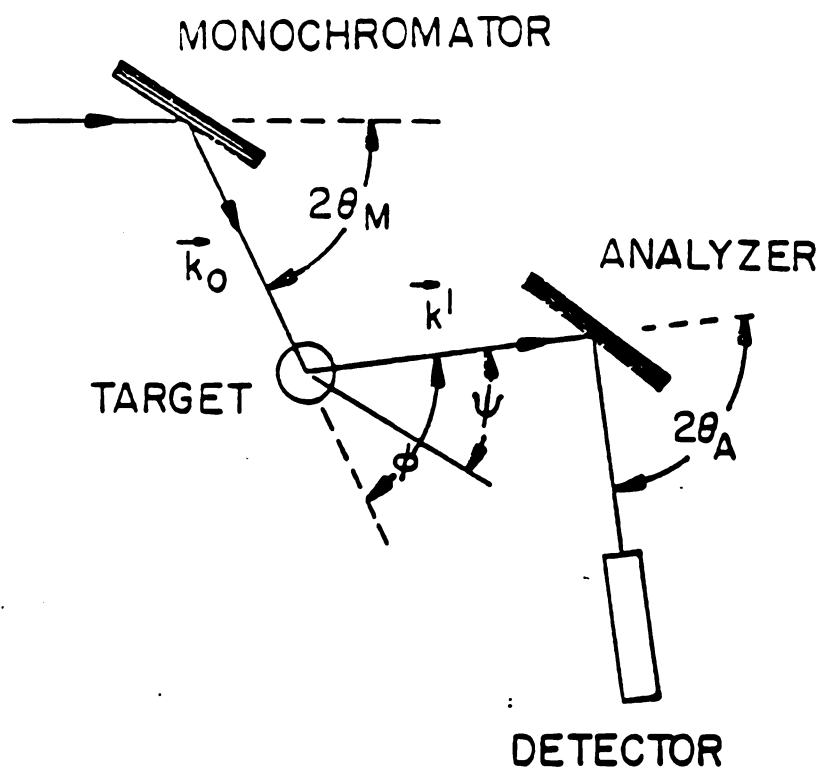


Fig. 1.6 A schematic representation of a triple-axis spectrometer.

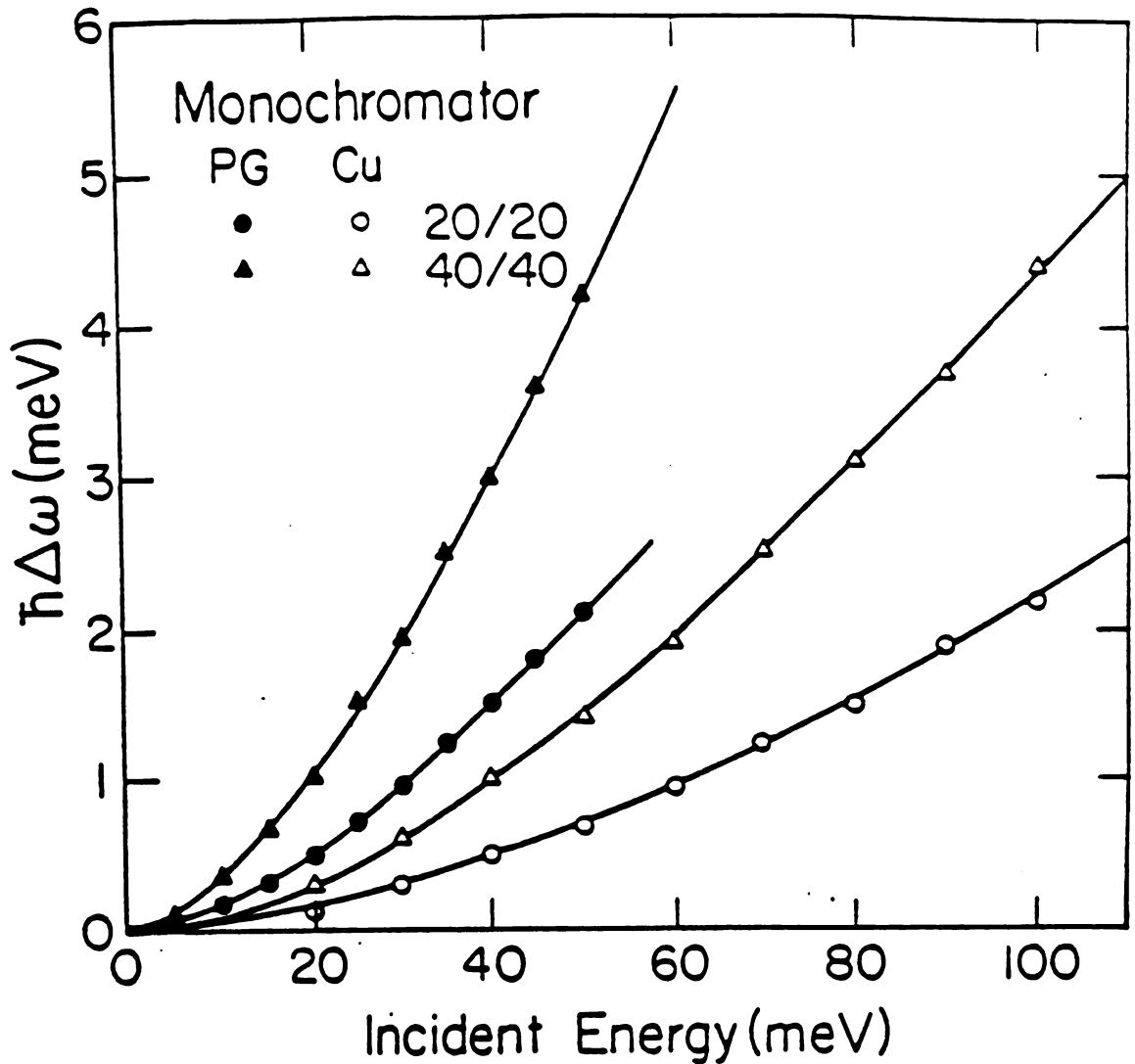


Fig. 1.7 The resolution of one-half of a triple-axis instrument as a function of the energy passed by that half for two different collimations and two different crystals for BT-4. (By one-half of an instrument, we mean collimator-monochromator-collimator/collimator-analyzer-collimator.) To obtain the total instrumental resolution, one has to find both half instrument resolutions then add them in quadrature.

intensity of a phonon group decreases with increasing  $\omega$  as shown in Eq. (1.35), and the reduced resolution at the larger energy transfer compensates for the intensity loss giving an enhancement overall. The second feature obviates the need to correct the data for the varying resolution function. The changing reflectivity of the monochromator is corrected by the monitor detector. However, it is necessary to make one correction in this mode, which comes from the higher order harmonic contamination. A filter is used to remove the harmonics from analyzer and must be placed after the sample. Therefore, the harmonic contamination in the incident beam causes the monitor detector to overcount. This effect can be simply measured by using a powder sample without a filter and comparing the intensity of a given Bragg peak with its  $\lambda/2$  counterpart. This gives the first order correction since we ignore the higher order contamination as well as the changing reflectivity of the powder sample. Fig. 1.8 gives the correction factor as a function of incident energy, determined using a Si powder sample ((111) reflection) for BT-4 at NBS.

The other mode of measuring phonon groups, which is less often used, is fixed initial energy. In this method, the main advantages are using the high flux part of the neutron distribution from the reactor, and the avoidance of swinging the entire instrument around the monochromator since the monochromator angle is fixed in this case. However, one has to pay the price of making more corrections including corrections for the varying resolution function, the varying reflectivity of the analyzer crystal, and the fact that the efficiency of the detector may depend on the final energy.

Another type of neutron scattering instrument for inelastic and quasielastic work is the time-of-flight spectrometer (TOF). The schematic outline of a time-of-flight spectrometer is shown in Fig. 1.9. A

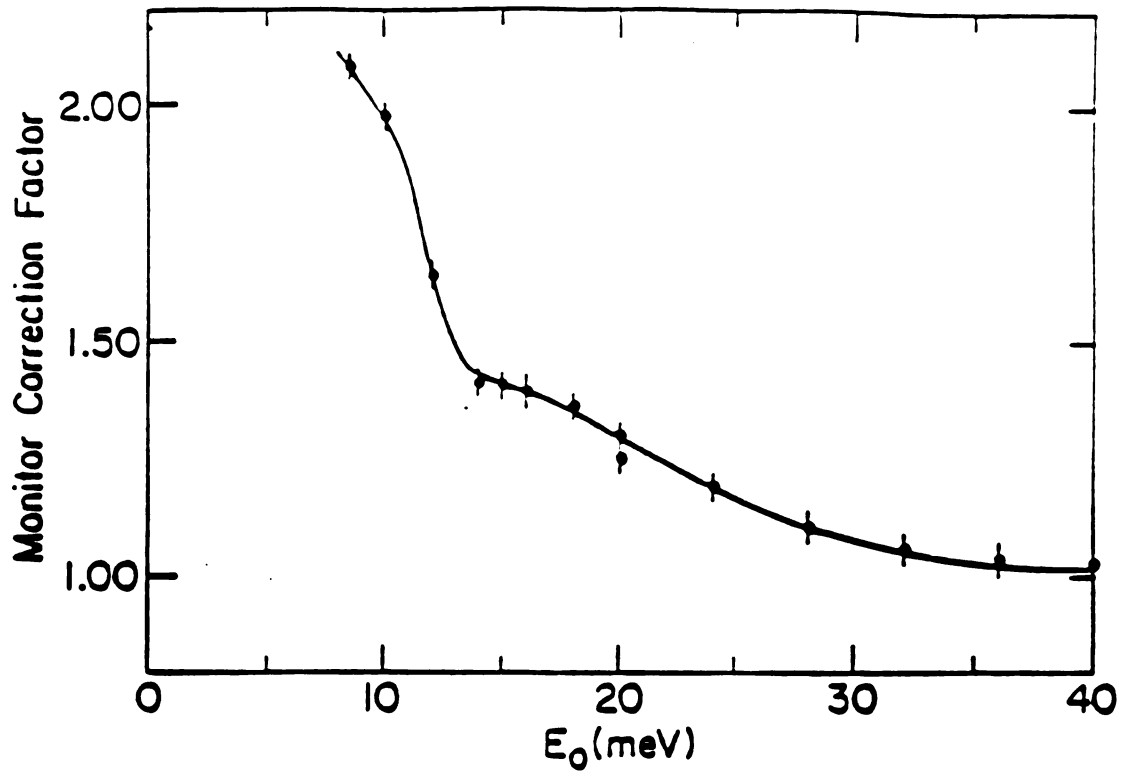


Fig. 1.8 The monitor correction factor in the fixed-final-energy mode as function of the initial energy. This particular figure was obtained at BT-4, a triple-axis instrument located at the NBS reactor. When data have been taken in the fixed-final-energy mode, they must be multiplied by this factor to account for the  $\lambda/2$  contamination in the monitor detector.

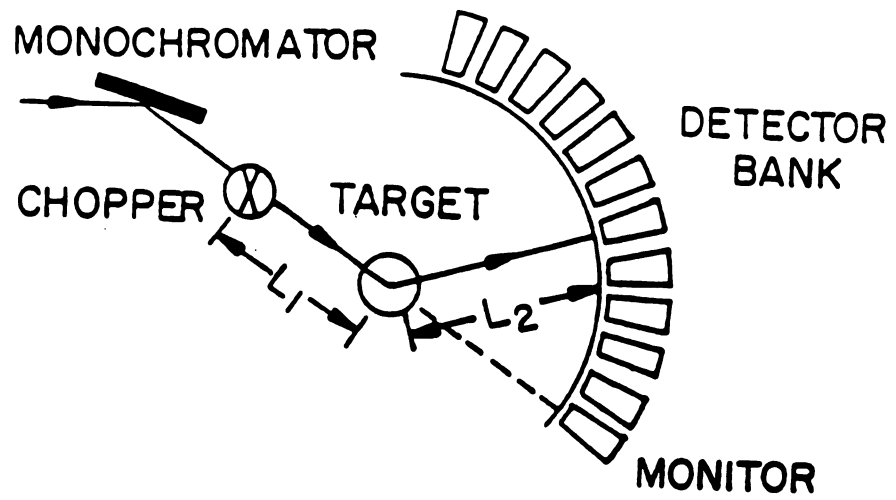


Fig. 1.9 A schematic outline of a time-of-flight spectrometer.

monochromator selects an initial energy  $E_0$  by a Bragg reflection. Then the monochromatic neutron beam is chopped in short bursts, the energy of the neutrons is measured by the flight time of the neutrons from the chopper to the detectors. An array of detectors is placed in the scattering plane allowing one to simultaneously collect data for several wave vectors. This type of instrument is well suited for studying the dynamics of liquids or powder samples for all wave vectors can be measured at once. Single crystal work is also possible, but the interpretation of the spectra is not straight forward. In this case, the triple-axis spectrometer is more suitable.

For the study of the structure of GIC's by use of elastic neutron scattering, three major scattering configurations, i.e. the  $[00l]$ , inplane, and  $c^*$  scan are employed. They are schematically shown in Fig. 1.10. The incident neutron wave vector is  $\vec{k}_0$  and the scattered neutron wave vector is  $\vec{k}'$ , where for elastic neutron scattering  $k_0 = k'$ . The inplane scan can be achieved simply by rotating the sample  $90^\circ$  about an axis perpendicular to the scattering plane from the  $[00l]$  scattering configuration. The  $[00l]$  and inplane scans are also called  $\theta$ - $2\theta$  scans. The  $c^*$ -scan is more complicated and computer control is used to keep the scattering vector along the AB line (Fig. 1.10.).

For inelastic neutron scattering, constant- $\vec{Q}$  mode measurement has been used most often. From Eqs. (1.33) and (1.34), we know that the dynamical structure factor is proportional to  $(\vec{Q} \cdot \vec{e}_s)^2$ , therefore,  $\vec{Q}$  selection can be employed to measure different polarized excitations. Fig. 1.11 illustrates three configurations for phonon dispersion measurements. With configuration I the frequencies of the longitudinal modes propagating along the  $c$  direction can be measured unambiguously as a function of wave vector. Using

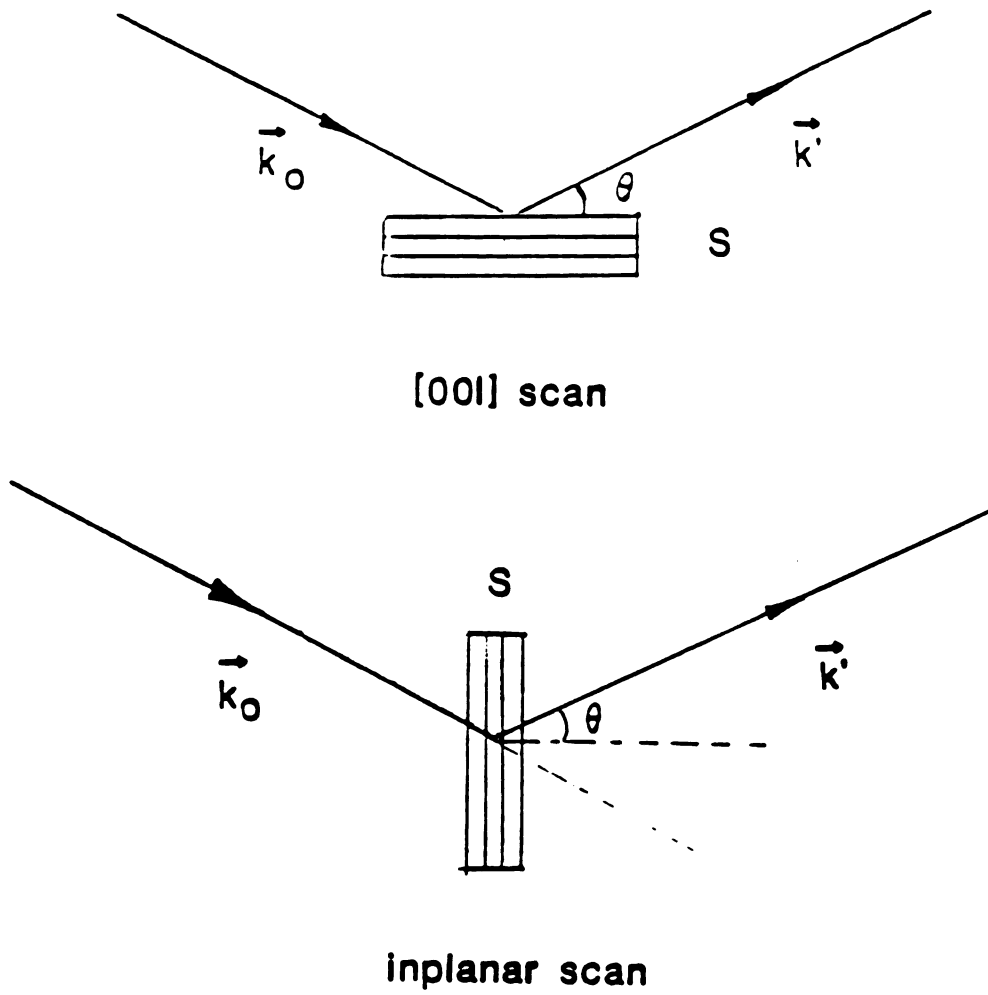


Fig. 1.10a A schematic diagram for (a) [001] scan and (b) inplane scan.

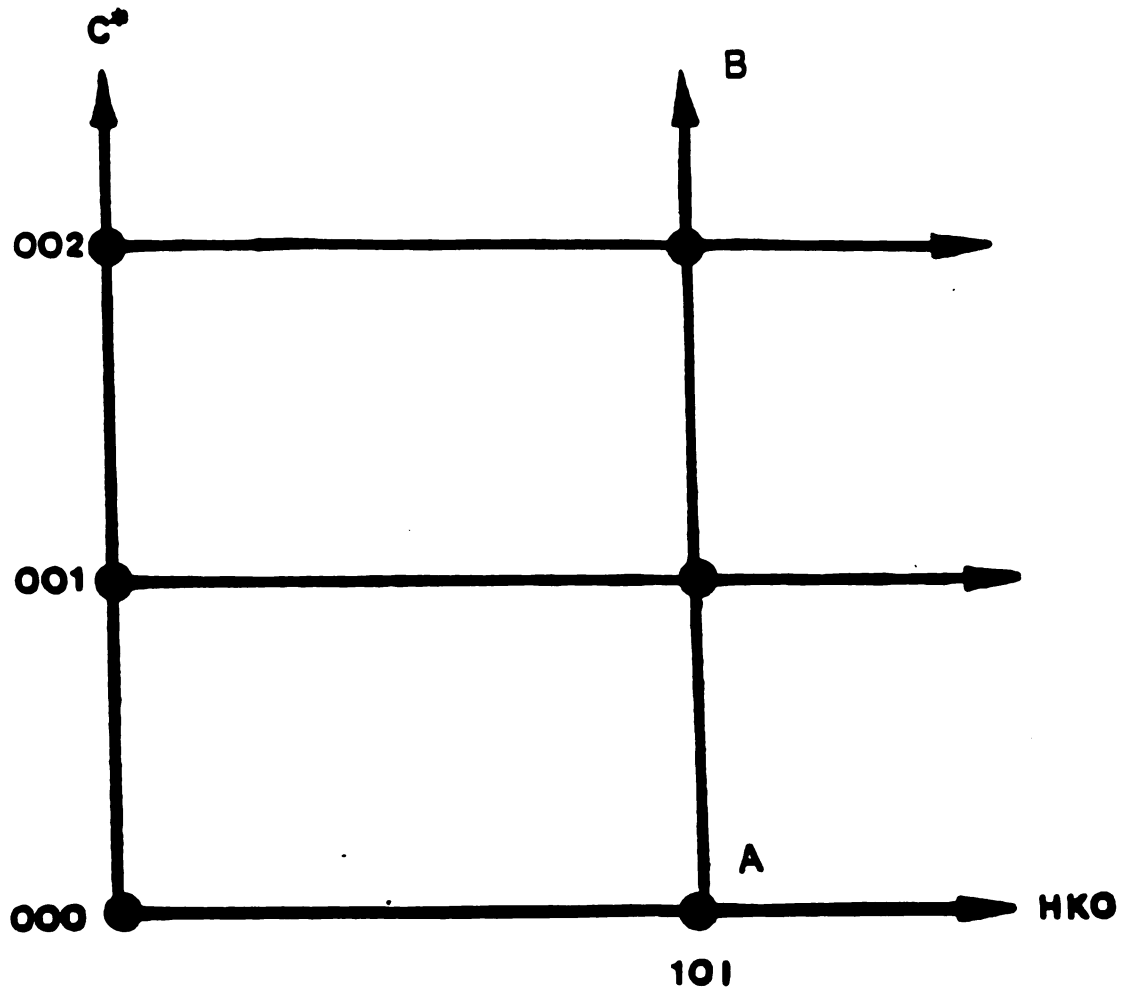


Fig. 1.10b A schematic diagram of a  $c^*$ -scan in reciprocal lattice.  $AB$  line represents a  $(10l)$   $c^*$ -scan.



configuration II, we can determine the frequencies of the transverse acoustic modes and the low energy optic modes propagating along the  $[00\ell]$  direction, i.e.,  $TA(0,0,\xi)$  and  $TO(0,0,\xi)$  modes. In configuration III, the shear modes can be measured. Note that all of the aforementioned configurations can be used the for constant-energy method.

References

1. K.V. Klitzing, Rev. Mod. Phys. 58, 519 (1986)
2. "Synthetic Modulated Structures", edited by L.L. Chang and B.C. Giessen, (Academic Press, Orlando, Florida, 1985); "Two-Dimensional systems, Heterostructures and Superlattices", edited by G. Bauer, F. Kuchar and H. Heinrich, (Springer Verlag, Berlin, 1984), Solid State Sciences, 53.
3. M.S. Dresselhaus and G. Dresselhaus, Adv. Phys. 30, 139 (1981).
4. S.A. Solin, Adv. Chem. Physics 49, 455 (1982).
5. S.A. Safran, Phys. Rev. Lett. 44, 937 (1980).
6. S.A. Safran and D.R. Hamann, Phys. Rev. Lett. 42, 1410 (1979).
7. M.E. Misenheimer and H. Zabel, Phys. Rev. Lett. 54, 2521 (1985).
8. G. Kirczenow, Phys. Rev. Lett. 52, 437 (1984).
9. H. Zabel, S.C. Moss, N. Caswell and S.A. Solin, Phys. Rev. Lett. 43, 2022 (1979).
10. A. Erbil, A.R. Kortan, R.J. Birgeneau and M.S. Dresselhaus, Phys. Rev. B28, 6329 (1983).
11. H. Zabel, S.E. Hardcastle, D.A. Neumann, M. Suzuki, and A. Magerl, Phys. Rev. Lett. 57, 2041 (1986).
12. H. Zabel, A. Magerl, A.J. Dianoux and J.J. Rush, Phys. Rev. Lett. 50, 2094 (1983).
13. A. Magerl, H. Zabel, and I.S. Anderson, Phys. Rev. Lett. 55, 222 (1985).
14. M. Suzuki, Phys. Rev. B33, 1387 (1986).
15. R. Clarke, J.N. Gray, H. Homma, and M.J. Winokur, Phys. Rev. Lett. 47, 1407 (1981).
16. M.J. Winokur and R. Clarke, Phys. Rev. Lett. 54, 811 (1985).

17. M. Kobayashi and I. Tsujikawa, J. Phys. Soc. Jpn. 46, 1945 (1979).
18. L.A. Pendry, R.A. Wachnik, F.L. Vogel, and P. Lagrange, Synthetic Metals 5, 277 (1983).
19. Y. Iye and S. Tanuma, Phys. Rev. B25, 4583 (1982).
20. A. Herold, C.R. Lebd, Seances Acad. Sci. 232, 838 (1951).
21. S.A. Solin and H. Zabel, Advances in Physics (in press).
22. H.E. Stanley, Introduction to Phase Transitions and Critical Phenomena, Oxford, New York, (1971).
23. P. Hansen, Physics Metallurgy, Cambridge Univ. Press, Cambridge, England, (1978).
24. P.F. Chow and H. Zabel, Syth. Met. 7, 243 (1983).
25. X.W. Qian, D.R. Stump, B.R. York, and S.A. Solin, Phys. Rev. Lett. 54, 1271 (1985).
26. X.W. Qian, D.R. Stump and S.A. Solin, Phys. Rev. B33, 5756 (1986).
27. Y.B. Fan, S.A. Solin, D.A. Neumann, H. Zabel and J.J. Rush, Phys. Rev. B36, 3386 (1987).
28. Y.Y. Huang, D.R. Stump, S.A. Solin and J. Heremans, Solid State Comm. 61, 469 (1987).
29. Y.Y. Huang, Y.B. Fan, S.A. Solin, J.M. Zhang, P.C. Eklund, J. Heremans, and G.G. Tibbets, Solid State Comm. 64, 443 (1987).
30. M. Suzuki, I. Oguro and Y. Jinzaki, J. Phys. C17, L575 (1984).
31. S.W. Lovesey, Theory of Neutron Scattering from Condensed Matter, (Clarendon Press, Oxford, 1984).
32. G.L. Squires, Introduction to the Theory of Thermal Neutron Scattering, Cambridge Univ. Press, Cambridge, England, (1978).
33. Neutron Scattering, edited by G. Kostorz, (treatise on materials sciece and technology; vol.15) (Academic Press, New York, 1979).

34. G.E. Bacon, Neutron Diffraction, (Clarendon Press, Oxford, 1975).
35. L.D. Landau, and E.M. Lifshitz, Quantum Mechanics, vol. 3 of Course of Theoretical Physics, Pergamon Press, Oxford, New York, Toronto, Sydney, Paris, Frankfurt, (1977).

## Chapter II.

Elastic Neutron Scattering Studies of the Structure of  
Graphite Intercalated with Potassium and Ammonia

## 2.1 INTRODUCTION

The ternary graphite intercalation compounds (GIC's)  $K(NH_3)_x C_{24}$  with compositions in the range  $0 \leq x \leq 4.38$  are a class of GIC's which exhibits unusual structural,<sup>1,2</sup> optical,<sup>3</sup> electrical<sup>4</sup> and kinetic<sup>5</sup> properties. For instance, diffuse X-ray scattering studies<sup>1,2</sup> coupled with Monte Carlo computer modeling indicate that the potassium-ammonia layers in  $K(NH_3)_{4.38}C_{24}$  constitute the two-dimensional (2D) structural analogue of the extensively studied bulk three-dimensional (3D) metal-ammonia solutions<sup>6</sup> which are notable for the metal-insulator (MI) transition which they exhibit.<sup>6</sup> In this recent study,<sup>1,2</sup> it was shown that a semiquantitative fit to the "liquid" structure factor can be obtained from a structural model in which all potassium ions are symmetrically 4-fold coordinated to ammonia molecules. One very interesting aspect of this work was that, unlike all binary GIC's studied to date,<sup>7,8</sup> the scattering could be described without including any modulation of the intercalant layer due to the graphite host. Thus, the potassium-ammonia layers could be treated as a "simple" 2D liquid at room temperature, presumably due to an enhanced intercalant-intercalant interaction. The origin of this increased interaction may be the back-transfer of electron charge from the carbon layers to the intercalant layers when  $KC_{24}$  is ammoniated.<sup>3,9,10</sup> This back-transfer, which amounts to about 0.2 e/K for  $x = 4.38$ , has been established by (00 $l$ ) X-ray diffraction studies,<sup>9</sup> proton NMR measurements,<sup>10</sup> and optical reflectivity measurements.<sup>3</sup> This effect may increase the intralayer binding in the K-NH<sub>3</sub> liquid while it would decrease the graphite-intercalant interaction. The back-transfer of

charge could therefore partially explain the reduction of the  $C_{33}$  elastic force constant in  $K(ND_3)_{4.38}C_{24}$ <sup>11</sup> compared to the corresponding binary compound  $KC_{24}$ .

In addition to exhibiting some structural properties which are analogous to bulk metal-ammonia solutions, recent electrical<sup>4</sup> and optical reflectivity measurements<sup>3</sup> of  $K(NH_3)_x C_{24}$  indicate related electrical behavior. Thus the opportunity exists of employing potassium-ammonia-graphite to study the 2D MI transition as well as the electronic crossover from 2D to 3D behavior by varying the stage of the K-NH<sub>3</sub> GIC as well as the composition. (A stage n GIC is one in which nearest pairs of intercalant layers are interspersed by n graphite layers in a structure that exhibits long range c-axis stacking order.) Moreover, the K-NH<sub>3</sub> graphite system has been shown to be the first GIC in which the intercalation and staging kinetics are dominated by simple 2D diffusion<sup>5</sup> rather than by the complex Lifshitz processes<sup>12</sup> associated with the formation of multidegenerate 2D domains<sup>13</sup> characteristic of binary GIC's.

Since each of the unusual properties of the K-NH<sub>3</sub> ternary GIC's is intimately related to the structure of the intercalant K-NH<sub>3</sub> layer, it is imperative to determine that structure as completely as possible. But it is well known from many studies of A-B binary disordered systems<sup>14,15</sup> that a definitive structure is difficult to determine from X-ray data alone because the structure factor is the convolution of three pair correlation functions which result from A-A, A-B, and B-B structural correlations. Thus, in principle, it is necessary to carry out three distinct scattering experiments to sort out the individual contributions to the structure factor. To date, however, our knowledge of the K-NH<sub>3</sub> intercalant structure derives solely from an in-plane (hk0) and c-axis (h = const., k = const., l) diffuse

scattering X-ray diffraction study. Accordingly, the purpose of this paper is to report elastic neutron scattering studies of  $K(\text{ND}_3)_x\text{C}_{24}$  and to use our results to further test the X-ray derived structural model of the 2D potassium-ammonia liquid intercalant layer. In this case, the use of neutrons complements the X-ray results quite well since the neutron scattering mostly reflects the ammonia-ammonia correlations while the X-rays are almost equally sensitive to K-K and K-ammonia correlations. Therefore, by referring the results to a particular structural model, it should be possible to reasonably characterize the structure.

## 2.1 EXPERIMENTAL METHODS AND RESULTS

Pyrolytic graphite with a typical mosaic spread of about  $5^\circ$  was cut into thirty pieces of dimension  $1.5 \times 1.0 \times 0.1 \text{ cm}^3$  which were intercalated to form binary stage-2  $\text{KC}_{24}$  GIC's using the standard 2-bulb method.<sup>16</sup> These pieces were then transferred in a glove box to an aluminum sample can and assembled in a package in which the specimens were separated by thin aluminum spacers and stacked with their c-axes well aligned. Care was taken to provide a region for subsequent expansion of the sandwich height upon ammoniation. The aluminum can was compression-sealed with a tapered stainless steel cap<sup>17</sup> to which was welded a stainless steel bellows valve for evacuation of the sample holder and admission of ammonia vapor.

To reduce the incoherent neutron scattering cross section, but enhance the coherent neutron scattering cross section, deuterated ammonia was used to synthesize the ternary GIC's studied here. The  $\text{ND}_3$  which was purchased with a stated purity of 99.95% was further purified by repeated exposure to sodium metal using procedures that are described in detail elsewhere.<sup>6,9</sup>

The neutron diffraction studies reported here were performed with a triple-axis spectrometer located at the National Bureau of Standards research reactor. All of our measurements were carried out with incident neutrons monochromated to an energy of 35.0 meV by a pyrolytic graphite monochromator [(002) reflection]. A 2 inch thick pyrolytic graphite filter was used to remove higher orders from the neutron beam. No analyzer crystal was used for the in-plane scans. The transmission of the sample was estimated to be in excess of 95% making multiple scattering corrections unnecessary. The Placzek corrections,<sup>18</sup> which arise from inelastically scattered neutrons, were also estimated to be less than 2%. The fast neutron background was found to be negligible as well. All measurements were performed at room temperature.

The ammoniation of  $KC_{24}$  was carried out by in-situ exposure of the sample to  $ND_3$  at a vapor pressure of ~9.5 atm. which was provided by a remote liquid ammonia reservoir held at room temperature. Intercalation to the 9.5 atm. saturation composition of  $K(ND_3)_{4.3}C_{24}$  required a post exposure period of approximately three hours during which repeated (00 $l$ ) scans were taken to monitor the intercalation process. These scans are shown in Fig. 2.1. Note first from Fig. 2.1a that the reflections observed prior to exposure to ammonia can be indexed to a pure stage-2 structure and provide a confirmation that the specimen was not degraded in the glove box transfer process. During the first hour of exposure, the system evolved from a pure stage-2 binary  $KC_{24}$  phase through a coexistence region (Fig. 2.1b) to a stage-1 ternary phase with composition  $K(ND_3)_{3.2}C_{24}$ . The ammonia content was determined by comparing the measured basal spacings of the stage-1 ternary phase with previous X-ray measurements<sup>9</sup> of the variation of basal spacing with composition. The post exposure period from approximately one

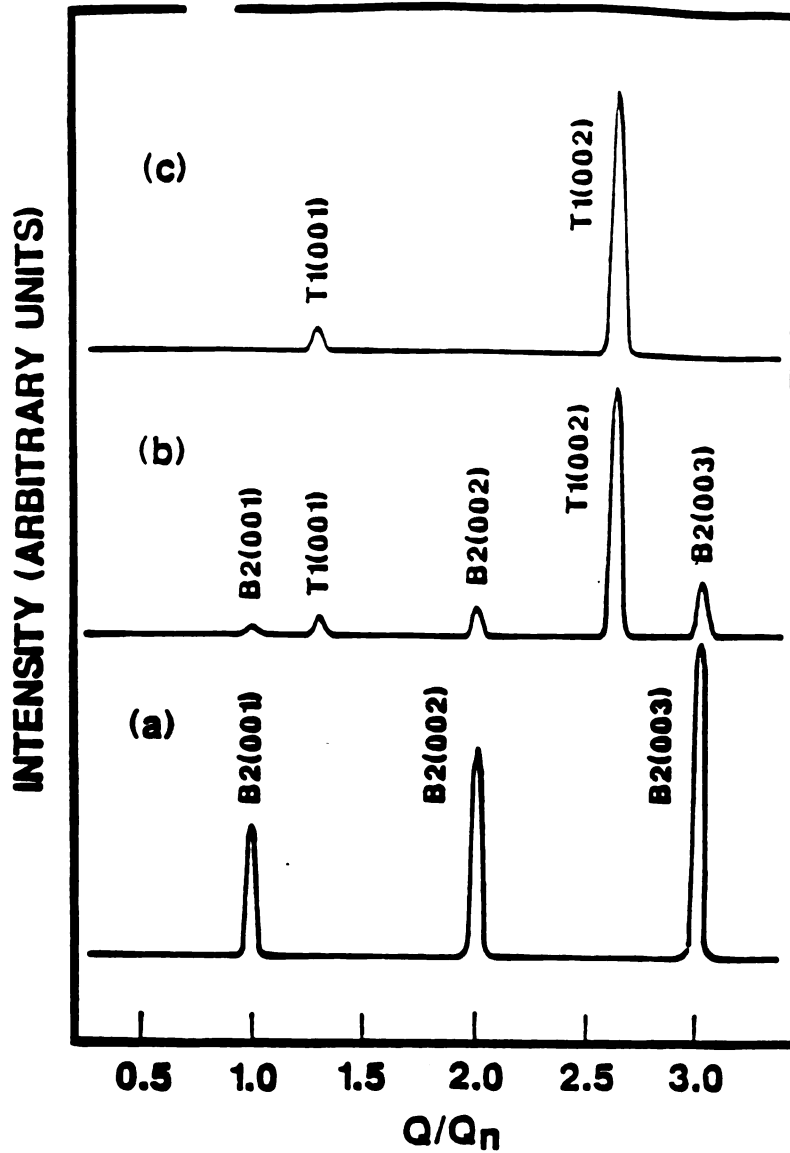


Fig. 2.1 The time evolution of the (00 $l$ ) elastic neutron scattering diffraction patterns of  $K(\text{ND}_3)_x\text{C}_{24}$  over the range  $0 < x < 4.3$  corresponding to an elapsed time of the exposure of  $\text{KC}_{24}$  to  $\text{NH}_3$  from 0 hrs (panel a) to > 3 hrs (panel c). The reflections are indexed according to the notation  $kn(00l)$  where  $k = \text{B}$  or  $\text{T}$  signifying respectively a binary or ternary GIC and  $n$  is the stage number. The abscissa is normalized in units of  $Q$ , the wave vector correspond. to the (001) reflection of  $\text{KC}_{24}$ .

to three hours is characterized by increased ammonia uptake of the pure stage-1 ternary phase until the saturation composition of  $K(\text{ND}_3)_{4.3}\text{C}_{24}$  was reached as indicated in Fig. 2.1c.

In addition to (00 $l$ ) scans, two other types of diffraction scans were employed in our studies. To measure the mosaic spread of the ternary phase and at the same time establish the c-axis stacking sequence, a (2.94 0  $l$ ) so-called  $c^*$  scan was taken. The results of this scan are shown in Fig. 2.2. The central broad peak of that figure indicates a mosaic spread of about  $10^\circ$  while the sharp carbon layer Bragg reflections at  $Q/Q_{c^*} = \pm 1$  result from an eclipsed ...A/A/A/... c-axis stacking sequence where A and / represent, respectively, crystalline carbon layers and liquid  $K\text{-ND}_3$  intercalate layers. The small shoulders at  $\pm 0.8\text{\AA}^{-1}$  in Fig. 2.2 are Bragg reflections from the aluminum sample can and spacers.

We carried out an additional  $c^*$  scan along the (20 $l$ ) direction in order to ascertain the degree of c-axis correlation between the disordered intercalate layers. The details of this scan which are shown in Fig. 2.3 will be discussed in section III. but we note here that it was chosen because it contains no carbon layer-derived Bragg reflections.

To conclude the presentation of our experimental results we show in Fig. 2.4a (solid line) an in-plane (hk0) scan of the diffuse scattering from the  $K\text{-ND}_3$  liquid layers. For clarity, the graphite and aluminum Bragg reflections have been removed from the diffraction pattern of Fig. 4a. For comparison and reference we also show in Fig. 2.4b (solid line) the corresponding X-ray measurement<sup>1,2</sup> of the in-plane diffuse scattering from the potassium-ammonia layers in graphite. As can be seen from Fig. 2.4, the X-ray and neutron diffraction patterns are quite similar, the major distinction between them being the strength of the first peak at  $0.8\text{\AA}^{-1}$ .

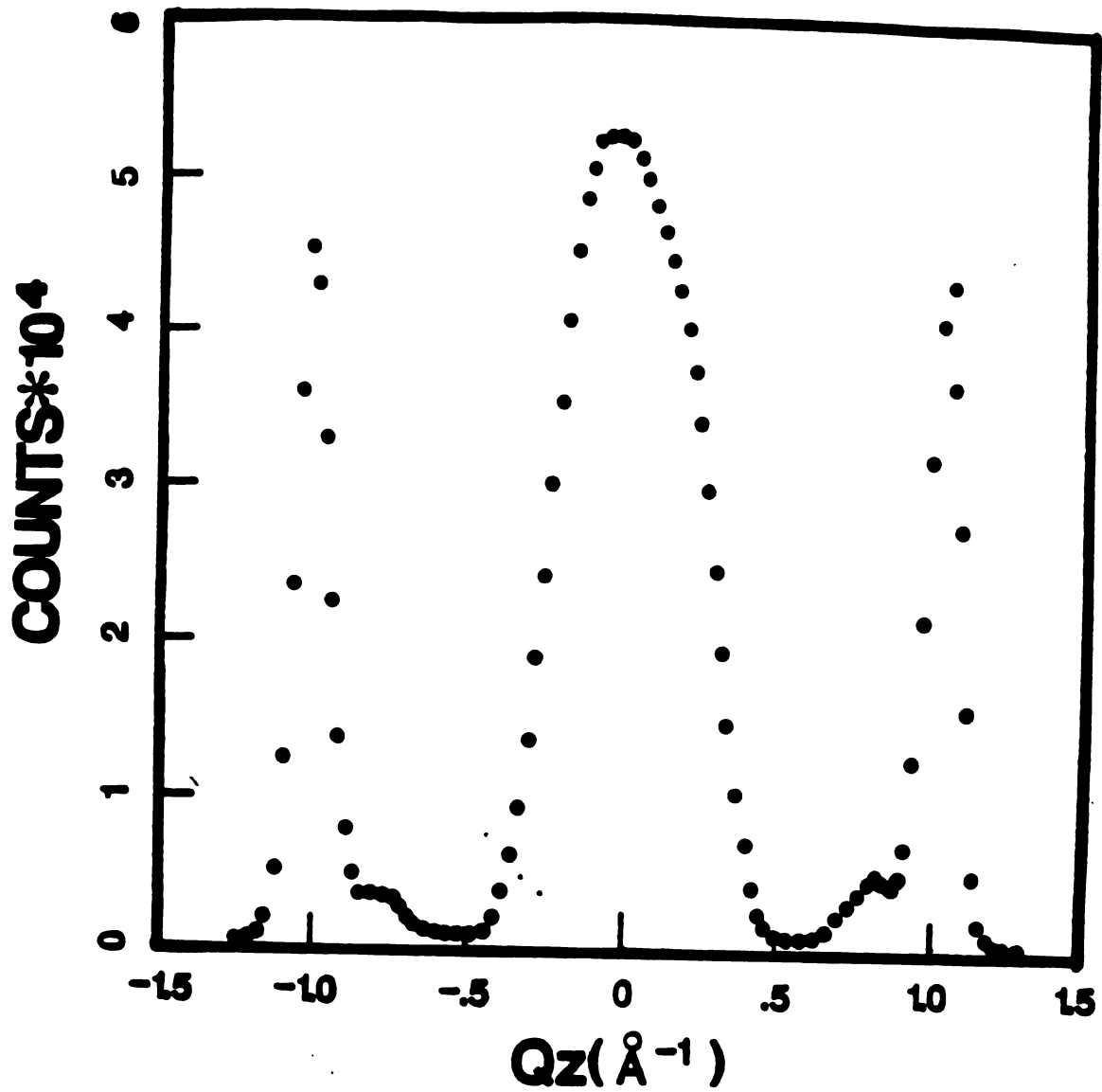


Fig. 2.2 A (2.93 0  $z$ )  $c^*$  scan of  $K(\text{ND}_3)_{4.3}\text{C}_{24}$ . Note:  $Q = 2\pi/d$ , where  $d$  is the  $c$ -axis repeat distance.

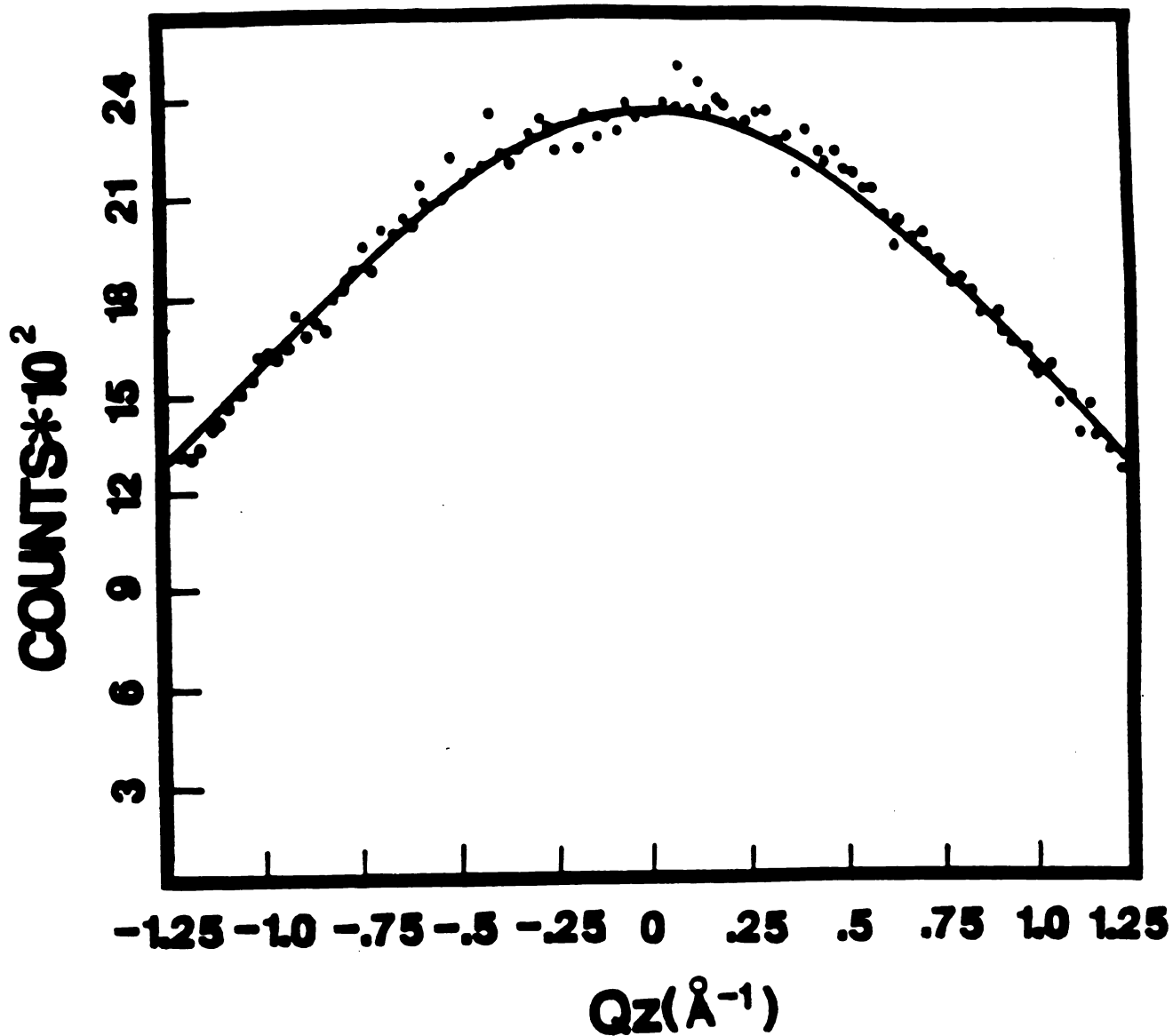


Fig. 2.3 A  $(2.0\ 0\ 2)$   $c^*$  scan (dots) of  $K(\text{ND}_3)_{4.3}\text{C}_{24}$ . The solid line was computed from the square of Eq. (2.6) of the text. Note:  $Q = 2\pi/d$ , where  $d$  is the  $c$ -axis repeat distance.

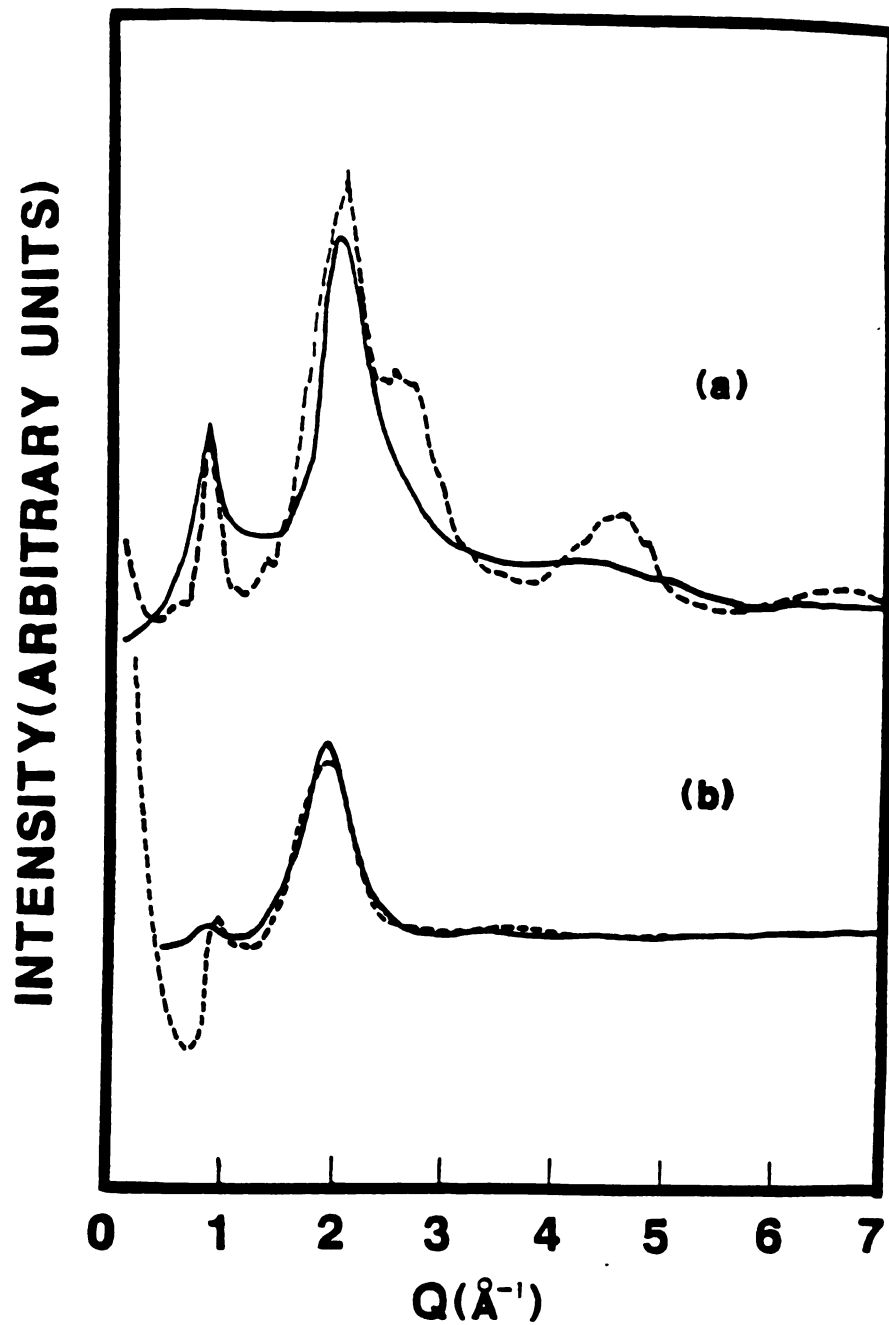


Fig. 2.4 (a) A comparison of the calculated (dashed line) and measured (solid line) in-plane diffuse neutron scattering intensity from  $K(\text{ND}_3)_{4.3}\text{C}_{24}$   
(b) The X-ray diffuse scattering result (solid line) and the calculated fit (dashed line) from the 4-fold cluster model.

This peak results from K-K scattering contributions<sup>1,2</sup> (see section V below) which, given the similar numbers of electrons on potassium and ammonia, are similar in strength to the K-NH<sub>3</sub> and NH<sub>3</sub>-NH<sub>3</sub> contributions that generate the second peak. In contrast the neutron cross section for potassium is much weaker than that of ND<sub>3</sub> and the first peak in the in-plane scattering is correspondingly much weaker than the second.

### 2.3 CALCULATIONS AND ANALYSIS

Two methods of analysis were applied to the data of Fig. 2.4a. In one, the real-space structural model of the atomic coordinates which had been previously applied<sup>1,2</sup> to explain the in-plane diffuse X-ray scattering data of Fig. 2.4b was used to calculate the corresponding neutron diffraction pattern of Fig. 2.4a. In the other, the planar radial distribution function (RDF) of the K-ND<sub>3</sub> liquid was determined from the Bessel-function back-transform of the neutron data. Although this latter method yields an RDF which is the sum of three pair correlation functions as noted above, the neutron scattering intensity is dominated by ammonia scattering and the back-transform represents primarily the ammonia-ammonia pair correlations.

#### A. The Real-Space Model Method

In a static neutron scattering experiment, the basic quantity that is measured is the structure factor given by<sup>18</sup>

$$\left(\frac{d\sigma}{d\Omega}\right)_{\text{coh}}^{\text{el}} = \langle |\sum_j \bar{b}_j \exp(i\vec{Q} \cdot \vec{R}_j)|^2 \rangle \quad (2.1)$$

where  $\vec{Q}$  is the scattering vector,  $\vec{R}_j$  is the position of the  $j^{\text{th}}$  nucleus,  $\bar{b}_j$  denotes that  $b_j$  is averaged over random nuclear spin-oriented and random isotope distributions and the angular brackets represent the average over all possible configurations of the nuclei. Using an appropriate structural model for the scattering medium (see section 3.4), we can calculate the coherent elastic cross section from Eq. (2.1).

We index the ammonia molecules by the label  $\ell$ . The position of the  $v^{\text{th}}$  nucleus relative to the center of mass of the  $\ell^{\text{th}}$  molecule is  $\vec{r}_{v(\ell)}$ . We denote the position of a potassium atom by the label  $\vec{r}_K$ . So

$$\begin{aligned} \vec{R}_j - \vec{R}_{j'} &= \vec{r}_j - \vec{r}_{j'} + \vec{r}_{v(\ell)} - \vec{r}_{v'(\ell)} \text{ for A-A} \\ &= \vec{r}_j - \vec{r}_{K'} + \vec{r}_{v(\ell)} \text{ for A-K} \\ &= \vec{r}_K - \vec{r}_{K'} \text{ for K-K} \end{aligned}$$

where A and K represent, respectively, ammonia and potassium. The cross section then becomes

$$\begin{aligned} \left(\frac{d\sigma}{d\Omega}\right)_{\text{coh}}^{\text{el}} &= \left\langle \sum_{\ell \ell'} \exp[i\vec{Q} \cdot (\vec{r}_\ell - \vec{r}_{\ell'})] \sum_{v(\ell)} \sum_{v'(\ell')} \bar{b}_{v(\ell)} \bar{b}_{v'(\ell')} \exp[i\vec{Q} \cdot (\vec{r}_{v(\ell)} - \vec{r}_{v'(\ell')})] \right\rangle \\ &+ \left\langle \sum_{\ell \ell'} \bar{b}_K \exp[i\vec{Q} \cdot (\vec{r}_\ell - \vec{r}_{\ell'})] \sum_{v(\ell)} \bar{b}_{v(\ell)} \exp(i\vec{Q} \cdot \vec{r}_{v(\ell)}) \right\rangle \\ &+ \left\langle \sum_{\ell_K \ell_{K'}} \bar{b}_K^2 \exp[i\vec{Q} \cdot (\vec{r}_{\ell_K} - \vec{r}_{\ell_{K'}})] \right\rangle \end{aligned} \quad (2.2)$$

Averaging over all 2D directions and separating the intramolecular and intermolecular scattering, we have

$$\begin{aligned} \left(\frac{d\sigma}{d\Omega}\right)_{\text{coh}}^{\text{el}} &= N_K \bar{b}_K^2 + \bar{b}_K^2 \sum_{\ell_K \neq \ell_{K'}} J_0(\vec{Q} \cdot |\vec{r}_{\ell_K} - \vec{r}_{\ell_{K'}}|) \\ &+ \bar{b}_K \left\langle \sum_{v(\ell)} \bar{b}_{v(\ell)} \exp(i\vec{Q} \cdot \vec{r}_{v(\ell)}) \sum_{\ell, \ell_K} J_0(\vec{Q} \cdot |\vec{r}_\ell - \vec{r}_{\ell_K}|) \right\rangle \\ &+ N_A (\bar{b}_N^2 + 3\bar{b}_D^2) + N_A \left\langle \sum_{v(\ell) \neq v'(\ell)} \bar{b}_v \bar{b}_{v'} \exp[i\vec{Q} \cdot (\vec{r}_v - \vec{r}_{v'})] \right\rangle \end{aligned}$$

$$+ \langle \sum_{\nu\nu'} \bar{b}_\nu \bar{b}_{\nu'} \exp\{i\vec{Q}\cdot(\vec{r}_\nu - \vec{r}_{\nu'})\} \sum_{\ell' \neq \ell} J_0[\vec{Q}\cdot(\vec{\ell} - \vec{\ell}')]\rangle \quad (2.3)$$

In Eq. (2.3) the first term is the self-scattering from the potassium nucleus, the second term is the internuclear scattering from potassium, the third term is the scattering from potassium-ammonia correlations, the fourth term is the self-scattering from the ammonia molecule, while the fifth term is the scattering from the correlations of different nuclei in the same molecule, and finally, the sixth term is the intermolecular scattering from ammonia.

To further clarify the important fifth and sixth terms of Eq. (2.3) we introduce the molecular form factor

$$F'(\vec{Q}) = \sum_{\nu} \bar{b}_\nu \exp(i\vec{Q}\cdot\vec{r}_\nu) \quad (2.4)$$

which describes the self interference within a single molecule and is due to the fact that a molecule is not a point scatterer of neutrons. From NMR<sup>10</sup> and quasielastic neutron scattering results,<sup>19</sup> it is known that the ammonia molecules are rotating rapidly about more than one molecular axis. Therefore, for the fifth term in Eq. (2.3) it is possible to treat the ammonia molecule as a uniform sphere of scattering length density. Then for the intramolecular scattering term one obtains

$$N_A [6 \bar{b}_N \bar{b}_D \left(\frac{3J_1(QR'_A)}{QR'_A}\right)^2 + 6 \bar{b}_D^2 \left(\frac{3J_1(QR'_A)}{QR'_A}\right)^2] 2. \quad (2.5)$$

where  $N_A$  is the number of ammonia molecules,  $J_1$  is the spherical Bessel function, and  $R'_A$  is the radius of the ammonia molecule which was used as a fitting parameter.

To calculate the form factor in the sixth term it is also possible to consider the ammonia molecule spherical in the intermolecular scattering term with an average radius  $R_A$  if one assumes that there are no directional correlations between the ammonia molecules. Then the molecular form factor, which contains no information on the orientation of the ammonia molecule with respect to the graphite planes, is given by

$$F'(\vec{Q}) = (\bar{b}_N + 3\bar{b}_D) \cdot \frac{3j_1(QR_A)}{QR_A} \quad (2.6)$$

and the sixth term in Eq. (2.3) becomes

$$|\langle F'(\vec{Q}) \rangle|^2 \cdot \sum_{\vec{Q}, \vec{Q}'} J_0\{Q \cdot (\vec{\ell} - \vec{\ell}')\} \quad (2.7)$$

Note that in the fitting procedure used, the radii  $R_A$  and  $R'_A$  were varied independently and that a best fit was obtained with the values 1.43Å and 1.55Å, respectively. The slightly larger value of  $R'_A$  is not unexpected since it is the average radius derived from the distribution  $P(r)$  of 2D discs which are used to model the in-plane structure while  $R'_A$  is the fixed radius of a 3D molecule. Moreover, the background scattering is sensitive to the value of  $R'_A$  while the structure in the scattering is not. Since our fit included only a constant background term small variations due to the Debye-Waller factor, multiple scattering, Placzek effects etc. may influence the derived value of  $R'_A$ . Finally, inspection of the intramolecular scattering fifth term shows that this term contains virtually no features at the small  $Q$ 's in question and yields only a sloping feature peaked at  $Q = 0$

which is characteristic of any form factor. Thus there is no physical significance of a small difference in the ammonia molecular radius between the fifth and sixth terms.

From Eqs. (2.3)-(2.6) we obtain the final form we need to calculate the diffuse scattering pattern.

$$\begin{aligned}
 \left(\frac{d\sigma}{d\Omega}\right)_{\text{coh}}^{\text{el}} &= N_K \bar{b}_K^2 + \bar{b}_F^2 \sum_{K \neq K'} N(r_{KK'}) J_0(Qr_{KK'}) \\
 &\quad + \bar{b}_K \langle F'(Q) \rangle \sum_{A,K} N(r_{AK}) J_0(Qr_{AK}) \\
 &\quad + N_A (\bar{b}_N^2 + 3\bar{b}_D^2) + N_A \left[ 6\bar{b}_N \bar{b}_D \left( \frac{3J_1(QR'_A)}{QR'_A} \right)^2 + 6\bar{b}_D^2 \left( \frac{3J_1(QR'_A)}{QR'_A} \right)^2 \right] \\
 &\quad + |\langle F'(Q) \rangle|^2 \sum_{A \neq A'} N(r_{AA'}) J_0(Qr_{AA'}). \tag{2.8}
 \end{aligned}$$

where  $N(r_{ij})$  is the number of atoms (molecules) at a distance  $r_{ij}$  from an atom (molecule) of type  $i$  to an atom (molecule) of type  $j$ . We use this formula in section V below to calculate the neutron scattering cross-section from the computer-generated liquid structure of Fig. 2.6.

### B. The Back-Transform Method

Now we address the theoretical method of the Bessel-function back transform. In Eq. (2.8), we change the sum into an integral and rewrite the formula as

$$\begin{aligned}
 \left(\frac{d\sigma}{d\Omega}\right)_{\text{coh}}^{\text{el}} &= N_K \bar{b}_K^2 + N_A (\bar{b}_N^2 + 3\bar{b}_D^2) \\
 &= 2\pi \int_0^\infty \bar{b}_K^2 P_{KK}(r) J_0(Qr) r dr + 2\pi \int_0^\infty \bar{b}_K \langle F'(Q) \rangle P_{KA}(r) J_0(Qr) r dr
 \end{aligned}$$

$$+ 2\pi \int_0^\infty |\langle F'_K(Q) \rangle|^2 P_{AA}(r) J_0(Qr) r dr \quad (2.9)$$

where  $P_{ij}(r)$  is the pair correlation function for atoms of type  $i$  and  $j$ , and has a similar physical meaning to  $N(r_{ij})$ .

The last term in Eq. (2.9) was derived from the last two terms of Eq. (2.8) as follows

$$\begin{aligned} N_A [6\bar{b}_N \bar{b}_D \left(\frac{3J_1(QR'_A)}{QR'_A}\right)^2 + 6\bar{b}_D^2 \left(\frac{3J_1(QR'_A)}{QR'_A}\right)] + |\langle F'(Q) \rangle|^2 \sum_{A \neq A'} N(r_{AA'}) J_0(Qr_{AA'}) \\ = |\langle F'(Q) \rangle|^2 N_0(Q, r) J_0(0) + |\langle F'(Q) \rangle|^2 \sum_{A \neq A'} N(r_{AA'}) J_0(Qr_{AA'}) \quad (2.10) \end{aligned}$$

Since  $N_0(Q, 0)$  is a slowly varying function of  $Q$ , Eq. (2.10) can be approximated as

$$\begin{aligned} |\langle F'(Q) \rangle|^2 [N_0(0) J_0(0) + \sum_{A \neq A'} N(r_{AA'}) J_0(Qr_{AA'})] \\ = |\langle F'(Q) \rangle|^2 \sum_{A, A'} N(r_{AA'}) J_0(Qr_{AA'}) \\ = |\langle F'(Q) \rangle|^2 \cdot 2\pi \int_0^\infty P_{AA}(r) J_0(Qr) r dr. \quad (2.11) \end{aligned}$$

We now introduce a convergence factor  $e^{-\alpha^2 Q^2}$  and a sharpening factor  $1/g^2(Q)^{15}$  into Eq. (2.9), where  $g(Q)$  decreases with increasing  $Q$  and  $\alpha$  is an adjustable parameter. We take  $g(Q) = |\langle F'(Q) \rangle|$  and define  $i(Q)$  as

$$i(Q) = \frac{\left(\frac{dr}{dQ}\right)_{\text{coh}} - N_K \bar{b}_K^2 - N_A (\bar{b}_N + 3\bar{b}_D^2)}{|\langle F'(Q) \rangle|^2} \quad (2.12)$$

Then, the Bessel-function back-transform is given by

$$\begin{aligned}
P(r) &= \int_0^{\infty} Qi(Q)e^{-\alpha^2 Q^2} J_0(rQ)dQ \\
&= 2\pi \int_0^{\infty} Qr \frac{\bar{b}_K^2 P_K(r)}{|\langle F'(Q) \rangle|^2} J_0(Qr)e^{-\alpha^2 Q^2} drdQ \\
&+ 2\pi \int_0^{\infty} \int_0^{\infty} Qr \frac{\bar{b}_K |\langle F'(Q) \rangle| P_{KA}(r)}{|\langle F'(Q) \rangle|^2} J_0(Qr)J_0(Qr)e^{-\alpha^2 Q^2} drdQ \\
&+ 2\pi \int_0^{\infty} \int_0^{\infty} Qr P_{AA}(r) J_0(Qr)J_0(Qr)e^{-\alpha^2 Q^2} drdQ \\
&\approx 2\pi P_{AA}(r) \propto P_{AA}(r)
\end{aligned} \tag{2.13}$$

In the last step of Eq. (2.13), we used the fact that contributions from K-K and K-A are negligible. In our calculation, the scale factor is not important, and the transform of a constant background only contributes to  $P_{ij}(r)$  at  $r = 0$ .

In computing the back transform of the experimental data of Fig. 2.4a, we normalized  $(\frac{d\sigma}{d\Omega})_{coh}^{el}$  to 1 at large  $Q$  and normalized  $F'(Q)$  to 1 at  $Q = 0$ , so

$$i(Q) = \frac{(\frac{d\sigma}{d\Omega})_{data} - 1}{|\langle F'(Q) \rangle|^2} \tag{2.14}$$

where  $(\frac{d\sigma}{d\Omega})_{data} - 1$  is equal to zero at large  $Q$ . To avoid the difficulty associated with zero values of the sharpening function (the denominator) in

Eq. (2.14), we incorporate an appropriate cut-off value,  $Q_m$ , in the integrals of Eq. (2.13) when calculating the back-transform of the neutron data.

#### 2.4 THE STRUCTURAL MODEL

We now discuss briefly the computer-generated structural model which we used to fit the in-plane X-ray scattering<sup>1,2</sup> (Fig. 2.4b) from potassium-ammonia liquid layers in  $K(NH_3)_{4.38}C_{24}$  and which we now further test by incorporation into the Real-Space Method to calculate the corresponding neutron diffraction pattern (Fig. 2.4a). The salient features of that model are illustrated in Figs. 2.5 and 2.6 and are enumerated below.

1. The  $K^+$  ions and the  $(NH_3)ND_3$  molecules are treated as hard infinitely thin discs oriented with their planes parallel to the carbon planes and located at the mid-point of the gallery along the graphite c-axis.
2. The radii of the  $K^+$  discs are identical and fixed at a value of  $1.46\text{\AA}$  which gave the best fit to the x-ray diffraction pattern consistent with the charge exchange to the graphite layer.
3. The model assumes a distribution of intermolecular distances,  $r_{KA}$  and  $r_{AA}$ , which is justified by the liquid dynamics of the system<sup>10,11</sup> for which  $S(Q)$  represents an ensemble average.
4. There are two types of ammonia molecule in the liquid, those which are 4-fold coordinated to potassium ions (open circles in Fig. 2.6) and those which are dynamically unbound (hatched circles in Fig. 2.6). The 4-fold coordinated  $K-ND_3$  clusters which result are assembled in a symmetric configuration so that the lines connecting the center of the  $K^+$  disc to each of the  $ND_3$  discs in a cluster make equal angles of  $\pi/2$ .

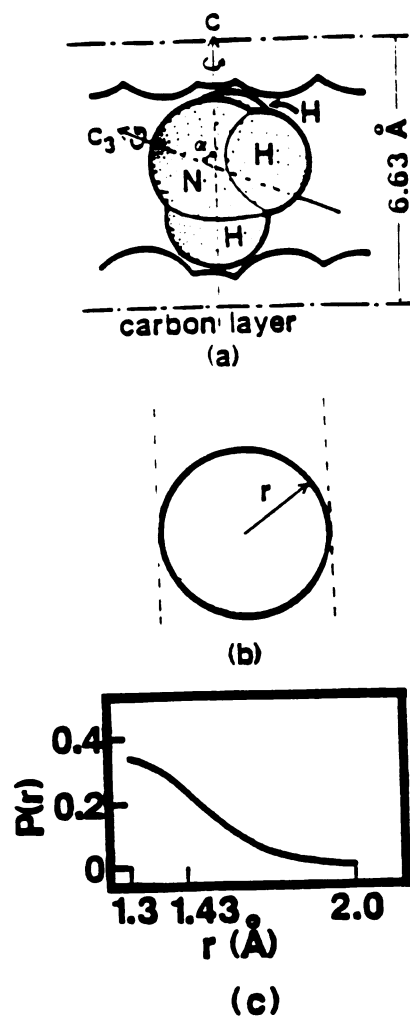


Fig. 2.5 (a) A schematic view of the tilted ammonia molecule between the graphitic planes. The arrows indicate rapid rotation of the molecule about its 3-fold axis which rapidly precesses about the graphite c-axis. The tilt angle between these two axes is  $\alpha$ . (b) The maximum cross-sectional projection of the ammonia molecule onto a plane parallel to the graphite planes. This projection defines the "hard disc" radius  $r$ . (c) The distribution of hard disc radii that results from the tilt angle distribution.

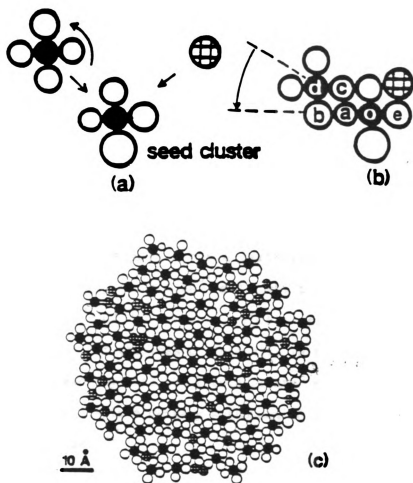


Fig. 2.6 Schematic representation of the mechanism by which 4-fold coordinated potassium-ammonia clusters are assembled to simulate a 2D liquid structure. Open (hatched) circles represent bound (free) ammonia molecules while the solid circles represent potassium ions. (b) Labels for reference in the text. (c) A portion of the simulated liquid structure.

5. The computer-generated collection of  $K\text{-ND}_3$  clusters and free  $\text{ND}_3$  discs is assembled (Fig. 2.6) in such a way as to maximize the in-plane density. The model contains 500  $K^+$  discs and 2165  $\text{ND}_3$  discs satisfying the stoichiometry  $K(\text{ND}_3)_{4.33}C_{24}$  where  $2165/500 = 4.33$ .
6. The effect of the graphite substrate potential on the structure of the  $K\text{-ND}_3$  liquid has been ignored.

We also generated 0-fold and 3-fold cluster models of the liquid structure of the  $K\text{-NH}_3$  layers using the procedures described above. The X-ray diffraction patterns calculated from these models yielded significantly inferior fits to the measured patterns as discussed in detail elsewhere.<sup>2</sup> For the 0-fold cluster model, the most notable deficiencies were a total loss of the first diffraction peak at  $0.8\text{\AA}^{-1}$  and a shift in the second peak from the correct position of  $2.0\text{\AA}^{-1}$  to  $2.3\text{\AA}^{-1}$ . Similar discrepancies occurred with the 3-fold model but the loss of intensity in the first peak was not total. It is also noteworthy that the 4-fold cluster model was the only one tested which yielded an in-plane density which was in agreement with the experimentally measured value.

## 2.5 CALCULATING THE DIFFRACTION PATTERN

In order to apply Eq. (2.8) to the above described structural model, it is necessary that there be no c-axis correlation between the individual potassium ammonia layers that contribute to the scattering. To experimentally confirm this point which has been initially established using X-ray scattering<sup>2</sup> we measured a  $(2.0\ 0\ 0)$   $c^*$  scan in the manner described in section 2.2. This scan is shown in Fig. 2.3 and the lack of short range order diffuse scattering is direct evidence that the potassium-ammonia layers are uncorrelated. The solid line in Fig. 2.3 represents the square of the

molecular form factor calculated from Eq. (2.6) for the corresponding positions in reciprocal space and provides an excellent fit to the experimental data.

The results we obtain by applying Eq. (2.8) to the 4-fold cluster model of Fig. 2.6c are shown in Figs. 2.7 a, b, and c which correspond respectively to the potassium-potassium, potassium-ammonia and ammonia-ammonia contributions. Notice immediately that the K-K contribution is only about 1/80 of that from A-A and that the sum of the three contributions (Fig. 2.7d and Fig. 2.4, dashed line) is essentially indistinguishable from that due to A-A alone. Moreover the weight of each contribution is only dependent on the stoichiometry of the sample and the stoichiometry of our model was chosen to be the same. Clearly then, ammonia contributions do indeed dominate the neutron scattering. This gives us the advantage of treating the system as monatomic and greatly simplifies the analysis of the back transform (see section 2.3).

In Fig. 2.4 we compare our calculated diffraction pattern with the experimentally measured pattern. Only four fitting parameters were used to achieve the fit shown in that figure. These are the molecular radii  $R_A = 1.43\text{\AA}$  and  $R'_A = 1.55\text{\AA}$ , a constant background, and a scale factor. Note that the molecular radii are indeed quite similar and are both physically reasonable. As can be seen, the fit is excellent in the range  $Q \geq 0.8\text{\AA}^{-1}$  but reveals serious discrepancies at lower values of  $Q$ . There are two reasons why these discrepancies did not appear in the X-ray studies. First, in X-ray diffraction the contribution from ammonia was much weaker, only half of the contribution from potassium. Second, x-ray data was obtained from the difference of two x-ray scattering intensity profiles using a "sample in/sample out" technique which may yield a large error at low  $Q$ .

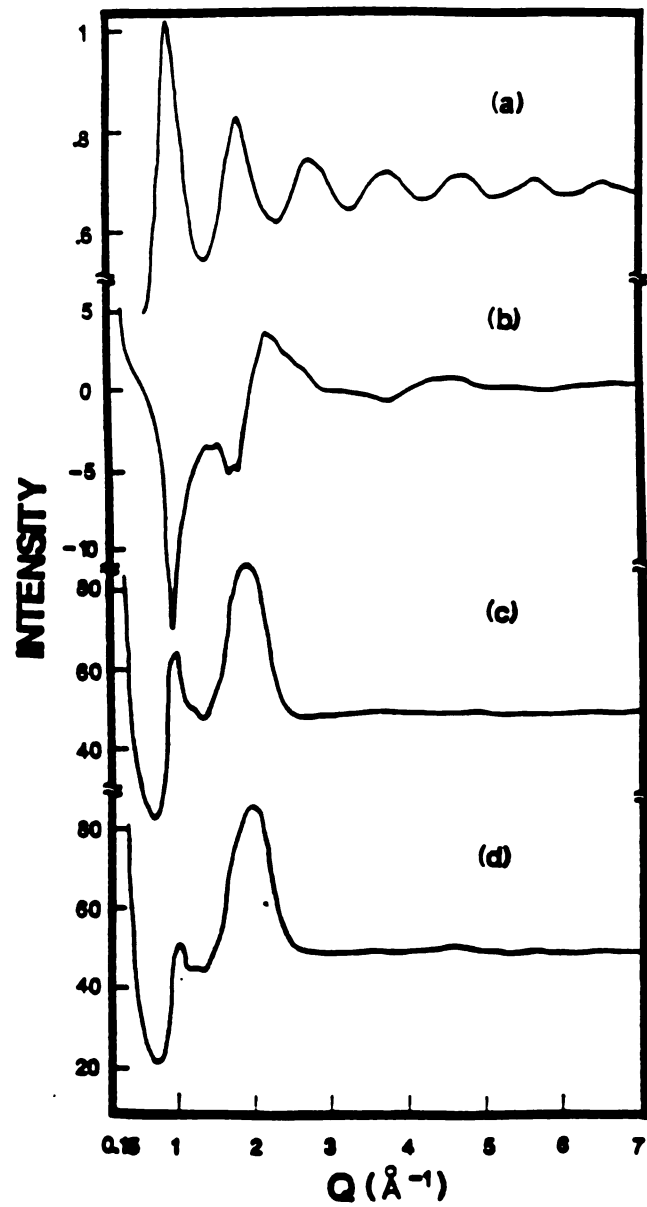


Fig. 2.7 Calculated contributions to the inelastic neutron scattering intensity from (a) potassium-potassium correlations, (b) potassium-ammonia correlations and (c) ammonia-ammonia correlations together with (d) the sum of (a), (b), and (c).

We can gain insight into the low  $Q$  discrepancy by considering the Bessel-function back-transforms shown in Fig. 2.8. In that figure the solid curve (Fig. 2.8b) is the ammonia radial density distribution deduced from the back-transform of the experimental data of Fig. 2.4 while the dashed curve (Fig. 2.8a) is the corresponding function determined from the 4-fold cluster structural model. Clearly, the latter exhibits much more sharp structure, the envelope of which is similar to the former. The sharp structure in Fig. 2.8a has physical meaning and corresponds to prominent distances in the model. For instance, the first peak in Fig. 2.8a corresponds to the nearest neighbor distance, a-b of Fig. 2.6b, the second peak represents the next-nearest neighbor distance, a-d of Fig. 2.6b, etc. But the broad first peak of Fig. 2.8b indicates that in the real potassium-ammonia 2D liquid, the first and second neighbor peaks are indistinguishable as are the third and fourth neighbor peaks. Thus, in the real fluid, the correlations are not as strong as indicated by the model.

The strong correlations in the model are a direct manifestation of the 4-fold symmetry imposed on the  $K\text{-ND}_3$  clusters. If that symmetry was to be relaxed so that the angular position of the ammonia molecules around the central potassium was random, interneighbor distances would be much more dispersed and the first two peaks in Fig. 2.8a would merge as would the third and fourth peaks. Note, however, that the second and third peaks would not merge since there is a  $K^+$  ion between atoms a and e in Fig. 2.6b. Also note that the high frequency component of Fig. 2.8a is a characteristic of the symmetric cluster while the low frequency component (the envelope) results from the 4-fold clustering and is independent of the angular symmetry in the cluster. Therefore, from the Bessel-function back-transform, it is clear that the high frequency components contribute to the

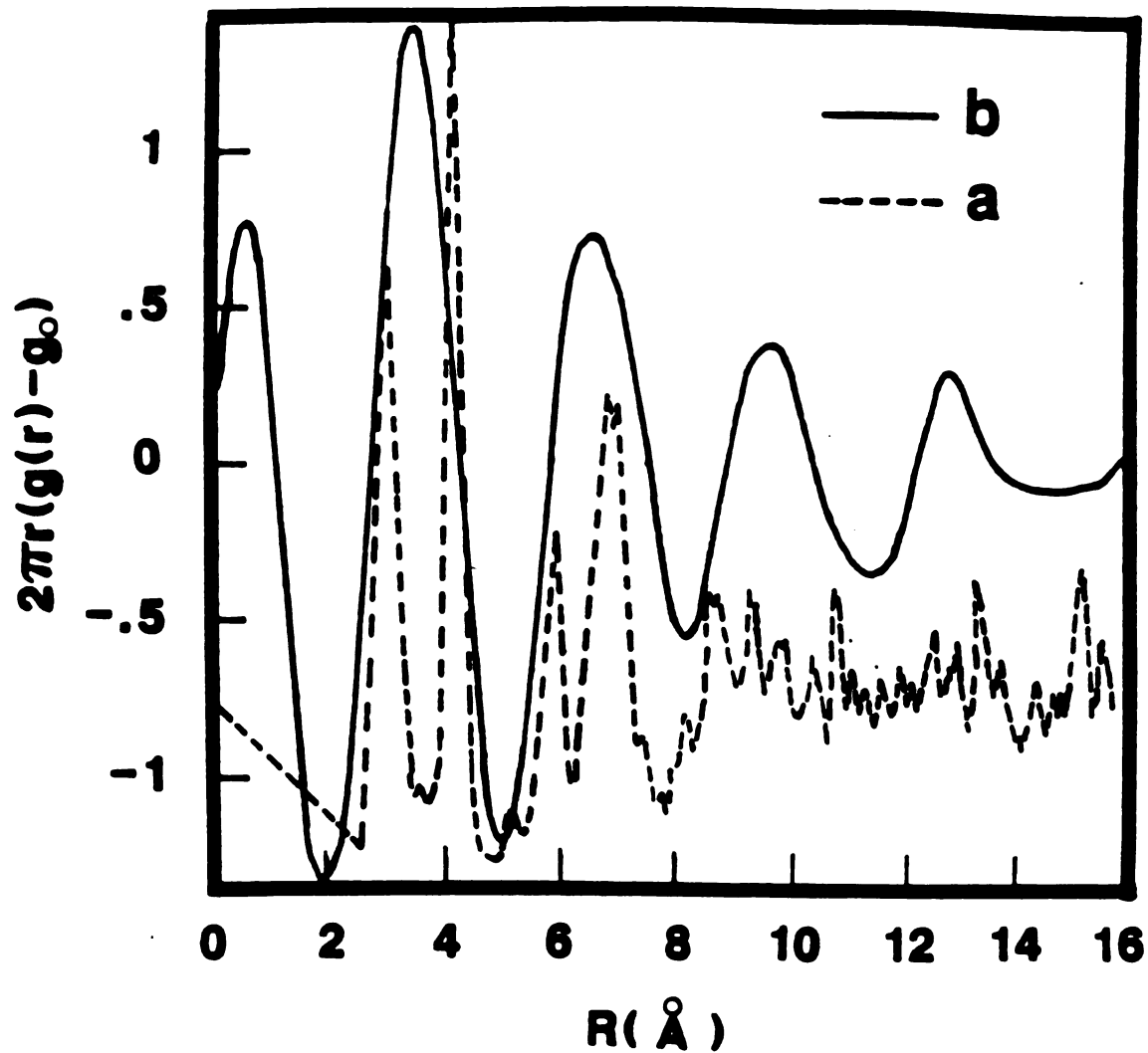


Fig. 2.8 The radial density distribution of  $K(\text{ND}_3)_{4.3}\text{C}_{24}$  deduced from (a) the 4-fold coordinated cluster model (dashed line) and (b) the Bessel-function back-transform of the experimental data (solid line) of Fig. 4a.

low Q discrepancy. Thus, if those components were absent from the radial density distribution as they are in Fig. 2.8b, the low Q discrepancy in the calculated diffraction would be minimized if not altogether absent. Finally, it is worth pointing out that the oscillations in Fig. 2.8b extend to large r due to the damping in Q-space which is imposed by the ammonia molecular form factor. Those oscillations are certainly not real, but rather are an artifact of the Bessel function back transform.

## 2.6 SUMMARY AND CONCLUSIONS

While the 4-fold cluster model contains the essential features of the structure of the 2D K-ND<sub>3</sub> liquid in graphite, the real liquid contains clusters with a much lower degree of rotational symmetry. This is, of course, to be expected since we know from NMR and quasielastic neutron scattering measurements that at room temperature the ammonia molecules are simultaneously rotating rapidly about their 3-fold axis while it precesses rapidly about the graphite c-axis. The molecules are also diffusing rapidly. An additional stimulus to reducing cluster symmetry is the pressure from unbound molecules which nudge between clusters and angularly displace their bound neighbors. Thus it would indeed be puzzling if the clusters preserved a high degree of internal symmetry. In principle, we could take the symmetry breaking into account analytically by parameterizing a probability distribution for the angular displacement of the ammonia molecules in a cluster. But we maintain, as in our X-ray work, that such an approach would require enough additional parameters to mask the essential physics and its structural consequences.

A few additional comments are warranted. In our 2D model for the diffraction, we used a 3D molecular form factor to compute the scattering. This approach is valid because the 2D model only relates to the positions of the molecular centers of mass in the graphite galleries. We have also tacitly assumed that the ammonia molecules are "rigid". Also our treatment of the molecules as spherical is very reasonable since they are in complex rapid motion and the structure factor takes an ensemble average over all orientations.

Finally, the calculated X-ray pattern<sup>1,2</sup> exhibits a peak of excess amplitude at  $4.8\text{\AA}^{-1}$  while no such peak is evident in the neutron

calculation. Though the X-ray data does show a small peak in the  $4.8\text{\AA}^{-1}$  region the calculated peak may result from the use of an oversimplified X-ray form factor which was computed from  $f_{\text{NH}_3} = f_{\text{N}} + 3f_{\text{H}}$ . That form factor decreases much more slowly with increasing  $Q$  than does the more accurate spherical type of form factor. Therefore, a high  $Q$  peak could have been inadequately quenched in the X-ray calculation. In addition, a convergence factor was not used in the X-ray analysis. Thus the X-ray calculation exhibited more noise than did the neutron calculation.

References

1. X.W. Qian, D.R. Stump, B.R. York and S.A. Solin, Phys. Rev. Lett. 54, 1271 (1985).
2. X.W. Qian, D.R. Stump and S.A. Solin, Phys. Rev. B33, 5756 (1986).
3. D.M. Hoffman, A.M. Rao, G.L. Doll, P.C. Eklund, B.R. York and S.A. Solin, *Mats. Res. Soc. Bulletin*, in press.
4. Y.Y. Huang, S.A. Solin, J. Heremans, and G.G. Tibbets, to be published.
5. Y.Y. Huang, D.R. Stump, S.A. Solin and J. Heremans, to be published.
6. J.C. Thompson, Electrons in Liquid Ammonia (Clarendon, Oxford, 1976).
7. S.A. Solin, *Adv. in Chem. Phys.* 49, 455 (1982).
8. M.S. Dresselhaus and G. Dresselhaus, *Adv. Phys.* 30, 139 (1981).
9. B.R. York and S. A. Solin, Phys. Rev. B31, 8206 (1985).
10. H.A. Resing, B.R. York, S.A. Solin and R.M. Fronko, *Proc. of the 17th Carbon Conference*, Lexington, 1985, p. 190.
11. D. Neumann, H. Zabel, Y.B. Fan, S.A. Solin and J.J. Rush, Phys. Rev. b36, 3386 (1987).
12. I.M. Lifshitz, *Zh. Eksp. Teor. Fiz* 42, 1354 (1962) [*Sov. Phys. JETP* 15, 939 (1962)].
13. H. Homma and R. Clarke, Phys. Rev. Lett. 52, 629 (1984).
14. S.A. Solin, in Structure and Excitations of Amorphous Solids, ed. by G. Lucovsky and F.L. Galeener (American Institute of Physics Press, Williamsburg, VA, 1976), p. 205.
15. B.E. Warren, X-ray Diffraction (Addison-Wesley, Reading, Mass., 1969).
16. A. Herold, *Bull. Soc. Chim. Fr.* 999 (1955).
17. H. Zabel, *Rev. Sci. Inst.* 54, 1413 (1983).
18. S.W. Lovesey, Theory of Neutron Scattering from Condensed Matter Vol. 1 (Clarendon, Oxford, 1984).

19. D. Neumann, Y.B. Fan, H. Zabel, S.A. Solin and J.J. Rush, to be published.

## CHAPTER III.

Inelastic Neutron Scattering Studies of stage-1  
and stage-2 K-Ammonia Intercalated Graphite

## 3.1 INTRODUCTION

In this chapter we address the time correlated properties of the K-ammonia graphite intercalation compound, or in other words the information contained in  $G'(r,t)$  and  $G''_S(r,t)$ . The use of coherent inelastic scattering allows one to investigate the properties of  $G'(r,t)$  which gives dynamic information such as phonon dispersion and librational excitations. One can measure the  $q$ -dependence of the excitation modes, which will yield information on their propagating nature. The phonons always display some dispersion which indicates that they are a collective excitation with a specific phase relation between the vibrating particles. Librations may or may not display such dispersion depending on whether or not they are collective excitations or are Einstein oscillators due to single-particle motions with no coherent phase relations.

Layered solids and some anisotropic molecular crystals have been extensively studied<sup>1-3</sup> due to their variety of kinetic, dynamical phenomena including orientational phase transitions, translation-rotation coupling, etc. Solids of this type are characterized by tight binding between atoms in a molecular unit which in turn is loosely bound to other molecules or to the surrounding atoms and by the strong anisotropy between interlayer and intralayer interactions. Some systems which have been heavily investigated include organic compounds adsorbed on the surface of graphite<sup>4-7</sup>; ammonia intercalated in  $TaS_2$ <sup>8</sup>;  $H_2$  and  $HNO_3$  intercalated in graphite<sup>9-11</sup>; and water intercalated in various forms of clay<sup>12-14</sup>.

Neutron scattering has been a powerful tool to study elementary excitations such as collective lattice vibrational modes, intramolecular modes, librational modes ("vibrational" excitations of a molecule which oscillates as a single unit in a hindered potential), molecular rotations, rotational tunneling and translational diffusion in a molecular crystal. One of the most important advantages of the neutron scattering technique is the ability to study the details of the interaction between those excitations. A fruitful system for such a study is the mixed alkali halide-cyanides. An interesting result from this system is that, in the low cyanide concentration limit, the [110] transverse acoustic branch (polarization [110]) splits due to phonon-libron hybridization<sup>15-16</sup>. Another split phonon dispersion curve has been reported<sup>17</sup> in the BGIC  $\text{RbC}_8$  but the mechanism of this splitting has not been determined unambiguously. It is probably due to coupling between the transverse optical mode of Rb and the [001]L phonon of graphite. Recently, we reported a coherent inelastic neutron scattering study of phonon-libron coupling in the layered TCIG,  $\text{K}(\text{ND}_3)_x\text{C}_{24}$ <sup>18</sup>. In that paper, several models have been proposed to explain the splitting. However, none of these models could consistently account for all of the experimental results. Here we present a more detailed analysis of the experimental data and provide a new model which consistently explains all of the data accumulated to date.

Despite the fact that the first K-ammonia TGIC was synthesized over 30 years ago<sup>19</sup>, systematic physical studies of this material have appeared only very recently. X-ray and neutron diffraction studies<sup>20-22</sup> have revealed that the structure of the intercalant layer is a two-dimensional liquid at room temperature and that the liquid structure factor can be reasonably well accounted for by a model in which four ammonia molecules are attached to a

single K-ion forming an ammonia-K cluster and the rest of the ammonia molecules are treated as free. The structure is depicted schematically in Fig. 3.1. In addition, NMR spectra have indicated on the average, the three-fold symmetry axis of the ammonia molecule lies parallel to the basal plane of the graphite<sup>23-25</sup>. A neutron quasielastic scattering study<sup>26</sup> (see Chapter IV) has shown that there are three different diffusion modes in the liquid layer. First, the ammonia molecule diffuses translationally in the gallery; second, it spins about its C<sub>3</sub>-symmetry axis; and third, the C<sub>3</sub> axis reorients or precesses about the graphite c-axis. Resistivity<sup>27</sup> and optical reflectance measurements<sup>28</sup> as a function of ammonia concentration have recently been interpreted in terms of a two-dimensional metal-insulator transition analogous to the three dimensional metal-insulator transition in bulk metal-ammonia solutions<sup>29</sup>. This transition was attributed to the back transfer of electrons from the carbon plane to the intercalant-layer where they are localized at lower ammonia concentration and delocalized above  $x=4.1$ <sup>27</sup>. The intercalant-graphite force constant  $\phi$  are expected to be reduced by back charge transfer and the associated lattice expansion which results from ammoniation. In this chapter, we will present inelastic neutron scattering measurements of the [001] longitudinal phonon dispersion of  $K(NH_3)_x C_{24}$ , and discuss the effects of charge transfer and lattice expansion on the force constant. We also will provide a detailed discussion of the mechanism for the libron-phonon coupling in K-ammonia TGICs.

### 3.2 EXPERIMENT AND RESULTS

Details of sample preparation have already been addressed in Chapter II and the general methodology for neutron scattering has been considered in Chapter I. Therefore, we will only briefly address here some additional

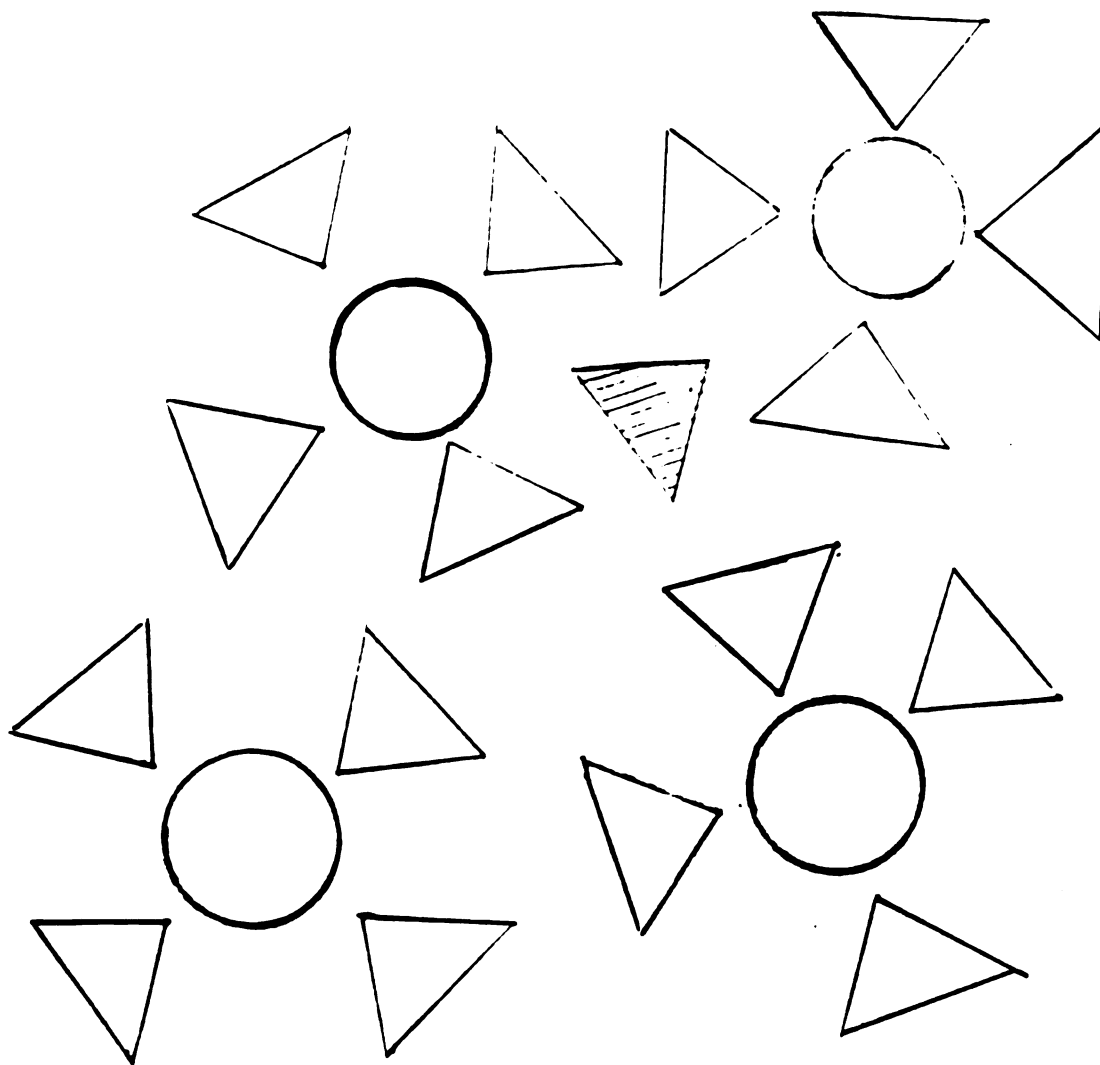


Fig. 3.1 A schematic Diagram of the inplane structure of  $K(NH_3)_4 \cdot 3C_{24}$ . The circles represent  $K^+$  ions, the open triangles represent  $NH_3$  molecules which are associated with a  $K^+$  ion, and the shaded triangle represents a "free" ammonia molecule.

aspects of the experimental procedure. After all measurements of  $K(\text{ND}_3)_x\text{C}_{24}$  were performed at  $x = 4.3$ , the  $\text{ND}_3$  concentration was reduced to  $x = 3.1$  by slowly removing ammonia vapor until a pressure of 0.20 atm was reached in the sample can. The ammonia fraction was determined using the results of York and Solin<sup>30</sup> who measured the composition dependence of the c-axis lattice parameter. The lattice parameter shift upon cointercalation was measured by repeated (00 $l$ ) scans and was found to be consistent with that measured by York and Solin<sup>30</sup>. The stage-2 sample was prepared in the same way as the stage-1 specimen but at a lower  $\text{ND}_3$  pressure. Neither the  $K(\text{ND}_3)_{3.1}\text{C}_{24}$  nor the stage-2  $K(\text{ND}_3)_{2.3}\text{C}_{28}$  compounds were pure stage samples<sup>31</sup>. Although the stage of interest was the dominant phase in each sample, care must be taken so that all phonons were measured in more than one Brillouin zone to assure that they were indeed associated with the periodicity of the phase of interest.

The neutron scattering results presented here were obtained using two triple axis spectrometers (BT-4 for stage-1 and BT-9 for stage-2 ) located at the National Bureau of Standards Reactor. Pyrolytic graphite was used as monochromator and analyzer crystals in both stations. All coherent scattering data present in this section were obtained in the constant Q mode with a fixed final energy of 13.7 meV and collimation of 40'-20'-40'-40' for the acoustic branch and 40'-40'-40'-80' for the optic branch, respectively. A one inch graphite filter was used to remove harmonic contamination. Other instrumental configurations were also used to eliminate the possibility of spurious observations. All of the measurements were performed at room temperature.

The measured [001] longitudinal phonon dispersion curves of stage-1  $K(\text{ND}_3)_{4.3}\text{C}_{24}$  are shown in Fig. 3.2. It is well known<sup>32</sup> that for a stage- $n$

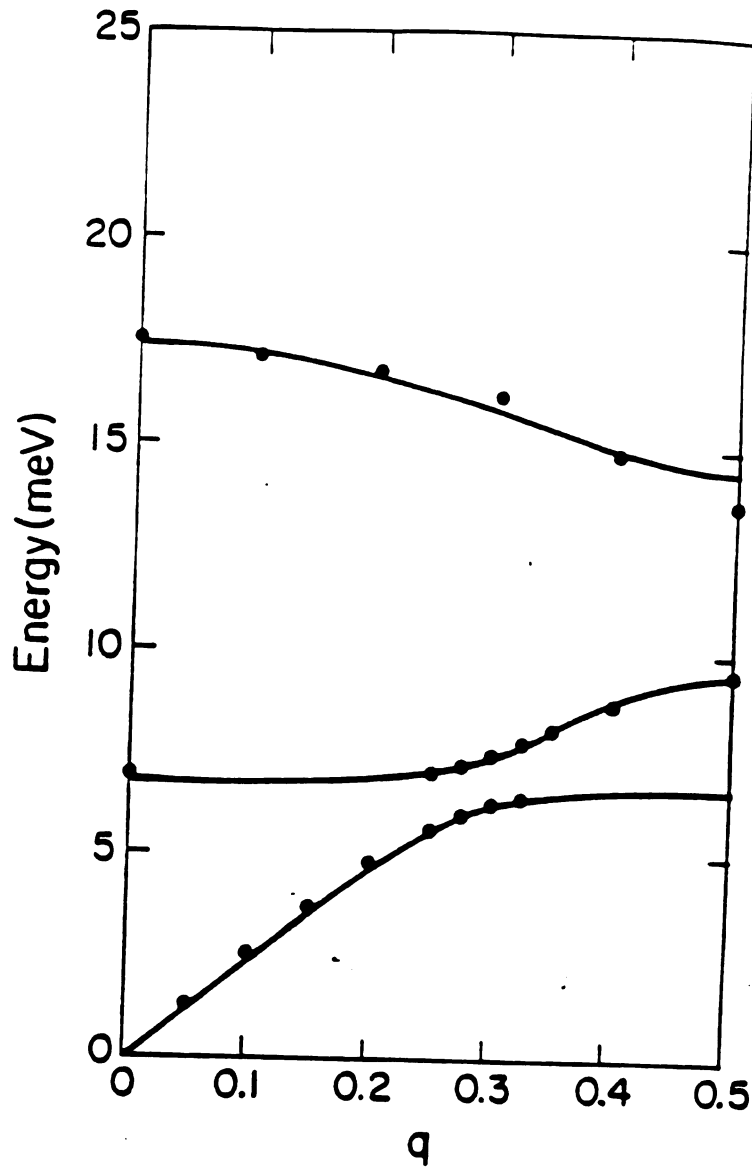


Fig. 3.2 [001]L phonon dispersion of stage 1  $\text{K}(\text{NH}_3)_{4.3}\text{C}_{24}$ . The solid line represents a fit using the dynamical matrix,  $A$ , described in the text.

compound there are  $n$  optical branches, and 1 acoustic one, of longitudinal phonon modes. In Fig. 3.2, we see clearly three phonon branches. Careful examination and comparison with the stage-1 binary counterpart indicates that the lower two branches of  $K(\text{ND}_3)_{4.3}\text{C}_{24}$  actually belong to the same acoustic branch which has been split into two parts due to the coupling of the phonon to a libron with an energy of about 6.7 meV. This phonon-libron coupling will be discussed in detail later. The [001] L phonon dispersion of the stage-1 compound  $K(\text{ND}_3)_{3.1}\text{C}_{22}$  are shown in Fig. 3.3. As can be seen, the phonon-libron coupling is also present in this compound but the librational energy has increased slightly to 7.1 meV and the splitting of the acoustic branch has been slightly reduced in comparison with  $K(\text{ND}_3)_{4.3}\text{C}_{24}$ .

The representative phonon-libron coupling effects are shown in Fig. 3.4 for three different values of wavevector  $q$  in units of  $2\pi/l_c$ . The solid line in that figure represents a two Gaussian fit to the experimental data. For  $q = 0.275$  and  $0.325$ , two peaks are evident. The less intense peak is broadened compared to the resolution function of the instrument while the more intense one is nearly resolution limited. At  $q = 0.30$ , the two peaks are almost equally intense and their combined width is broad compared to the resolution. Since the phonon lifetime is so long that all phonon peaks should be resolution limited, we assume that the broadened weak peak is a libron-like excitation. An attempt was made to observe the librational mode directly. The result of this effort is shown in Fig. 3.5. We performed the measurement at  $\vec{Q} = (0,0,3)$  ( $q = 0$ ) in order to avoid inelastic scattering from nearby phonons. The solid line in Fig. 3.5 again represents a two Gaussian fit to the data. The first fits the "background" from other inelastic scattering as well as elastic scattering, the second fits the librational mode yielding an energy of 7.1 meV and a width much broader than

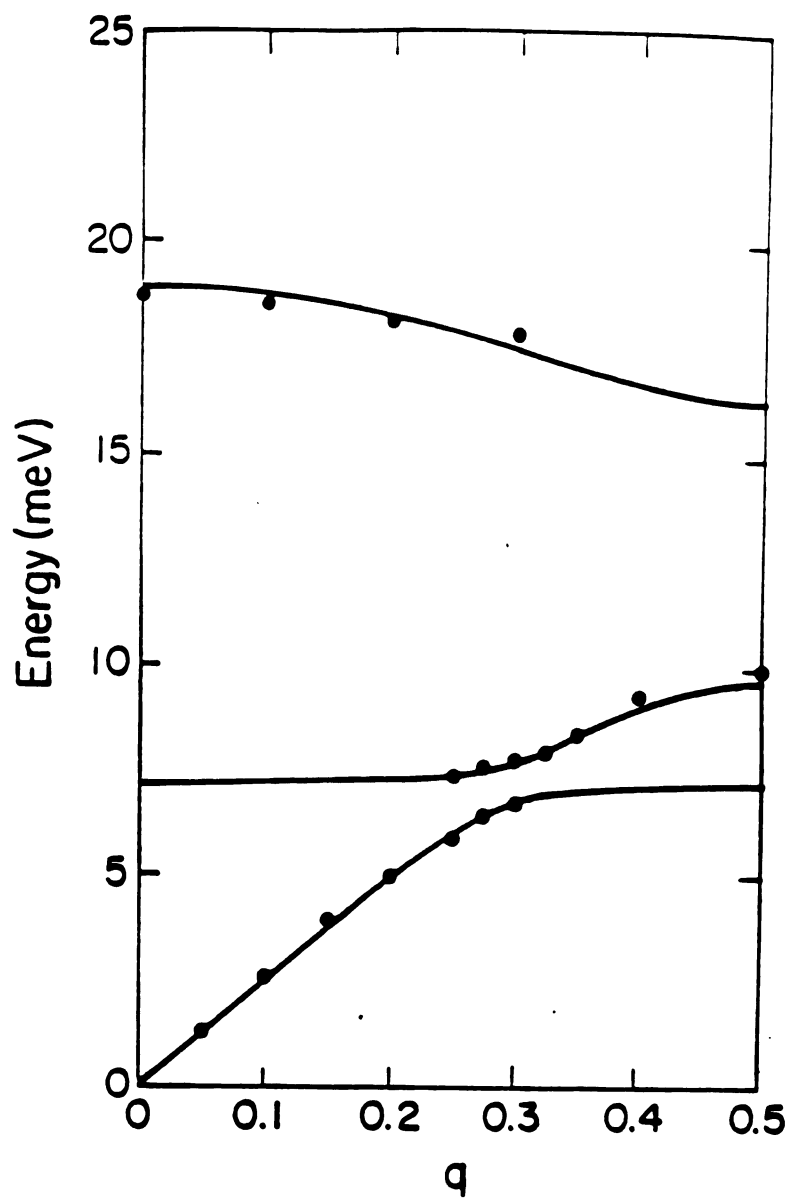


Fig. 3.3 [001]L phonon dispersion of stage 1  $\text{K}(\text{NH}_3)_{3.1}\text{C}_{24}$ . The solid line represents a fit using the dynamical matrix,  $A$ , described in the text.

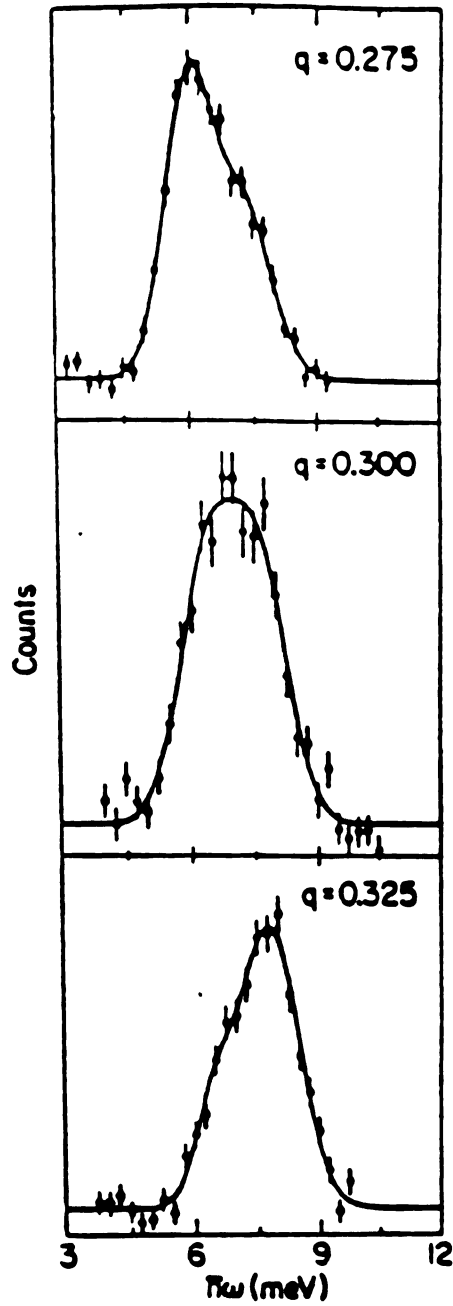


Fig. 3.4 Representative phonon groups at  $q=0.275$ ,  $0.300$ ,  $0.325$  for the compound  $\text{K}(\text{NH}_3)_{4.3}\text{C}_{24}$ . The solid lines are fits of the data to a sum of two Gaussians. The splitting due to phonon-libron coupling can be seen clearly, and the positions from such fits were plotted in Fig. 3.2.

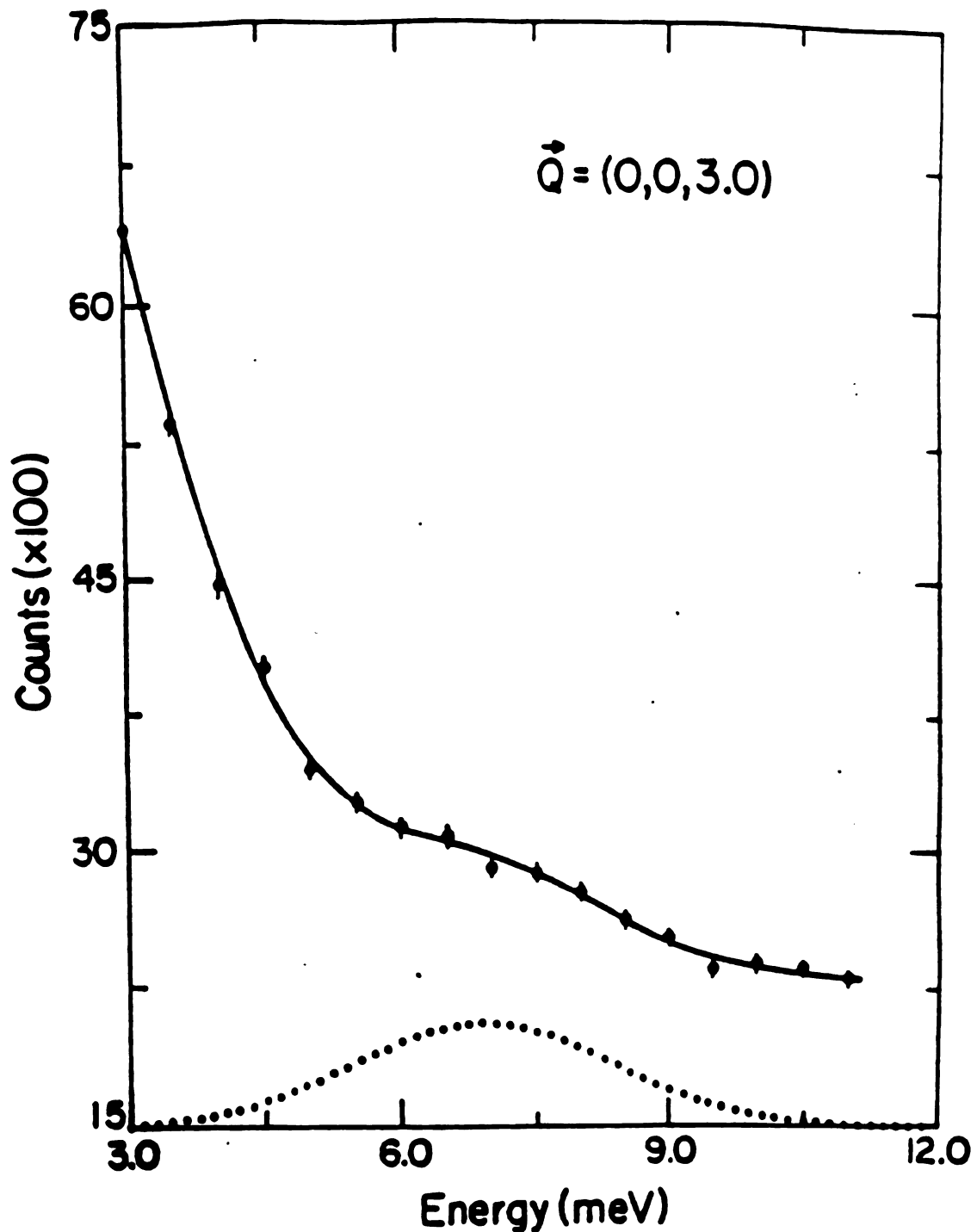


Fig. 3.5 Inelastic scan at  $\vec{q}=0$  ( $\vec{Q}=(0,0,3)$ ). The solid line is a fit to two Gaussian functions, one was fixed at  $E=0$  with a resolution limited width. The second peak is due to the librational excitation and has an energy of 7.1 meV and a width of 3.5 meV.

the instrumental resolution of 1.1 meV. The libron excitation energy of 7.1 meV is in good agreement with the value of libron-phonon coupling deduced directly from the phonon dispersion curves. This indicates that the libron is essentially dispersionless along the c-axis, implying that there is no collective motion in adjacent galleries. This is consistent with the absence of positional correlations observed in the elastic scattering<sup>22</sup>.

The measured phonon dispersion of the stage-2 compound  $K(\text{ND}_3)_{2.3}\text{C}_{24}$  is shown in Fig. 3.6. In spite of considerable effort, neither the upper optical branch nor the phonon-libron splitting was found. The failure to observe the upper optical mode could be due to the higher excitation energy and the lower concentration of  $\text{ND}_3$  in the stage-2 compound. The absence of the splitting is due to the fact that the energy of the librational excitation, which exists at  $\sim 10$  meV according to our model (see next section), falls within the Brillouin zone boundary gap of the stage-2 compound causing the phonon-libron coupling to disappear. Therefore, in order to determine the existence of this libron mode, one would have to observe the excitation directly and unambiguously. However, several facts make this impossible. First, the  $K(\text{ND}_3)_{2.3}\text{C}_{28}$  was not a pure phase, so that some stage-1 regions were also present; since the libron is dispersionless, it is impossible to distinguish whether the observed scattering was due to a libron from stage-2 or if it came from the stage-1 regions. Second, the lifetime of the libron is short and its intensity is very weak. Finally, the ammonia concentration is low and this in turn causes the total scattering cross-section to be reduced so that the observation becomes even more difficult.

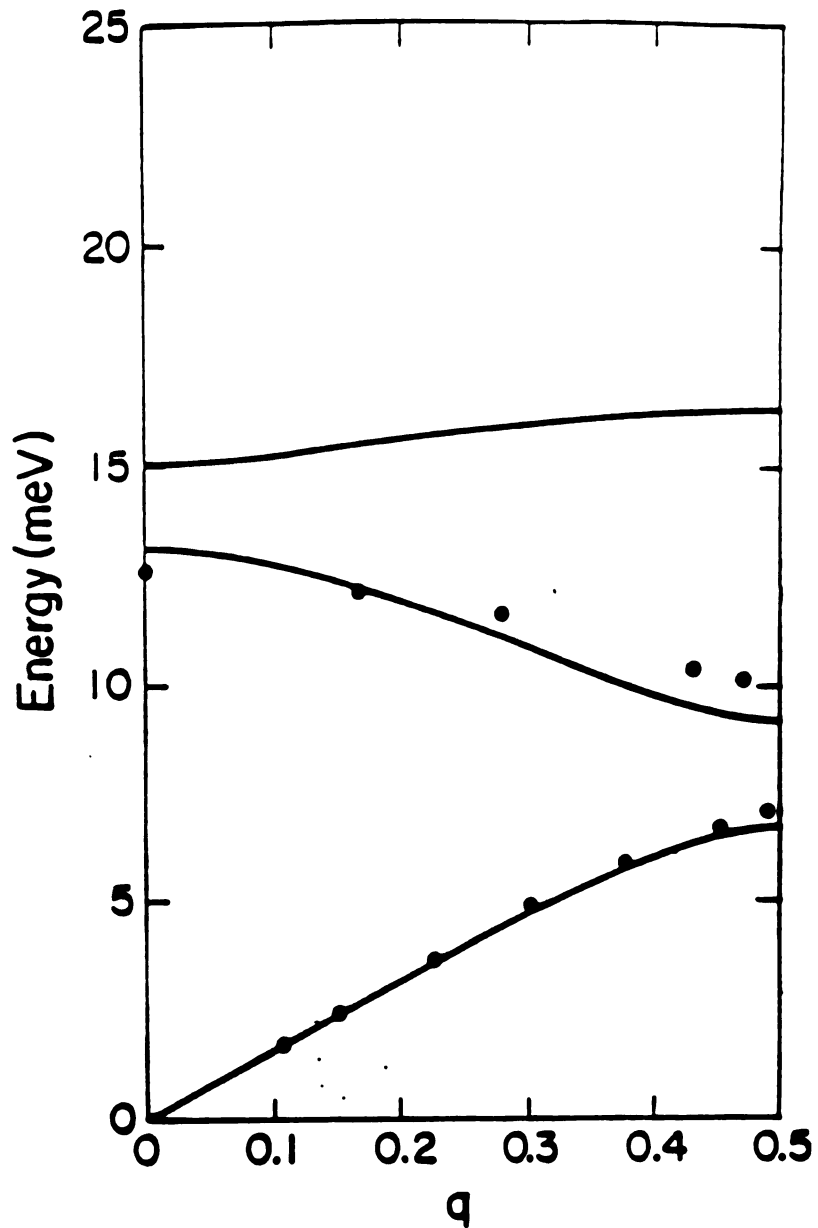


Fig. 3.6 [001]L phonon dispersion of stage 2  $K(ND_3)_{2.3}C_{24}$ . The solid line represents a simple two force constant Born-von Karman model discussed in the text.

## 3.3 DISCUSSION

In order to interpret the observed phonon dispersion relations, a 3×3 dynamical matrix, A, was employed in Ref. [18] to account for the split phonon dispersion curve. The dynamic matrix A contains a virtual crystal, one-force constant Born-von-Karman model, an Einstein oscillator of energy  $\alpha$  representing the libration, and a coupling term with strength coefficient  $\gamma$ .

$$A = \begin{vmatrix} \frac{\phi}{M} & \frac{\phi}{\sqrt{Mm}}(1+e^{iqI}) & \gamma\alpha(1-e^{i2qI}) \\ \frac{\phi}{\sqrt{Mm}}(1+e^{-iqI}) & \frac{\phi}{m} & 0 \\ \gamma\alpha(1-e^{-i2qI}) & 0 & \alpha^2 \end{vmatrix}$$

Here  $\phi$  is the intercalate-graphite force constant per carbon atom, M is the areal carbon mass density, m is the areal intercalate mass density per carbon atom, and the I is the c-axis lattice constant. The best fit to the measured phonon dispersion relations using this dynamic matrix yielded the parameters given in Table 3.1. From this table we see that  $\phi$ , the force constant per carbon atom, is essentially independent of the  $\text{ND}_3$  concentration, x. This implies that the K-graphite interaction is the dominant factor in determining  $\phi$  since the ratio of K to C is nearly constant in the two stage-1 compounds, and also that the elastic interaction is probably more important than the electrostatic interaction in determining  $\phi$ . This is in agreement with the fact that the K- $\text{ND}_3$  interaction is strong and the  $\text{ND}_3$ -C interaction is weak. It should be noticed that the increase of back charge transfer and lattice parameter with ammoniation tend to decrease  $\phi$ . On the other hand, the increase of x must strengthen the ammonia-graphite interaction. Therefore it is difficult to draw any unique conclusion from the charge transfer effect, since it depends on the

Table 3.1. Best fit parameters for the [001]L modes of two stage 1 K-ammonia intercalated graphite compounds by use of dynamic matrix A.

Compounds	$\phi$ (dyn/cm)	$\alpha$ (mev)	$\gamma$ (mev)
$K(ND_3)_{4.3}C_{24}$	2090	6.7	0.70
$K(ND_3)_{3.1}C_{24}$	2120	7.1	0.49

competition between those interactions. The slight reduction of the libration energy with increased  $x$  can be interpreted by the fact that the  $c$ -axis lattice parameter increases as  $x$  increases, reducing the curvature of the potential and therefore the energy of the libration.

In Fig. 3.6, the solid line represents the fit with a two parameter Born-von-Karman model for the stage-2 compound  $K(ND_3)_{2.3}C_{28}$ . Because of the lack of the upper branch of the optical mode in this sample, we were unable to fit the data in an unambiguous way. A graphite-graphite nearest-neighbor force constant of 2900 dyn/cm, consistent with the values obtained for the stage-2 binary compounds<sup>33</sup>, was assumed, and the intercalate-graphite force constant,  $\phi=2100$  dyn/cm, obtained from the stage-1 results and determined to be independent of the intercalate concentration, gives the best fit.

The sound velocity  $v_s$  and elastic constant  $C_{33}$ , determined from the initial slope of the acoustic branch is given for  $K(ND_3)_x C_{24}$  as well as the values for the stage-1  $KC_8$  in Table 3.2. It clearly shows that there is essentially no difference between the two compositions of the K-ammonia compounds studied here, but both  $v_s$  and  $C_{33}$  are substantially reduced compared to the binary  $KC_8$ . Two possible reasons accounting for this reduction were proposed. The first, and most important effect was the large expansion of the  $c$ -axis of the ternary compound. The second possible reason may be the back charge transfer to the intercalate layer in the K-ammonia compound. From the previous discussion concerning  $\phi$ , we know that the electronic effects are unimportant within the accuracy of the present data. The sound velocity and  $C_{33}$  for the stage-2 ternary compound are also shown in Table 3.2 along with the results for the binary stage-2 compound  $KC_{24}$ . The reduction of  $C_{33}$  for the ternary compound compared to the binary compound is apparent for the stage-2 compounds, though it is not as dramatic

Table 3.2 Elastic constants and sound velocities for K-ammonia intercalated graphite along with the analogous binary compounds.

Compounds	Stage	$C_{33} (\times 10^{11} \text{ dyn/cm})$	$V_s (\times 10^5 \text{ cm/sec})$
$\text{KC}_{24}(\text{ND}_3)_{4.3}$	1	1.71 0.10	3.22 0.10
$\text{KC}_{24}(\text{ND}_3)_{3.1}$	1	1.62 0.10	3.18 0.10
$\text{KC}_{24}(\text{ND}_3)_{2.3}$	2	2.94 0.10	3.90 0.10
$\text{KC}_8$	1	4.85 0.14 <sup>a</sup>	4.91 0.07 <sup>a</sup>
$\text{KC}_{24}$	2	3.71 0.15 <sup>a</sup>	4.33 0.15 <sup>a</sup>

<sup>a</sup>After H.Zable and A.Magerl, Phys. Rev. B25, 2463 (1982).

as it was for stage-1. The fact that stage-1 ternary compound is softer than the stage-2 ternary compound is because stage-1 contains more "soft" intercalate-graphite bonds than does the stage-2 ternary.

The large width of the librational peak indicates that the librational potential is probably quite anharmonic so that the splitting between levels is not at all constant.

Note that the coupling constant  $\gamma$  scales approximately with the ammonia concentration<sup>18</sup>. This seems to be evidence that the librons couple to the phonons individually. However, further study shows that this scaling phenomenon may be an artificial effect since this phenomenological description is not universal.

Consider a dynamical matrix B which is similar but not identical to A:

$$B = \begin{vmatrix} \frac{\phi}{M} & \frac{\phi}{\sqrt{Mm}}(1+e^{iqI}) & 0 \\ \frac{\phi}{\sqrt{Mm}}(1+e^{-iqI}) & \frac{\phi}{m} & \gamma\alpha(1-e^{2iqI}) \\ 0 & \gamma\alpha(1-e^{i2qI}) & \alpha^2 \end{vmatrix}$$

In this matrix all terms are the same as in matrix A, except the coupling term is placed at a different position (compare with A). The quality of the fit for both matrices is equivalent and the fitting parameters are given in Table 3.3. As can be seen, the force constant  $\phi$  and the libration energy  $\alpha$  are the same to within experimental error as those from matrix A given in Table 3.1. The only difference is in the coupling constant  $\gamma$  which for matrix B is independent of ammonia concentration. This leads us to conclude that the coupling interaction is due to K-graphite, which contradicts the previous model. Thus, both dynamical matrices are deficient and any interpretation for the libron-phonon coupling based on them is necessarily

Table 3.3 Best fit parameters for the [001]L modes of two stage 1 K-ammonia intercalated graphite compounds by use of dynamic matrix B.

Compounds	$\phi$ (dyn/cm)	$\alpha$ (mev)	$\gamma$ (mev)
$K(ND_3)_{4.3}C_{24}$	2090	6.7	1.22
$K(ND_3)_{3.1}C_{24}$	2120	7.1	1.23

ambiguous. In addition, the coupling term contains  $\exp(2qI)$  which imply that there are coupling interactions between second nearest layers. This is physically unreasonable and in conflict with the fact that the intercalate layers are uncorrelated and the intercalate-intercalate interaction is very weak. Therefore, a new approach to the problem is warranted. In that approach we construct a dynamical matrix according to a vibrational model and test the resultant fit to the phonon dispersion curves.

Several possible models which are independent of the description by the dynamical matrix A were discussed in reference [18]. We consider those models first. As discussed in reference [18], it is unlikely that the libration is due to the oscillation of an individual ammonia molecule dipole in a potential provided by the K-ion since the energy estimated for this motion is much higher than the measured value of  $\sim 7$  mev. In contrast, the K-ammonia bond-bending (umbrella) mode in which motion occurs principally out of the basal plane was estimated to be roughly in the right energy range. We approximate this bond-bending mechanism by the force constant model depicted in Fig 3.7. The dynamical matrix for this model can be determined rigorously and is given as C below.

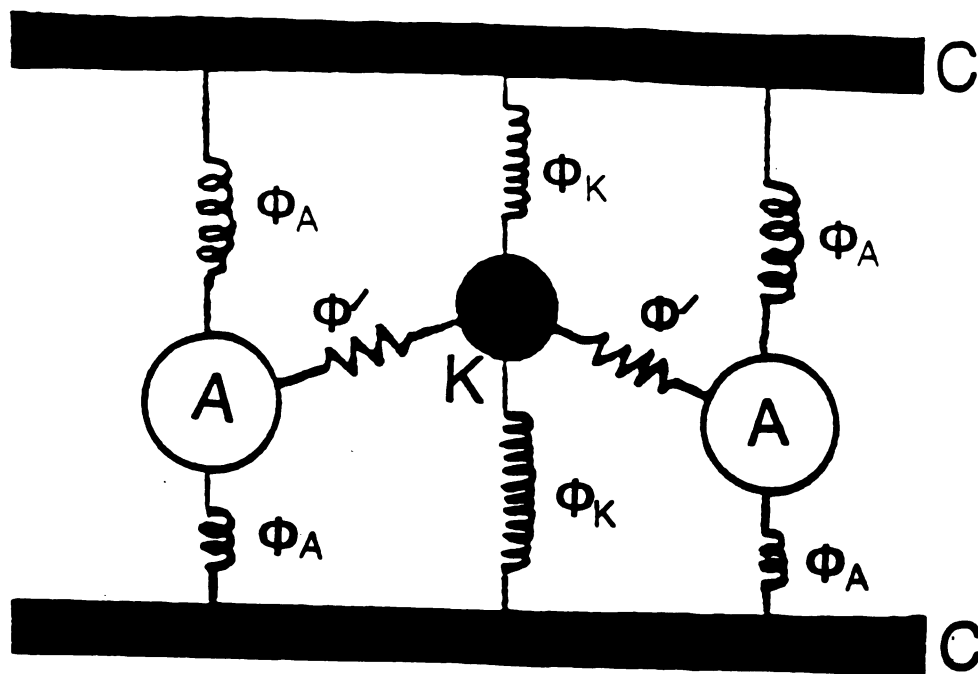


Fig. 3.7 A schematic diagram for the umbrella model described in the text. K represents  $K^+$  ion, A represents ammonia molecule, and C represents a carbon layer.

$$C = \begin{vmatrix} \frac{-(2\phi_K + \phi_A)}{M_C} & \frac{\phi_K(1+e^{iqI})}{\sqrt{M_C M_K}} & \frac{\phi_A(1+e^{iqI})}{\sqrt{M_C M_K}} \\ \frac{\phi_K(1+e^{-iqI})}{\sqrt{M_C M_K}} & \frac{-(2\phi_K + \phi')}{M_K} & \frac{\phi'}{\sqrt{M_A M_K}} \\ \frac{\phi_A(1+e^{-iqI})}{\sqrt{M_C M_A}} & \frac{\phi'}{\sqrt{M_A M_K}} & \frac{-(2\phi_A + \phi')}{M_A} \end{vmatrix}$$

Here the carbon-ammonia interaction is represented by  $\phi_A$ , the K-ammonia interaction (out-of-plane) by  $\phi_K$  and the carbon-potassium interaction is by  $\phi$ . Although, there are three fitting parameters in this matrix, it can not fit the split phonon dispersion curves of Figs. 3.2 and 3.3. Even when additional fitting parameters are employed, using the dynamical matrix  $C'$  where

$$C' = \begin{vmatrix} a_1 & \gamma_1(1+e^{iqI}) & \gamma_2(1+e^{iqI}) \\ \gamma_1(1+e^{-iqI}) & a_2 & \gamma_3 \\ \gamma_2(1+e^{-iqI}) & \gamma_3 & a_3 \end{vmatrix}$$

a satisfactory fit cannot be obtained. Thus we conclude that the bonding model of Fig. 3.7 is not applicable to the libration in  $K(\text{ND}_3)_x\text{C}_{24}$ .

Now consider the "washing machine" mode in which the K-ammonia cluster rotates about an axis which passes through the K-ion and is perpendicular to the graphite basal plane. The fact that this excitation would only take place in the basal plane does not eliminate it from consideration since the observed splitting of the [001]L acoustic phonon branch in the stage-2  $\text{RbC}_8$

compound was found to be attributable to a coupling between the in-plane motion of the Rb and the out-of-plane phonon. NMR results<sup>34</sup> indicate that the graphite layers provide an out-of-plane potential which prevents the ammonia's  $C_3$  axis from lying out of the basal plane. This result as well as the fact that the graphite carbon layer and the K-ammonia cluster have different symmetry would provide a coupling to the [001]L phonon. The coupling Hamiltonian can be determined easily

$$H = -Y\alpha(x_n - x_{n-1})v + \frac{1}{2}a^2v^2 \quad (3.1)$$

where  $v$  is the third degree of freedom representing the angular displacement of K-ammonia cluster.  $Y$  is the coupling constant. The term containing  $x_n - x_{n-1}$  indicates that the narrower the gallery is the stronger is the hindrance to rotation. The dynamical matrix,  $D$ , for "washing machine" motion can be derived by use of Eq. (3.1). We have

$$D = \begin{vmatrix} \frac{\phi}{M} & \frac{\phi}{\sqrt{Mm}}(1+e^{iqI}) & Y\alpha(1-e^{iqI}) \\ \frac{\phi}{\sqrt{Mm}}(1+e^{-iqI}) & \frac{\phi}{m} & 0 \\ Y\alpha(1-e^{-iqI}) & 0 & a^2 \end{vmatrix}$$

Here all symbols have the same physical meaning as in the dynamical matrix  $A$ . Notice that matrices  $A$  and  $D$  are almost identical except for the coupling term, which now contains  $e^{iqI}$  instead of  $e^{i2qI}$ . The former derives from the term  $x_n - x_{n-1}$  in Eq. (3.1) and is apparently more physically meaningful. The positive square roots of the eigenvalues of this matrix are shown as the solid curves in Figs. 3.8 and 3.9. As can be seen, the fit is as good as the one obtained from matrix  $A$  (see Figs. 3.2 and 3.3, all fits have approximately same chi square). The best fit parameters corresponding to these dispersion relations are given in Table 3.4. Comparing Table 3.4 with Tables 3.2 and 3.3, we see that the force constant and the libration energy

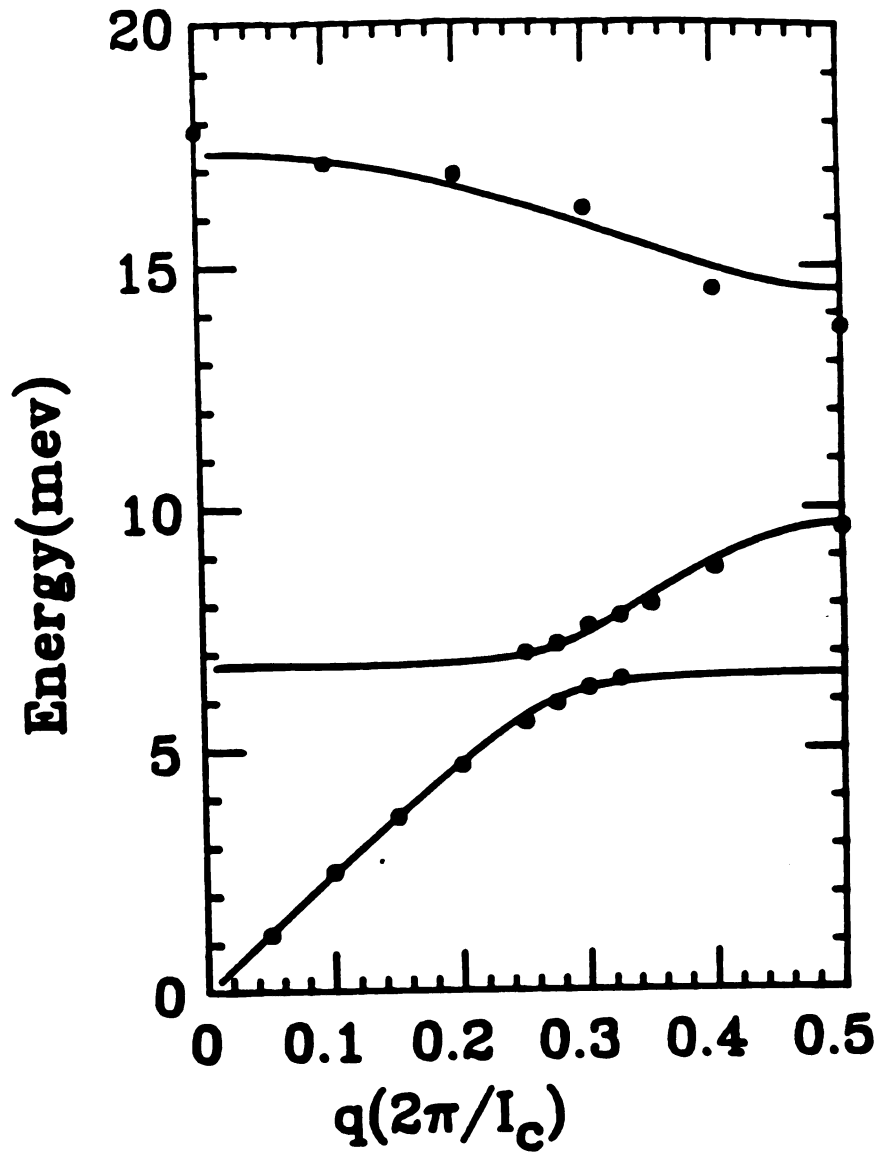


Fig. 3.8 [001]L phonon dispersion curve of stage 1  $K(ND_3)_{4.3}C_{24}$  fitted by dynamical matrix D (see text) for "washing machine" mode.

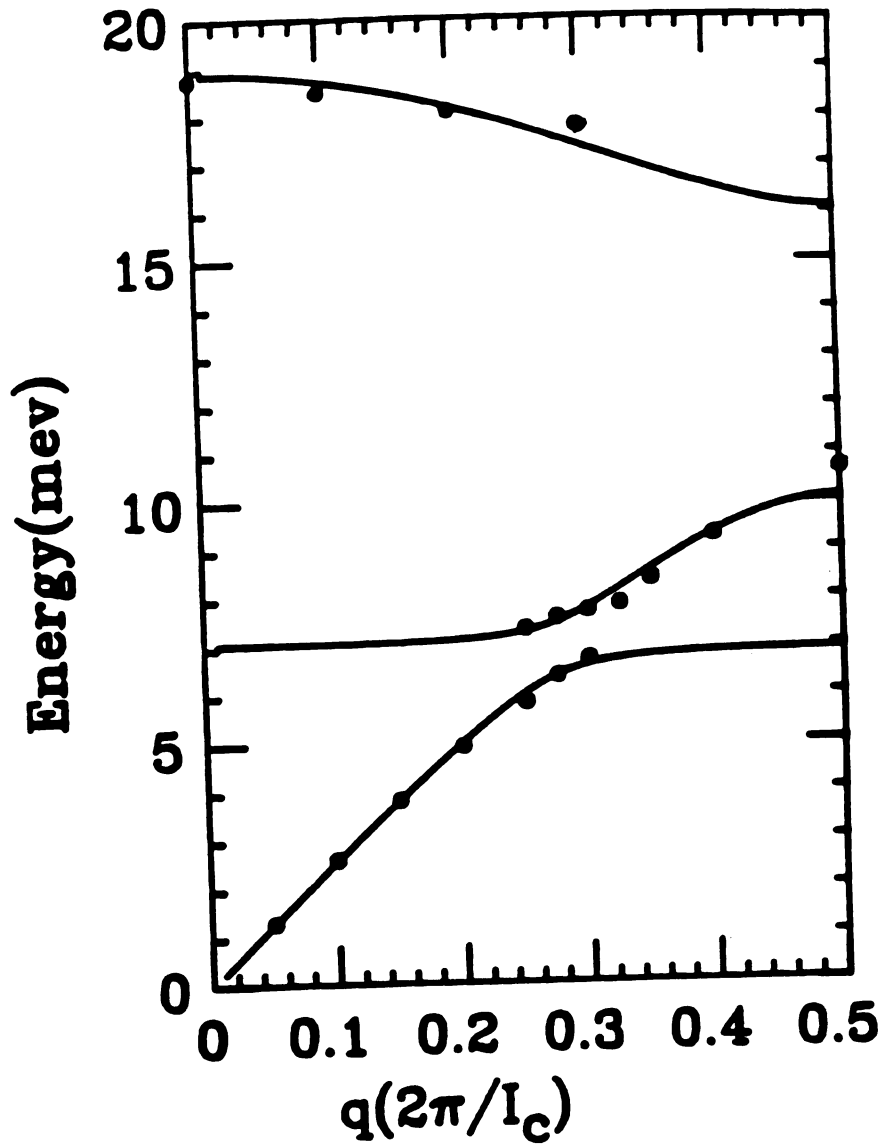


Fig. 3.9 [001]L phonon dispersion curve of stage 1  $K(ND_3)_{3.1}C_{24}$  fitted by dynamical matrix D for "washing machine" mode.

Table 3.4 Best fit parameters for the [001]L modes of two stage 1 K-ammonia intercalated graphite compounds by use of dynamic matrix D.

Compounds	$\phi$ (dyn/cm)	$\lambda$ (mev)	$\gamma$ (mev)
$\text{K}(\text{ND}_3)_{4.3}\text{C}_{24}$	2110	6.7	0.78
$\text{K}(\text{ND}_3)_{3.1}\text{C}_{24}$	2280	7.1	0.78

for all these matrices are the same to within experimental error. The force constant and the sound velocity are determined by the slope of the lowest energy branch and are the same as those determined from dynamical matrix A. Discussion of these parameters has already been presented. We will now consider the mechanism of the libron-phonon coupling.

Notice that the libration energy scales approximately with  $1/\sqrt{m}$  (Fig. 3.10), where  $m$  is the areal intercalate mass density per carbon atom, and that the energy is independent of dynamical matrix used to describe the libron-phonon coupling. This is evidence that the libration excitation is due to the K-ammonia complex. The coupling strength can be represented by  $\gamma_a$  which also scales with  $1/\sqrt{m}$ . Nevertheless, it is consistent with the fact that the c-axis lattice parameter increases as the ammonia concentration increases, reducing the coupling interaction. It is worthwhile to point out that the fit depends crucially on the coupling term whether it contains  $(1-\exp(iqI))$  or  $(1+\exp(iqI))$ . The former come from the out-of-plane to in-plane coupling (without displacement of the center of mass along the c-axis) and the latter represents a coupling between two out-of-plane excitations. A reasonable fit can be only achieved for the former case which strongly suggests that the splitting is due to transverse mode coupling to the longitudinal phonon. This conclusion is also consistent with the fact that the librational mode can barely be observed in the [001] direction without coupling.

We conclude that the actual physical motion of the observed librational excitation is best characterized as a "washing machine" mode: The K-ammonia clusters tend to partially reorient themselves about an axis through the  $K^+$  ion and parallel to the graphite c-axis in response to a force which is provided by the reorientational activation energy. The clusters can not

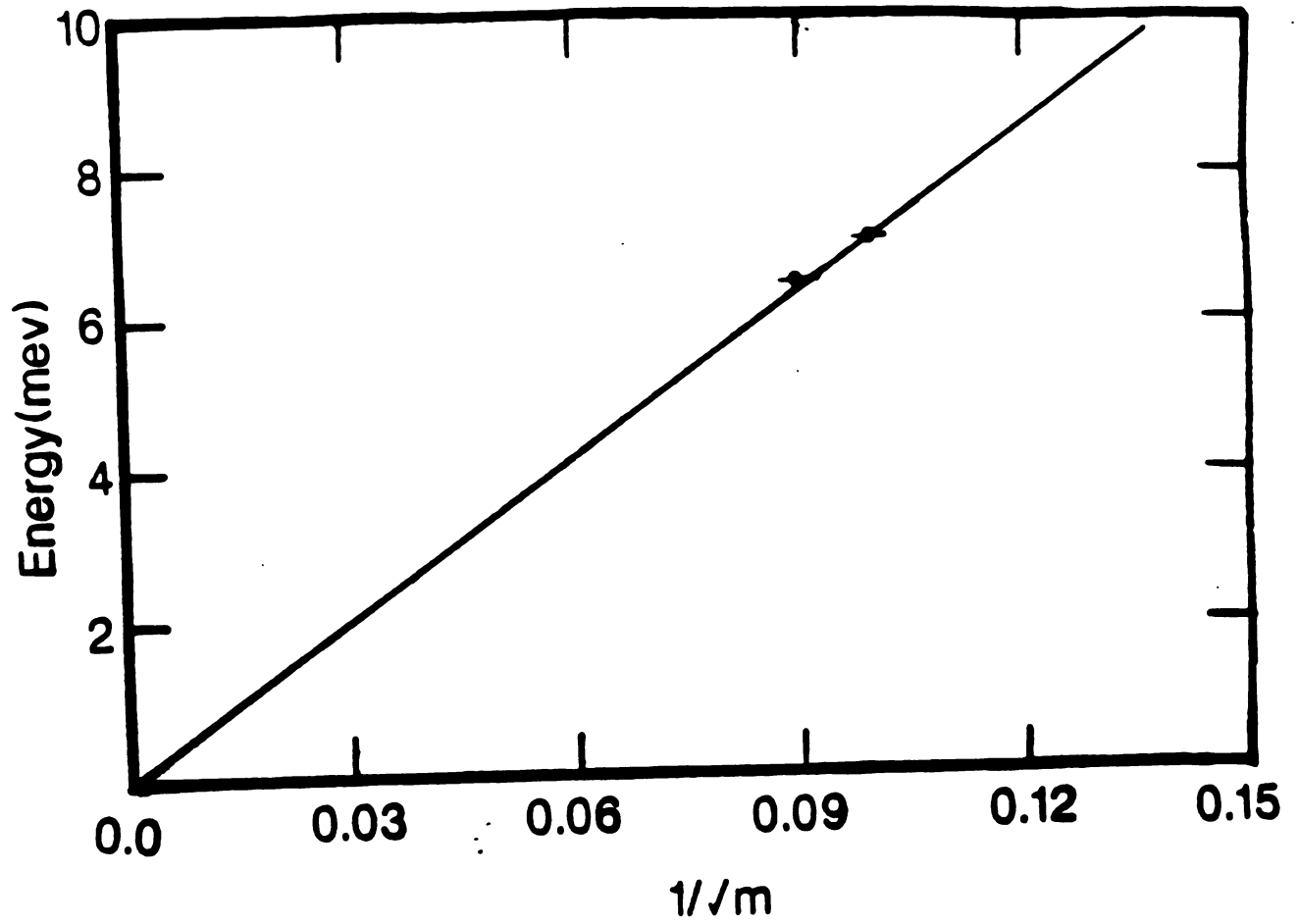


Fig. 3.10 The relation between librational energy  $\alpha$  and the areal intercalate mass.



rotate freely since sterically (see Fig. 3.1) other clusters block rotation. The cluster thus bumps back and forth and this motion constitutes the librational excitation. The relaxation of these excitations forms the reorientational motion of the complex. Quasielastic neutron scattering results (see next chapter) show that the characteristic time of reorientation is of the same order as the libron lifetime. This is evidence that the reorientation happens on a much slower time scale than the libron does and is thus a mechanism for libron damping.

Let us consider a simple model of a K-ammonia complex rotationally oscillating in the potential of the reorientational activation energy. For a classical oscillator,  $2T = U$ <sup>35</sup> and the oscillation frequency is

$$\omega = \left(\frac{U}{I}\right)^{1/2}$$

where  $I$  is the moment of inertia of K-ammonia complex about the rotational axis. Using a metal-ammonia distance of roughly 3 Å and an average complex  $K(\text{ND}_3)_{4.3}$ , we obtain  $I \approx 7.54 \times 10^{14} \text{ meV-Å}^2/\text{c}^2$ . With  $U = 80 \text{ meV}$ <sup>34</sup> (see next chapter), this will give an energy for the libration of about 6.4 meV which is in good agreement with the observed value of 6.7 meV for  $x = 4.3$ . Similarly, for  $K(\text{ND}_3)_{3.1}$  we have  $\omega = 7.5 \text{ meV}$  which is also in good agreement with the observed value of 7.1 meV. The quantitative values for this oversimplified model are not very meaningful. The important thing is that such a simple model gives the right order of magnitude for the librational excitation energy. This simple calculation suggests that the model for libration is reasonable.

It is worthwhile to point out that other mechanisms can also fit the phonon dispersion data since the description is still phenomenological. For instance, in the bond-bending model, if we introduce two transverse degrees of motion for ammonia and K-ion, the dynamical matrix  $C$  will become  $5 \times 5$ , and

the transverse longitudinal coupling term will contain  $(1 - \exp(iqI))$ . Apparently, it will fit the dispersion data with two more extra transverse branches of phonon. However, the energy for this model would be at higher frequency since the stretching force between K and ammonia is strong. In addition, one would expect that the energy will be independent of ammonia concentration. The more realistic mechanism is the stretching mode between K-ammonia complex. The Hamiltonian for this model will be same as Eq. (3.1). The energy of excitation will scale with  $1/\sqrt{m}$  and the coupling constant will be independent of ammonia concentration. All these predictions agree with experimental observation and make the model very promising. However, if we use a barrier of 80 meV, calculation shows that the mean square displacement for this model will be about 2.3 Å, which is an unacceptably large value. The barrier is about two orders of magnitude higher. If the barrier was 100 times lower, the thermal energy would be much higher than the barrier and one would expect that the lifetime of the libron would be so short as to render the definition of libron meaningless. In other words, the stretching mode in the present barrier has a much higher energy than 7 meV.

### 3.4 CONCLUSIONS

We have examined the [001]L phonon dispersion in three K-ammonia TGICs and have shown that the previously proposed bond-bending mode model of the libron motion is deficient. The libron-phonon coupling has to be associated with a transverse mode. The coupling mechanism which is most consistent with all experimental data acquired to date, is the "washing machine" mode of the K-ammonia complex coupled to the [001]L acoustic phonon.

References

1. J.A. Janik, Phys. Rep. 66, 1 (1980).
2. J.J. Rush and J.M. Rowe, Physica 137B, 169 (1986).
3. W. Press; Single Particle Rotations in Molecular Crystals, Springer Tracts in Modern Physics Vol. 92, (Springer-Verlag, Berlin, 1981).
4. P. Thorel, J.P. Coulomb and M. Bienfait, Surface Sci. 114, L43 (1982).
5. R.K. Thomas, Prog. Sol. State Chem. 14, 1 (1982).
6. B.H. Grier, L. Passell, J. Eckert, H. Patterson, D. Richter and R.J. Rollefson, Phys. Rev. Lett. 53, 814 (1984).
7. R. Wang, H. Yaub, H.J. Lauter, J.P. Biberian and J. Suzanne, J. Chem. Phys. 82, 3465 (1985).
8. C. Riekkel, A. Heidmann, B.E. Fender and G.C. Sterling, J. Chem. Phys. 71, 530 (1979).
9. P.C. Eklund, E.T. Arakawa, J.L. Zarestky, W.A. Kamitakahara and G.D. Mahan, Synth. Met. 12, 97 (1985).
10. F. Batallan, I. Rosenman, A. Magerl and H. Fuzellier, Phys. Rev. B32, 4810 (1985).
11. J.P. Beaufils, T.L. Crowley, T. Rayment, R.K. Thomas and J.W. White, Mol. Phys. 44, 1257 (1981).
12. S. Olejnik and J.W. White, Nat. Phys. Sci. 236, 15 (1972).
13. J.M. Adams, C. Breen and C. Riekkel, Clays and Clay Minerals, 27, 140 (1979).
14. D.K. Ross and P.L. Hall, Neutron Scattering methods of investigation clay systems, in Advanced Chemical Methods for Soil and Clay Minerals Research, p93 (1980).
15. D. Walton, H.A. Mook and R.M. Nicklow, Phys. Rev. Lett. 33, 412 (1974).

16. J.M. Rowe, J.J. Rush, S.M. Shapiro, D.G. Hinks and S. Susman, Phys. Rev. B21, 4863 (1983).
17. A. Funahashi, T. Kondow and M. Iizumi, Sol. State Comm. 44, 1515 (1982).
18. D.A. Neumann, H. Zabel, Y.B. Fan, S.A. Solin and J.J. Rush, Phys. Rev. B37, 8424 (1988).
19. W. Rudorff and E. Schultze, Agnew. Chem. 66, 305 (1954).
20. X.W. Qian, D.R. Stumpp, B.R. York and S.A. Solin, Phys. Rev. Lett. 54, 1271 (1985).
21. X.W. Qian, D.R. Stumpp and S.A. Solin, Phys. Rev. B33, 5756 (1986).
22. Y.B. Fan, S.A. Solin, D.A. Neumann, H. Zabel and J.J. Rush, Phys. Rev. B36, .
23. T. Tsang, R.M. Franko, H.A. Resing, X.W. Qian and S.A. Solin, Sol. State Comm. 62, 117 (1987).
24. T. Tsang, R.M. Franko, H.A. Resing, X.W. Qian and S.A. Solin, Sol. State Comm. 63, 361 (1987).
25. R.M. Franko, T. Tsang, H.A. Resing, X.W. Qian and S.A. Solin, Phys Rev. B, to be published.
26. D.A. Neumann, H. Zabel, Y.B. Fan, S.A. Solin and J.J. Rush, J. Phys. C, 20, L761 (1987)
27. Y.Y. Huang, Y.B. Fan, S.A. Solin, J.M. Zhang, P.C. Eklund, J. Hermans, and G.G. Tibbetts, Solid State Comm. 64, 443 (1987).
28. J.M. Zhang, P.C. Eklund, Y.B. Fan, and S.A. Solin, Phys. Rev. B37, 6226 (1987).
29. J.C. Thompson, Electrons in Liquid Ammonia, (Clarendon, Oxford, 1976).
29. B.R. York and S.A. Solin, Phys. Rev. B25, 2463 (1982).

31. Y.B. Fan, and S.A. Solin, 17th Biennial Conference on Carbon, Extended Abstracts and Program, 190 (1985).
32. C. Kittel, Introduction to Solid State Physics, 5th ed. John Wiley & Sons, Inc. (1976).
33. H. Zabel and A. Magerl, Phys. Rev. B25, 2463 (1982).
34. T. Tsang, R.M. Franko, H.A. Resing, X.W. Qian and S.A. Solin, Solid State Comm. 62, 117 (1987).
35. L. Landau, E.M. Lifshitz, Mechanics, Oxford, New York, Pergamon Press, (1969).

## Chapter IV.

**Quasielastic Neutron Scattering Study of Rotations and Diffusion  
in Stage-1 K-Ammonia Intercalated Graphite**

## 4.1 Introduction

In Chapter I, we showed that many properties associated with the motion of individual atoms can be determined by incoherent neutron scattering. Dynamic properties, such as rotations and diffusion in molecular crystals are typical subjects for this type of study. Usually, a large incoherent neutron scattering cross-section is required. This makes the K-ammonia system, which contains hydrogen, an ideal candidate for the study of rotational and translational diffusive motions of molecules confined to a plane<sup>1-3</sup>.

The so called quasielastic neutron scattering (QENS) technique has greatly enhanced our knowledge of the microscopic details of rotations and diffusion in molecular crystals<sup>4-7</sup>. The actual quantity measured by QENS is given in Eq. (1.28). The incoherent scattering function  $S_{inc}(\vec{Q}, \omega)$  is the space and time Fourier transform of the self-correlation function  $G_s(\vec{r}, t)$ , now we return to Eq. (1.24)

$$S_{inc}(\vec{Q}, \omega) = \frac{1}{2\pi\hbar} \int I_s(\vec{Q}, t) e^{-i\omega t} dt \quad (4.1)$$

where the intermediate scattering function  $I_s(\vec{Q}, t)$  is the space Fourier transform of  $G_s(\vec{r}, t)$  and can also be expressed by Eq. (1.25). In order to understand the microscopic details of rotations and diffusion, we will derive the incoherent scattering function for three simple models.

4.2 Translational Diffusive Motion<sup>8</sup>

The diffusion motion is simply governed by Fick's law

$$\frac{\partial P(\vec{r}, t)}{\partial t} = D \nabla^2 P(\vec{r}, t) \quad (4.2)$$

where  $P(\vec{r}, t)$  is the particle density at position  $\vec{r}$  at time  $t$  and  $D$  is the diffusion constant. A solution of this equation is given by the self correlation function

$$G_s(\vec{r}, t) = \frac{1}{(4\pi a(t))^{3/2}} \exp(-r^2/4a(t)), \quad (4.3)$$

where  $a(t, \tau) = D(t-\tau)$ . For true diffusive motion,  $t \gg \tau$ . We can then neglect  $\tau$  and do a space Fourier transform of Eq. (4.3) yielding the intermediate scattering function

$$I_s(\vec{Q}, t) = e^{-Q^2 D t} \quad (4.4)$$

which in turn yields a Lorentzian scattering function

$$S_{inc}(Q, \omega) = \frac{1}{\pi h} \frac{D Q^2}{(D Q^2)^2 + \omega^2}. \quad (4.5)$$

Thus, a diffusive motion of particles is characterized by a Lorentzian line shape with an energy width

$$\Gamma = 2hDQ^2 \quad (4.6)$$

and zero energy scattering function

$$S_{inc}(\vec{Q}, 0) = 1/\pi h D Q^2. \quad (4.7)$$

These results have been experimentally verified for liquid argon at 85K by Skold, et al.<sup>9</sup>

#### 4.3 Translational Jump Diffusion<sup>10</sup>

This is a hopping type motion of atoms on lattice sites in a crystal. For the simplicity of mathematical treatment we assume that the jump motion is random, the jumps are instantaneous, i.e., the residence time is much longer than the flight time to the next lattice site, and the available lattice sites form a Bravais lattice. Then the particle motion can be derived from the rate equation

$$\frac{\partial P(\vec{r}, t)}{\partial t} = \frac{1}{n\pi} \sum_{i=1}^n [P(\vec{r} + \vec{r}_i, t) - P(\vec{r}, t)], \quad (4.8)$$

where  $P(r,t)$  has the same meaning as in Eq. 4.2,  $\tau$  is the residence time and the sum is taken over all  $n$  next nearest neighbor sites at distance  $\vec{\ell}_i$ . Using the boundary condition  $P(\vec{r},0) = \delta(\vec{r})$ , the probability  $P(\vec{r},t)$  becomes equivalent to  $G_s(\vec{r},t)$ . Using the Fourier transform method to solve Eq. (4.8), we obtain

$$I_s(\vec{Q},t) = \exp\left(-\frac{f(\vec{Q})t}{\tau}\right), \quad (4.9)$$

with

$$f(\vec{Q}) = \frac{1}{n} \sum_{i=1}^n (1 - e^{-i\vec{Q} \cdot \vec{\ell}_i}). \quad (4.10)$$

Fourier transformation with respect to time yields a Lorentzian line shaped scattering function

$$S_{inc}(\vec{Q},\omega) = \frac{1}{\pi\hbar} \frac{f(\vec{Q})/\tau}{(f(\vec{Q})/\tau)^2 + \omega^2}, \quad (4.11)$$

with a FWHM

$$\Gamma_{inc} = 2\hbar f(\vec{Q})/\tau, \quad (4.12)$$

and a zero energy scattering function

$$S_{inc}(\vec{Q},0) = \frac{1}{\pi\hbar} \frac{\tau}{f(\vec{Q})}. \quad (4.13)$$

For Bravais lattices, each lattice site is an inversion center and we obtain

$$\begin{aligned} f(\vec{Q}) &= \frac{1}{n} \left[ n - 2 \sum_{i=1}^{n/2} \cos \vec{Q} \cdot \vec{\ell}_i \right] \\ &= \frac{4}{n} \sum_{i=1}^{n/2} \sin^2 \frac{\vec{Q} \cdot \vec{\ell}_i}{2}. \end{aligned} \quad (4.14)$$

Therefore the line width is an oscillatory function with nodes at the reciprocal lattice points  $\vec{Q} = 2\pi\vec{\ell}/\ell^2$  and the zero energy scattering function has singularities at reciprocal lattice points where the line width vanishes (see Fig. 4.1). Notice that at small  $Q$ 's  $\Gamma \propto Q^2/\tau$ , one can compare this with

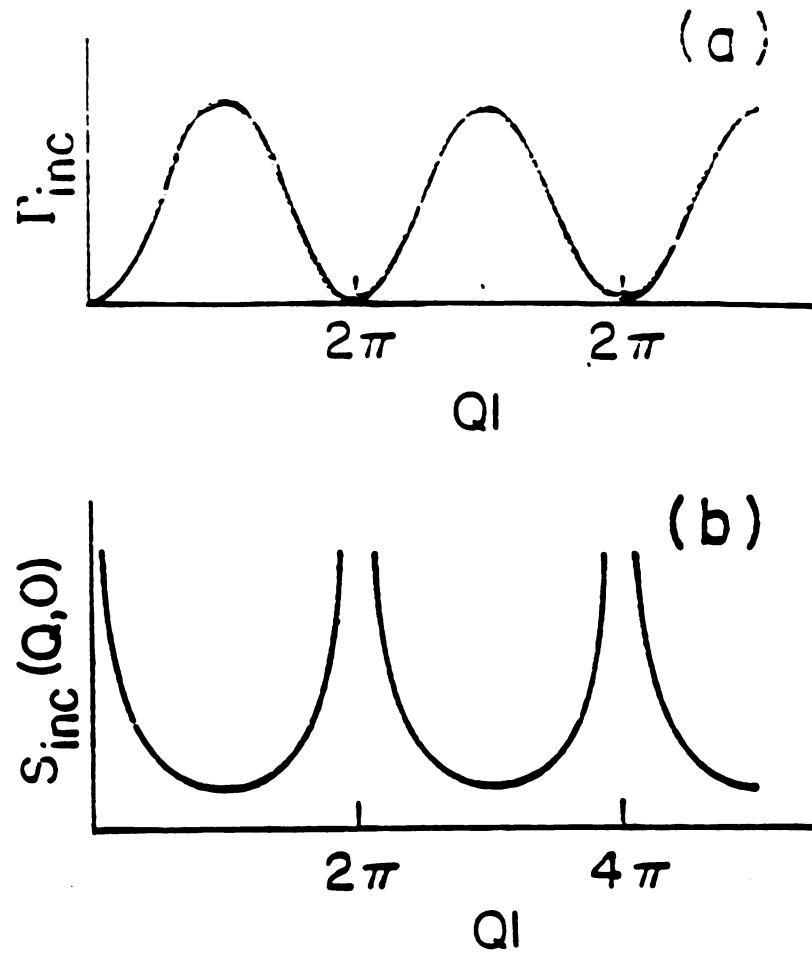


Fig. 4.1 Incoherent scattering from random jump diffusional motion. (a) Full-width at half-maximum  $\Gamma$  plotted against  $Ql$  from relation (4.12). (b) Zero-energy scattering function  $S_{inc}(Q,0)$  from eq. (4.13)

the pure diffusive motion,  $\Gamma = 2hDQ^2$ , obtaining an equivalent diffusion constant for jump diffusion,  $D \propto 1/\tau$ <sup>11</sup>. This makes it possible to compare the QENS results with those obtained using other methods and also to discern the activation energy  $E_0$  via the Arrhenius relation

$$D = D_0 \exp\left(\frac{-E_0}{k_B T}\right) \quad (4.15)$$

#### 4.4 Rotational Jump Diffusion<sup>12</sup>

We now consider the case of a particle motion which is constrained to instantaneous jumps on an available lattice, forming a closed ring. For example, benzene rotates by  $60^\circ$  around its  $c_6$ -axis or ammonia rotates by  $120^\circ$  around its  $c_3$ -axis, and the rotation takes a time much shorter than the residence time (see Fig. 4.2). For illustration, we only derive the scattering function for the three site case (ammonia's jump rotation), as sketched in Fig. 4.2. A general discussion of more complex models can be found in Refs. 12 and 13.

The self-correlation function can be written as

$$G_s(\vec{r}, t) = \sum_{i=1}^n f_i(t) \delta(\vec{r} - \vec{R}_i) \quad (4.16)$$

where  $\vec{R}_i$  are the sites which form a ring and the function  $f_i(t)$  is the probability that a particular atom is at site  $i$  at time  $t$ . Assuming that the jump rate is  $1/\tau$  and the initial condition  $f_1(0) = 1$  which means that the particle 1 is at site 1 at  $t = 0$ , we have the rate equation

$$\frac{df_1(t)}{dt} = \frac{1}{2\tau} \sum_{i=2}^3 [f_i(t) - f_1(t)]. \quad (4.17)$$

and the conditions

$$f_2(t) = f_3(t), \quad \sum_{i=1}^3 f_i(t) = 1$$

The solutions for Eq. (4.17) are

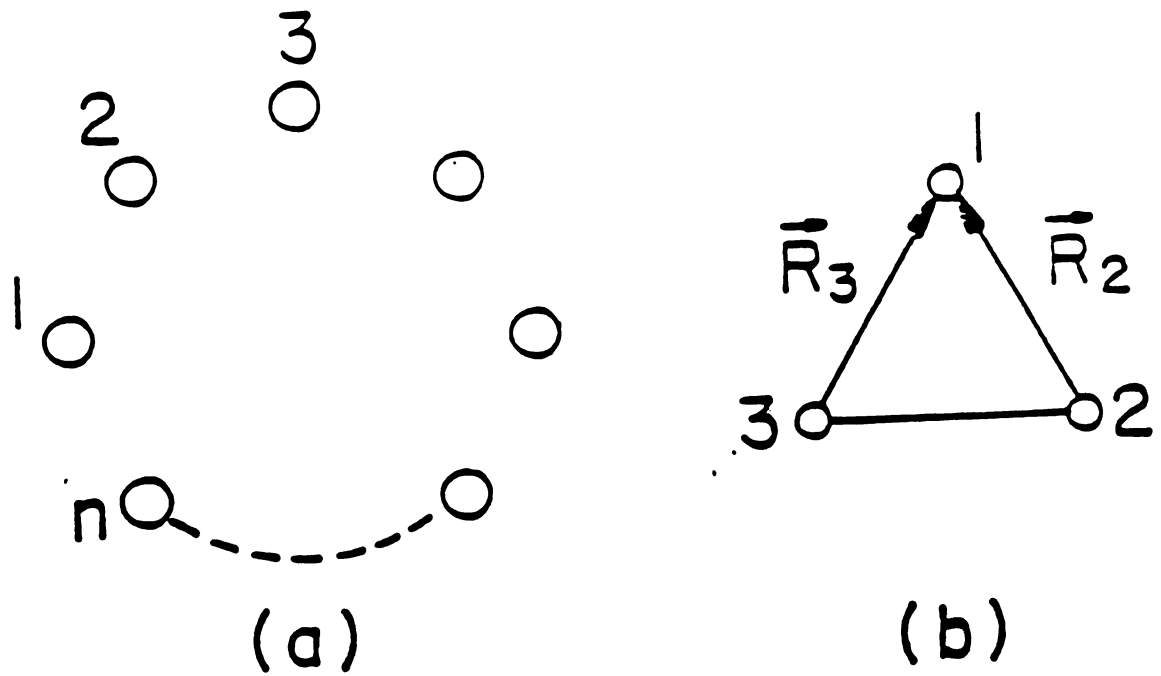


Fig. 4.2 (a) Closed ring of lattice sites for rotational jump diffusion, (b) triangular arrangement of lattice sites for the model discussed in the text.

$$f_1(t) = \frac{1}{3}(1+2\exp(-3t/2\tau))$$

$$f_{2,3}(t) = \frac{1}{3}(1-\exp(-3t/2\tau)). \quad (4.18)$$

For small  $t$ , the probability to find particle 1 at site 1 is greater than that of other particles, and when  $t \rightarrow \infty$ , all  $f_i(t)$  are identical and finite, which give rise a  $\delta(\omega)$  spike in the energy spectrum of  $S_{inc}(\vec{Q}, \omega)$ . From Eqs. (4.16) and (4.18), we can then obtain the intermediate scattering function

$$I_s(Q, t) = \frac{1}{3}(1+2\exp(-3t/2\tau)) + \frac{1}{3}(1-\exp(-3t/2\tau)) \sum_{i=2}^3 \exp(i\vec{Q} \cdot \vec{R}_i). \quad (4.19)$$

Fourier transform of Eq. (4.19) with respect to  $t$ , yields the scattering function

$$S_{inc}(\vec{Q}, \omega) = \frac{1}{2\pi\hbar} \left\{ \left( 2 - \sum_{i=2}^3 \exp(i\vec{Q} \cdot \vec{R}_i) \right) \frac{3/2\tau}{(3/2\tau)^2 + \omega^2} \right. \\ \left. + \frac{1}{3} \left( 1 + \sum_{i=2}^3 \exp(i\vec{Q} \cdot \vec{R}_i) \right) \delta(\omega) \right\}. \quad (4.20)$$

The scattering function consists of two components, a broad Lorentzian with FWHM  $\Gamma \sim 1/\tau$  due to the jump diffusion within the triangle, and a narrow  $\delta$  component caused by the finite value of the correlation function at infinite times.

Using  $|\vec{R}_2| = |\vec{R}_3|$ , and taking the powder average of the scattering function we obtain

$$S_{inc}(\vec{Q}, \omega) = \frac{1}{\pi\hbar} \left\{ [1 - J_0(QR)] \frac{3/2\tau}{(3/2\tau)^2 + \omega^2} \right. \\ \left. + \frac{1}{3} [1 + J_0(QR)] \delta(\omega) \right\} \quad (4.20a)$$

The intensities of the two components are oscillatory functions of the scattering vector, and the sum of two is a constant (see Fig. 4.3).

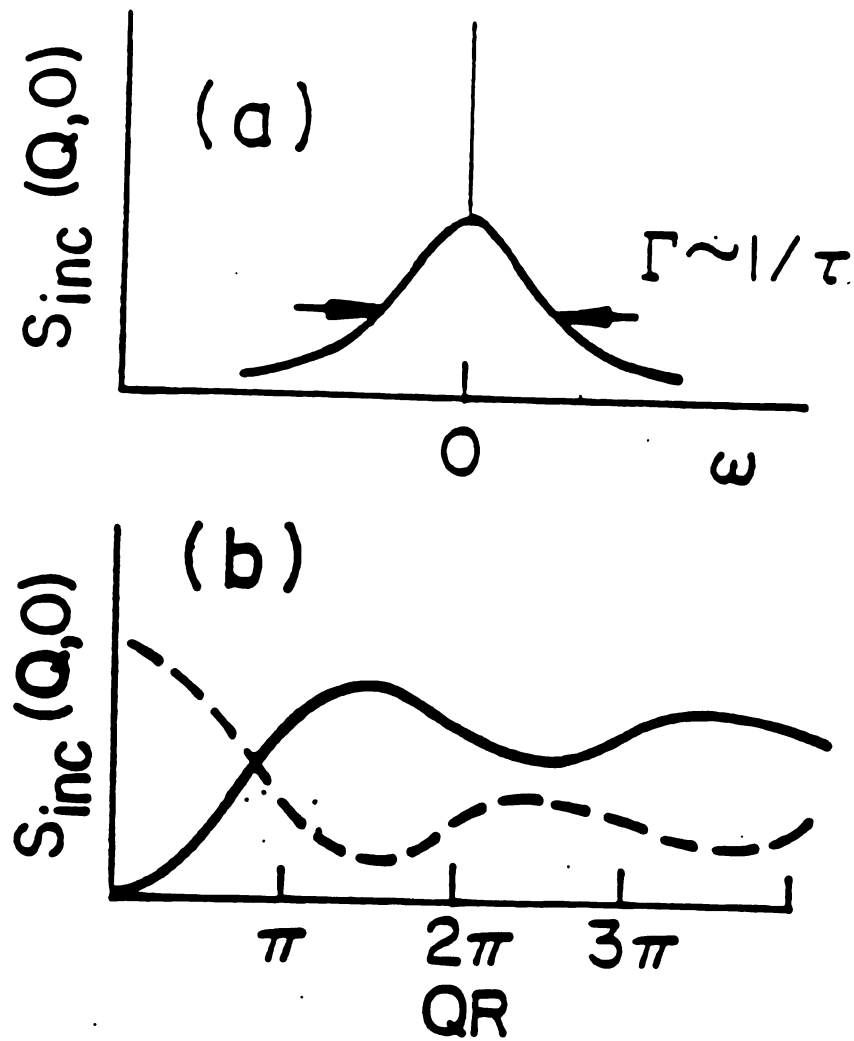


Fig. 4.3 Scattering function for rotational jump diffusion. (a) energy spectrum of broad and narrow component, (b) dependence of  $S_{inc}(Q,0)$  on the scattering vector for the broad component (solid line) and the narrow component (dashed line).

#### 4.5 General case

Apparently, the microscopic diffusion mechanism is not limited to the above three simple examples. For instance, if the thermal energy is of the same order as the static potential barrier separating the wells, the jump diffusion rate  $1/\tau$  becomes a distribution function of time, therefore the jump diffusion can be replaced by rotational diffusion<sup>4</sup>. In this case the scattering function becomes<sup>14</sup>

$$S_{\text{inc}}(\vec{Q}, \omega) = J_0^2(Q\rho\sin\theta)\delta(\omega) + \frac{2}{\pi} \sum_{l=1}^{\infty} J_l^2(Q\rho\sin\theta) \frac{\Gamma_l}{\Gamma_l^2 + \omega^2} \quad (4.21)$$

where  $\rho$  is the radius of the rotating molecule,  $\theta$  is the angle between the axis of rotation and  $\vec{Q}$ , and  $\Gamma_l = l(l+1)D_R$  with  $D_R$  representing the rotational diffusion constant. We see that the main features of the scattering function in Eq. (4.21) are same as those of Eq. (4.20), however, the broad peak now is composed of many different Lorentzians of varying widths, thus making the total width of this component a function of  $\vec{Q}$ .

Besides the molecular motions discussed in previous sections, there are two other types of molecular motions, which have been extensively studied by QENS, i.e. quantum mechanical free rotations and tunneling<sup>6,15</sup>. The quantum mechanical free rotation can only occur when the molecule interacts so weakly with its environment that it can be treated as a free rotator. However, tunneling involves excitations between energy levels which are split due to the overlap of the wavefunction between adjacent potential wells. This provides a new method to measure the local potential. The energy transfer for these two types of motion usually is of the order of  $\mu\text{ev}$ 's. Therefore the measurement requires high resolution spectrometer such as a backscattering spectrometer and has to be carried out at very low temperature.

Usually, a system displays more than one type of diffusive motion. In this case the total scattering function is the convolution of different types of motion<sup>6</sup> in which case the intermediate scattering function can be written as

$$I_s(\vec{Q}, t) = I_s^{\text{vib}}(\vec{Q}, t) \prod_j I_{s_j}(\vec{Q}, t) \quad (4.22)$$

where  $I_s^{\text{vib}}(\vec{Q}, t) = \exp(-Q^2 \langle u^2 \rangle)$  is the Debye-Waller factor and the product is taken over different diffusive motions. The motions can be separated, if they occur on different time scales, because they have different widths. Even if they happen on the same time scale, some information can also be deduced since they have different  $Q$  dependences of the zero-energy scattering functions.

#### 4.6 Experiment

The samples of  $K(\text{NH}_3)_x\text{C}_{24}$  addressed in this chapter were prepared in the same way as those described in Chapter II. The differences are the size of the sample and the fact that hydrogenated ammonia has been used here. For quasielastic neutron scattering, the rule of thumb is that the multiple scattering from the sample has to be less than 10%, so that the sample thickness was estimated to be less than 0.7 mm. We used a  $2 \times 1.5 \times 0.05 \text{ cm}^3$  piece of pyrolytic graphite to form the stage-2 BGIC  $\text{KC}_{24}$  using the 2-bulb technique described in Chapter I. The sample was then placed into an aluminum sample can and ammonia vapor was introduced to form the stage-1 TGIC  $K(\text{NH}_3)_{4.3}\text{C}_{24}$ . The results presented here were again obtained using a triple axis spectrometer (BT-4) located at the National Bureau of Standards Reactor except for a fixed window scan [see Fig. 4.13 and associated discussion] which was obtained on the backscattering spectrometer IN10 at the Institute Laue-Langevin, Grenoble, France. For the triple-axis

spectrometer, pyrolytic graphite ((002) reflection) was used for both the monochromator and the analyzer. The fixed initial energy mode was used with the incident neutron energy at either 4.9 meV (collimation 40'-20'-20'-40') or 3.69 meV (collimation 40'-40'-40'-40') yielding instrumental resolution about 120  $\mu$ eV respectively. A cooled Be filter was placed in the direct beam to remove all harmonic contamination and also to eliminate the fast neutron background. The data were corrected for the varying resolution volume.

For reference, we also measured the elastic neutron scattering patterns of  $\text{K}(\text{ND}_3)_{4.3}\text{C}_{24}$  at 5K (Fig. 4.4) and 200 K (Fig. 4.5). These patterns were obtained using the deuterated sample discussed in Chapters II and III. We already know from Chapter II that the inplane structure of the K-ammonia layer is liquid-like at room temperature. As the temperature is decreased, the inplane structure shows a disorder-order transition as evidenced by Figs. 4.4 and 4.5. The ordered phase cannot be determined unambiguously from these neutron scattering patterns alone. It is possibly a multiple phase structure or a modulated  $3 \times 3$  structure. In this chapter, we will discuss quasielastic results in both the low temperature ordered phase and the high temperature liquid phase. We will further consider this ordered structure below.

#### 4.7 Results and discussions

In Fig. 4.6, the quasielastic scans for several different Q's at room temperature are shown. They were fitted by two component peaks (two Lorentzians) broadened by the Gaussian instrumental resolution. The broader Lorentzians have a width of 1.2 meV which is independent of Q indicating the

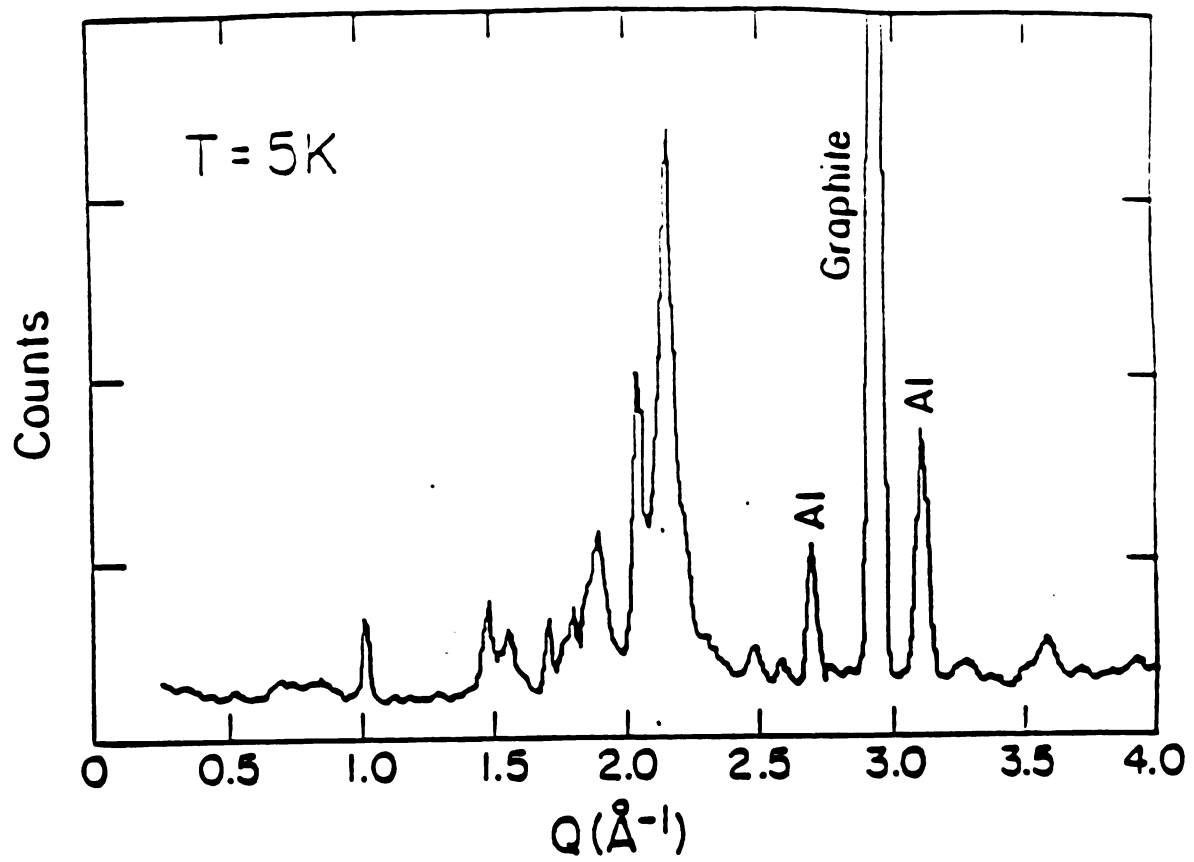


Fig. 4.4 Inplane elastic scans of  $K(ND_3)_{4.1}K_{24}$  at 5K, showing an ordered phase, possibly multiphase structure.

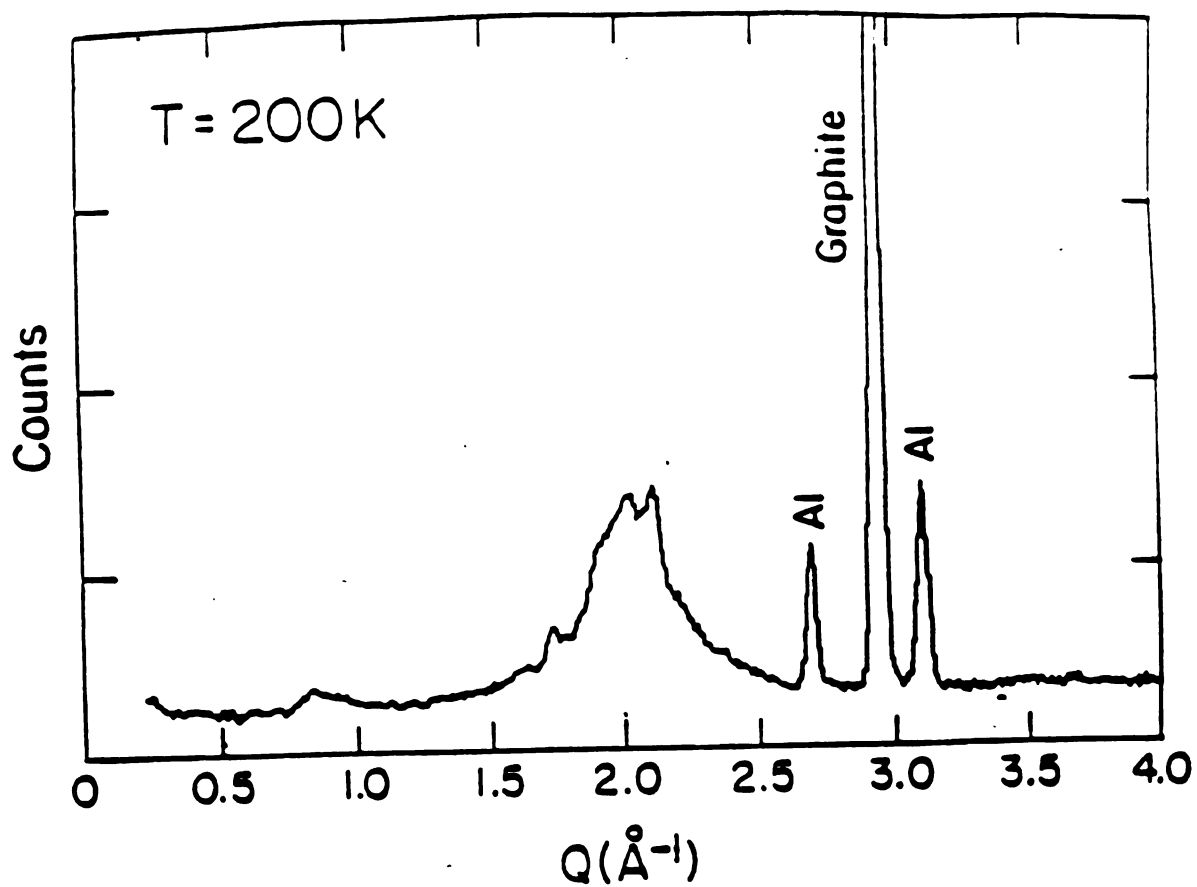


Fig. 4.5 Inplane elastic scans of  $\text{K}(\text{ND}_3)_{4.1}\text{K}_{24}$  at 200K, showing that the intercalant is essentially a liquid at this temperature.

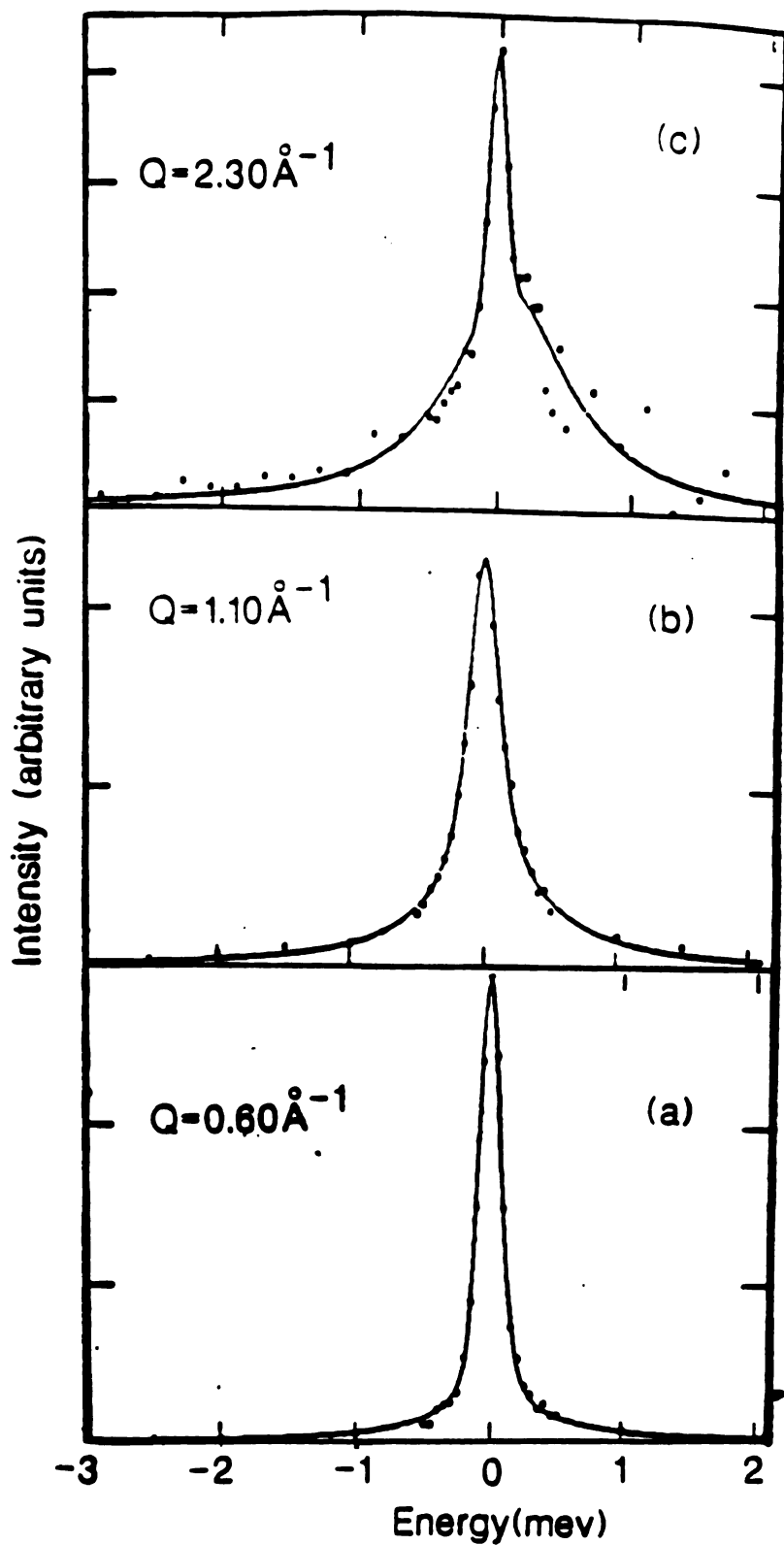


Fig. 4.6 The quasielastic spectra of  $K(\text{NH}_3)_{4.3}\text{C}_{24}$  at 300K for a scattering vector at  $Q=0.6\text{ \AA}^{-1}$  (a),  $Q=1.10\text{ \AA}^{-1}$  (b),  $Q=2.3\text{ \AA}^{-1}$  (c). Each spectrum was fitted by two Lorentzian functions giving the widths plotted in Fig. 4.7.

existence of rotational diffusion of the  $\text{NH}_3$  molecule. The central peaks are broader than the instrumental resolution which is evidence of translational diffusion. The widths vs.  $Q$  for  $T = 300\text{K}$  are given in Fig. 4.7. As expected, the width of the rotational component is independent of the scattering vector, and the width of translational component is apparently proportional to  $Q^2$  for small  $Q$ . From the  $Q$ -dependence, we estimate the translational diffusion constant to be  $1 \times 10^{-6} \text{ cm}^2/\text{sec}$  at  $T=300\text{K}$ .

Quasielastic scans for different temperatures are given in Fig. 4.8. At  $T = 10\text{K}$ , a good fit to the data was achieved by the use of a two component peak (a  $\delta$ -function and a Lorentzian) broadened by instrumental resolution. The width obtained from the fit is still 0.4 meV even at 10K. As the temperature is increased, the width of this component increases. At  $T = 150\text{K}$ , a width of 1.3 meV was obtained from the fit. As the temperature is further increased to  $T = 200\text{K}$ , it is found that the first Lorentzian has broadened into a flat background, but another Lorentzian with a width of 0.2 meV is clearly manifested in the scattering function. At room temperature, this Lorentzian component has a width of 1.2 meV. The only reasonable explanation for this is that the first Lorentzian at lower temperature is due to the rotation of the  $\text{NH}_3$  molecule with lower activation energy and the rotation which persists at room temperature has a higher activation energy. Arrhenius plots indicate that the activation energy for these two rotations are 2 meV and 80 meV respectively (Figs. 4.9 and 4.10).

. Fig. 4.11 shows the zero-energy transfer scattering function for the second rotational component and the translational component of the quasielastic line at room temperature. The fact that both components quickly drop to zero intensity instead of oscillating indicates that the

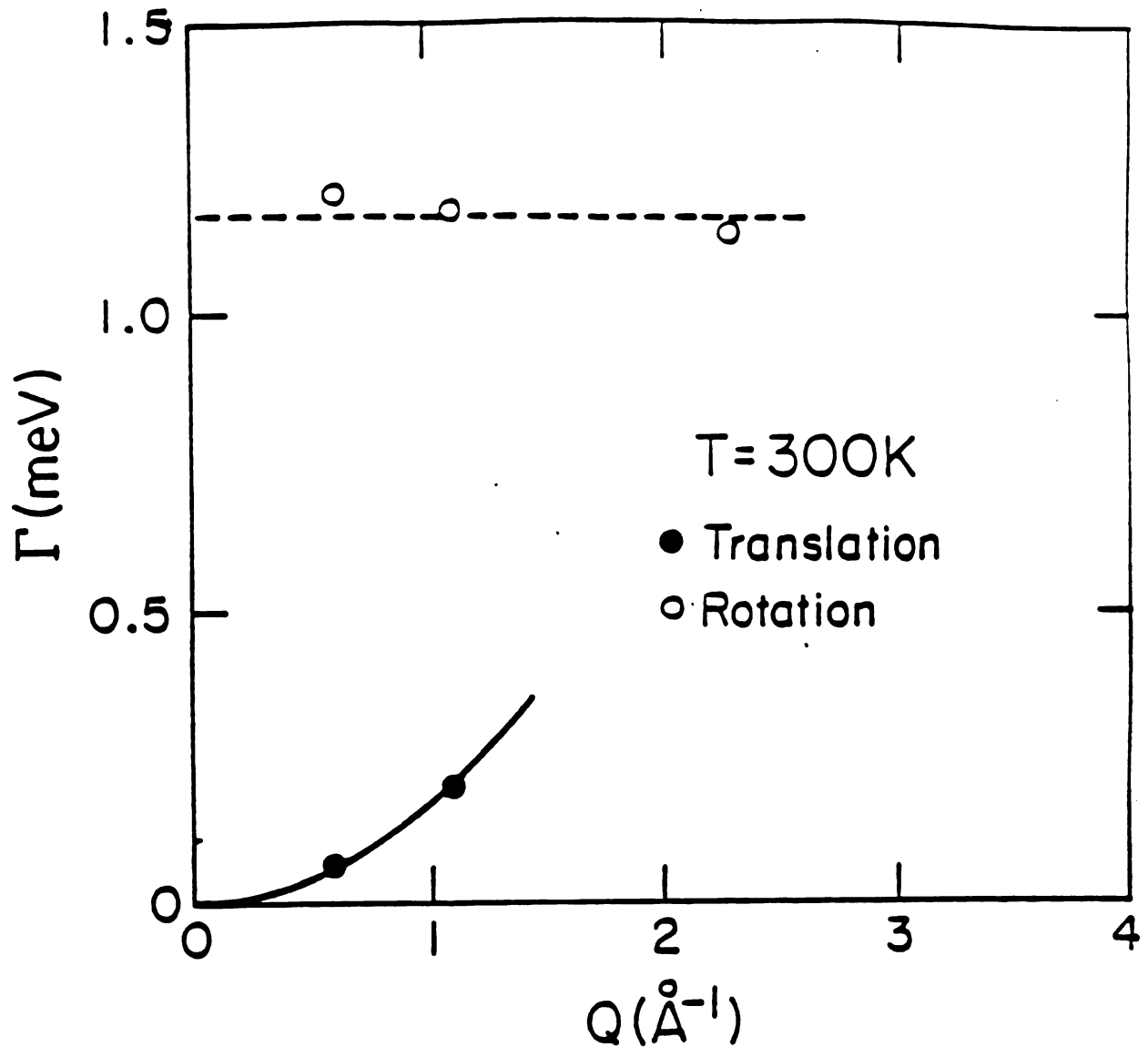


Fig. 4.7 The width (obtained from the fits in Fig. 4.6) of the high temperature rotational and translational components of the scattering plotted as a function of the scattering vector at 300K. From the  $Q$  dependence of the broadening of the translational component, we obtain a diffusion constant of  $1.0 \times 10^6 \text{ cm}^2/\text{sec}$ .

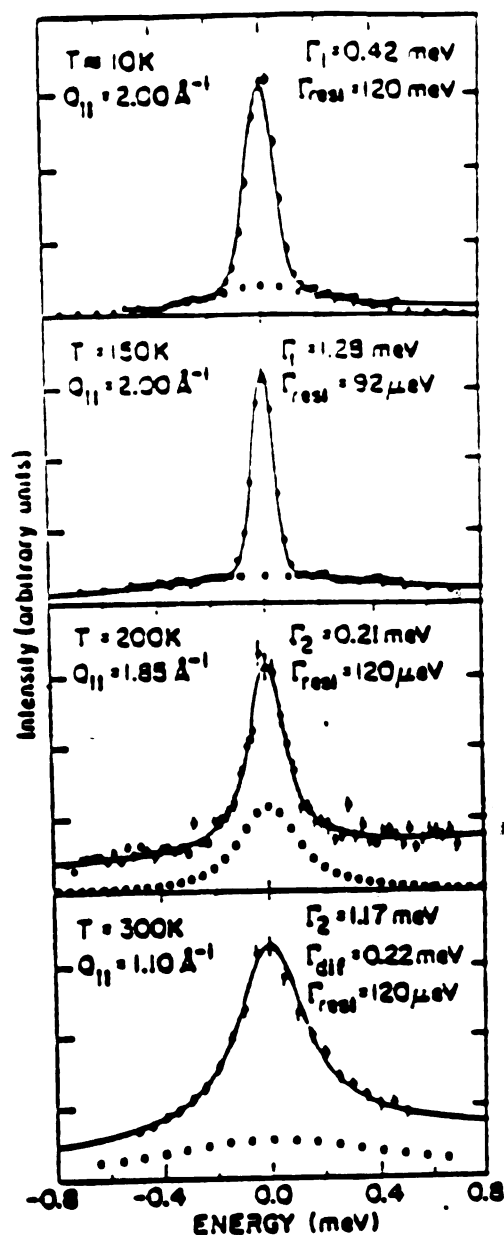


Fig.4.8 (a) A quasielastic spectrum of  $\text{K}(\text{NH}_3)_4 \cdot 3\text{C}_{24}$  at 10 K. The open circles are the experimentally measured points, the full curve is a fit to a  $\delta$ -function plus a Lorentzian, both convoluted with the Gaussian instrumental resolution, and the full squares represent the Lorentzian contribution to the scattering. A scattering function of this type is indicative of a rotational motion of the ammonia molecules. (b) A quasielastic spectrum at 150 K. This shows the broadening of the Lorentzian component of the scattering function. The activation energy of this motion is estimated to be about 5 meV. (c) A quasielastic spectrum at 200 K (above the intercalant melting transition). Here the previously observed Lorentzian has broadened into a flat background. However the peak still includes both  $\delta$ -function and a Lorentzian component due to the appearance of a different reorientational motion. (d) A quasielastic spectrum at room temperature. The elastic component has also been broadened due to translational motion of the ammonia molecules.

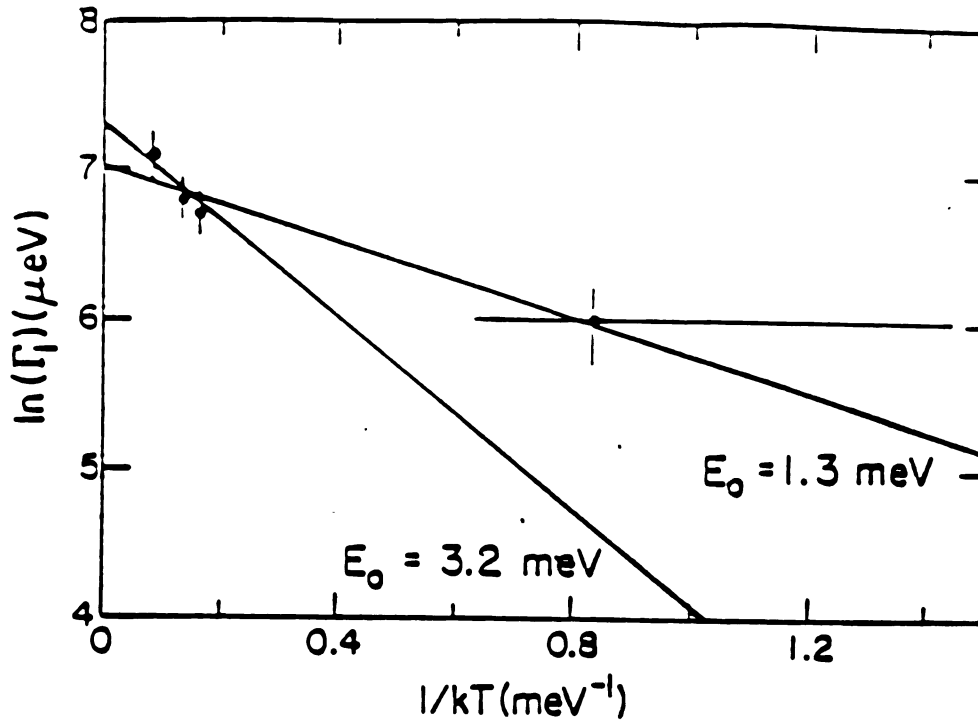


Fig. 4.9 Arrhenius plot which shows the  $\ln$  of the peak width as a function of  $1/kT$  for the low temperature rotation. The solid lines are drawn for activation energies of 1.3 meV (best fit) and 3.2 meV. From this we estimate the activation energy to be 2 meV.

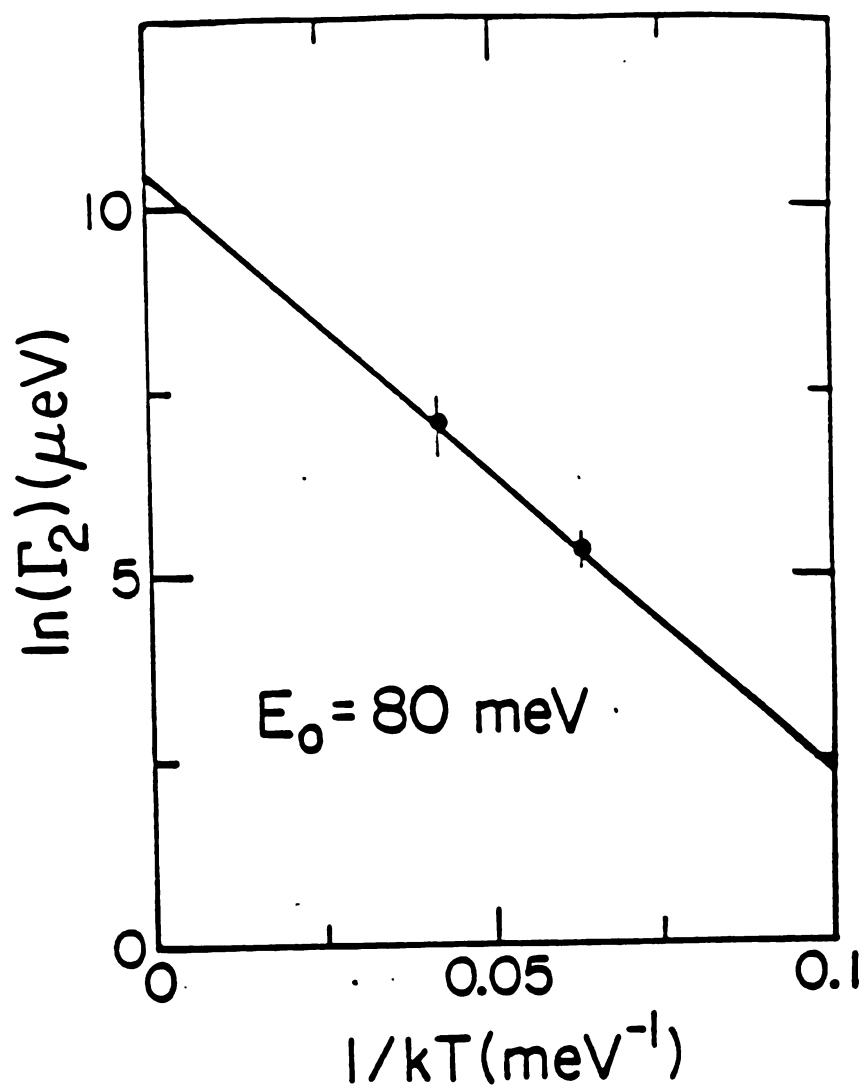


Fig. 4.10 Arrhenius plot for the high temperature rotation. The solid line represents an activation energy of 80 meV.

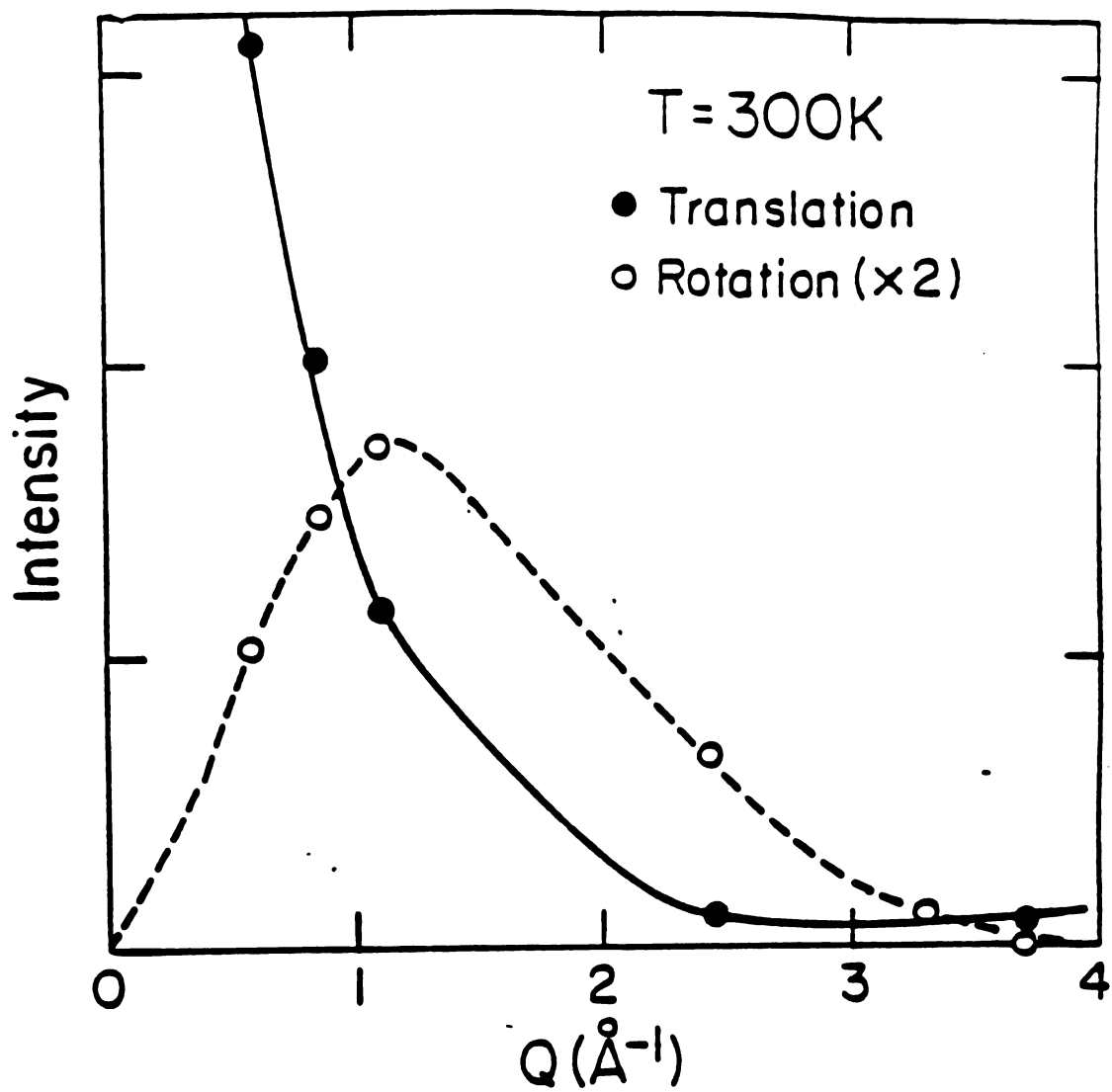


Fig. 4.11 The intensities of the high temperature rotational and the translational compounds of the scattering plotted as a function of  $Q$  for  $T=300\text{K}$ .

motion is highly complex and cannot be easily separated into rotational and translational components at these scattering vectors.

It is clear that the current results, obtained with a triple-axis spectrometer located at a thermal neutron reactor, do not include quasielastic spectra at enough values of the scattering vectors, to allow a comparison of the intensities and widths of the various components of the scattering function to a particular model. Thus it is difficult to determine the jump vectors of the rotational or translational motions, and to assess if jump vectors are a valid concept for any of these motions in any of the temperature ranges studied. Nevertheless, it is possible to give a reasonable assignment to each of the diffusive motions with the aid of other experimental results.

The quasielastic scattering observed at low temperatures is almost certainly due to rotations of the hydrogens about the threefold molecular axis. The rotation observed at high temperatures is assigned to the reorientation of the  $K-NH_3$  complex and the translational motion is either the motion of the complex as a unit, or of the individual ammonia molecule, or both. This assignment is consistent with the fact that the scans performed with  $\vec{Q}$  perpendicular to the carbon planes show that the two motions appearing in the liquid phase take place mostly parallel to the basal plane. This assignment is also in accord with recent NMR results<sup>17</sup> which indicate that at room temperature both spinning of the ammonia molecule about its threefold axis and precession of this axis about the graphite c-axis are present and that both motions occur with frequencies greater than  $10^5$  Hz. When we include the librational motion discussed in Chapter III, the overall motion of ammonia can be described in Fig. 4.12.

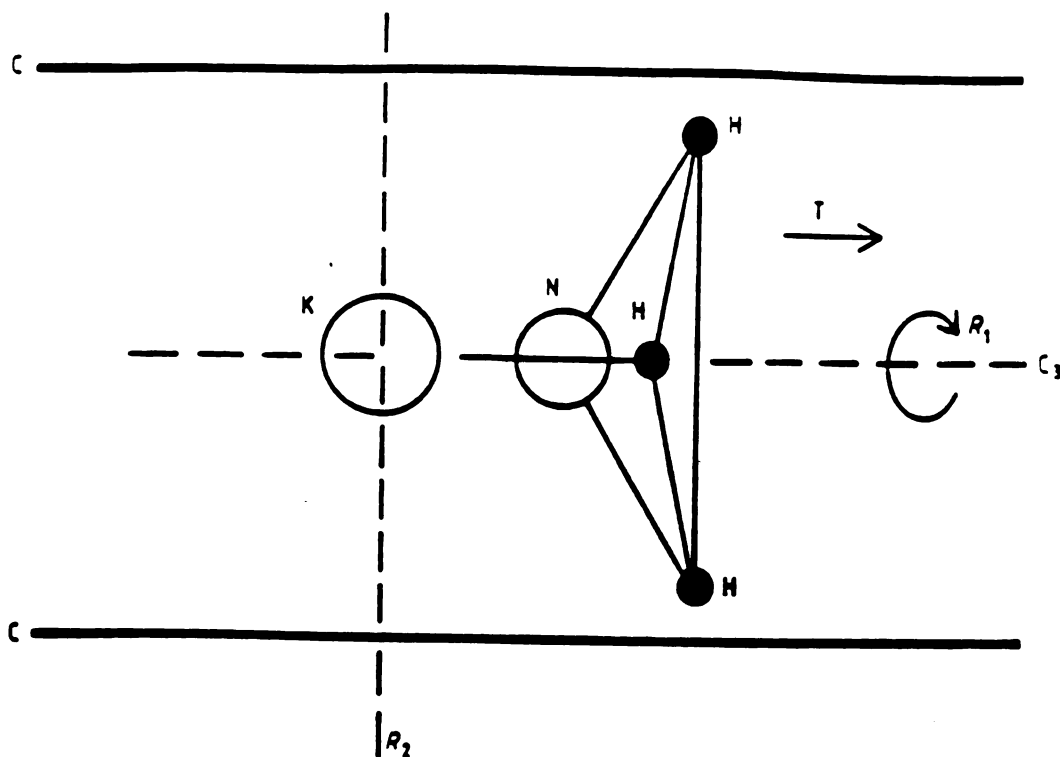


Fig. 4.12 A schematic diagram of the motions in  $\text{K}(\text{NH}_3)_4 \cdot 3\text{C}_{24}$ . The molecule spins about the three-fold molecular axis, reorients about a given K atom, and translates either through the motion of the entire  $\text{K-NH}_3$  cluster or by the ammonia moving between adjacent cluster. Note that only the spinning motion occurs in the low-temperature ordered phase.

Dr  
re  
th  
li  
t  
r  
n  
q  
Q  
t  
e  
e  
t  
e  
o  
o  
a  
t  
s  
t  
i  
w  
i  
t  
t  
a

The ammonia molecule spins about its threefold axis at low temperature; reorients about a given K-ion; and translates either through the motion of the entire complex or by the ammonia moving between adjacent complexes; and librates about the K atom (see Chapter III).

Fig. 4.13 shows a so called "fixed window" scan taken on the backscattering spectrometer IN10 at the Institute Laue-Langevin with an energy resolution of about 0.5  $\mu\text{ev}$ . The energy window for the scan is 15  $\mu\text{ev}$ . Here we display the total intensity of the elastic component of the quasielastic line in this window as a function of the temperature for  $Q = 1.68 \text{ \AA}^{-1}$  directed both in and out of the basal plane. At high temperature above 185K, the inplanar structure is liquid-like so the elastic component is weak, the scattering is mostly inelastic due to the Doppler effect. When the temperature is decreased to 185K, a dramatic increase in the elastic intensity occurs for  $Q$  parallel to the basal plane. This is a clear signal of an inplane liquid-solid transition. Recalling that the order-disorder transition we presented in the previous section occurs at about the same temperature, leads us to conclude that this effect must be due to the same mechanism, i.e., the onset of translational diffusion and possibly also the reorientation of the  $\text{NH}_3$  molecule discussed earlier. As the temperature decreased from 185K to about 30K, the intensity increases linearly, this temperature dependence is consistent with the thermal Debye-Waller factor in the high temperature limit. Below 30K the elastic intensity increases for both  $Q$  in and out of the basal plane, indicating that another low energy motion is frozen. The best candidate for this motion is certainly the rotation of the ammonia about its three-fold symmetry axis since it would display components in both of the directions

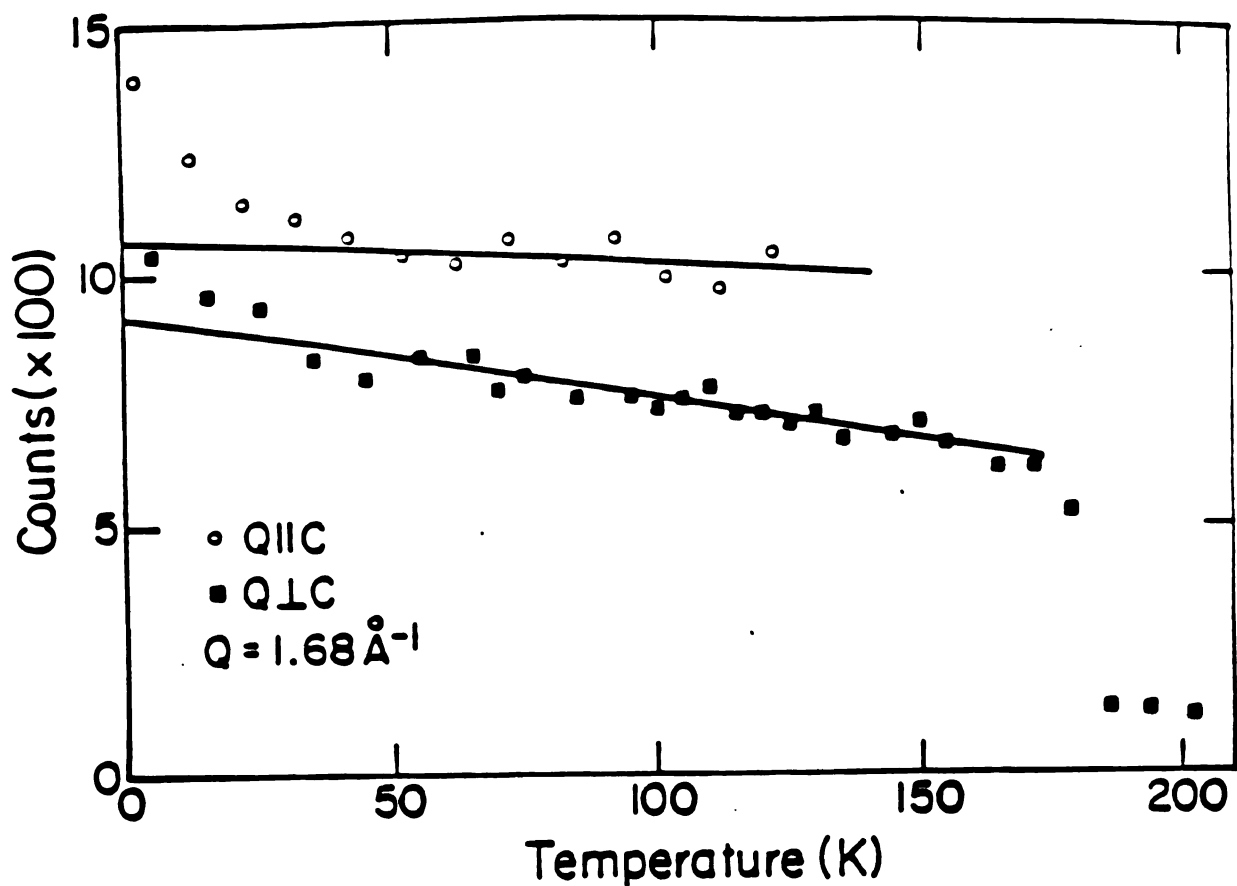


Fig.4.13 The elastic intensity as a function of temperature for two directions of scattering vector  $Q$  both having a magnitude of  $1.68 \text{ \AA}^{-1}$ . This intensity includes all of the counts within the resolution width of  $1/2 \text{ \mu eV}$ . For  $T < 30\text{K}$ , the intensity increases quickly as temperature decreases, possibly indicating the presence of rotational tunneling. For  $30 < T < 180\text{K}$  shows a linear decrease in the intensity with increasing temperature. Then For  $T \approx 185\text{K}$ , there is a sudden drop in the intensity of the elastic component for  $Q$  parallel the graphite basal plane, which is associated with the inplane transition.

and since the temperature for this motion to appear is at 30 K which corresponds to the 2 meV activation energy of this motion determined from Fig. 4.10.

In conclusion, the model of the spinning, reorientation and libration qualitatively explains the quasielastic neutron scattering data. In order to unambiguously determine the dynamics of this system more data are needed for different temperatures and Q's.

References

1. C. Riekel and A. Heidemann, B.E.F. Fender, and G.C. Stirling, *J. Chem. Phys.* 71, 530 (1979).
2. H. Zabel, A. Magerl, A.J. Dianoux, and J.J. Rush, *Phys. Rev. Lett.* 50, 2094 (1983).
3. F. Batallan, I. Rosenman, A. Magerl, H. Fuzellier, *Phys. Rev.* B32, 4810 (1985).
4. W. Press, Single-Partical Rotations in Molecular Crystals, Springer Tracts in Modern Physics vol. 92, (Springer-Verlag, Berlin, 1981).
5. J.W. White, in Dynamics of Solids and Liquids by Neutron Scattering, edited by S.W. Lovesay and T. Springer, Springer Topics in Current Physics vol. 3, (Springer-Verlag, Berlin, 1977), p. 197.
6. T. Springer, in Dynamics of Solids and Liquids by Neutron Scattering, edited by S.W. Lovesay and T. Springer, Springer Topics in Current Physics vol. 3, (Springer-Verlag, Berlin, 1977), p. 255.
7. H. Zabel, in Nontraditional Methods in Diffusion, edited by G.E. Murch, H.K. Birnbaum, and J.R. Cost, (The Metallurgical Society of AIME, Warrendale, PA, 1984), p.1.
8. G.H. Vineyard, *Phys. Rev.*, 110 999 (1958).
9. K. Shold, J.M. Rowe, G. Ostrowski, and P.D. Randolph, *Phys. Rev.* A6 1107 (1972).
10. C.T. Chudley and R.J. Elliott, *Proc. Phys. Soc.* 77, 353 (1960).
11. C.P. Flynn, Points Defects and Diffusion, (Clarendon Press, Oxford, 1972).
12. V.F.Sears, *Can. J. Phys.*, 45 237 (1967).

13. T. Springer, Quasielastic Neutron scattering for the Investigation of Diffusive Motions in Solids and Liquids, Springer Tracts in Modern Physics, vol. 64, Springer, Berlin, Heidelberg, New York, 1972.
14. J.A. Janik, J.M. Janik, K. Otnes, and K. Rosciszewski, Physica B83, 259 (1976).
15. D.A. Neumann, H. Zabel, J.J. Rush, Y.B. Fan, and S.A. Solin, to be published.
16. T. Tsang, R.M. Franko, H.A. Resing, X.W. Qian, and S.A. Solin, Solid State Comm. 62, 117 (1987).

## Chapter V.

Neutron scattering studies of  $(\text{CH}_3)_3\text{NH}^+$ -Vermiculite

## 5.1 INTRODUCTION

Recently, clay intercalation compounds (CIC's) have drawn the attentions not only of chemists but also of solid state physicists due to the novel chemical and physical properties<sup>1-6</sup> of these materials. Layered silicates such as vermiculite as well as its intercalation compounds, which are the focus of this chapter, are unique among lamellar solids in their ability to be pillared<sup>3</sup> by robust intercalated guest ions which occupy specific lattice sites in the interlayer galleries. These materials provide a testing ground for the study of 2D layer rigidity and pillaring, the latter of which is a special example of the more general phenomenon of intercalation. Pillared clays also provide a unique system for the study of 2-dimensional microporosity. The distinguishing feature of pillared clays is that the gallery cations are robust 3D species which function in the water-free interlayer space as molecular props. The pillaring cations can be uniform in size and spacing within the galleries. Therefore, the enormous free volume of accessible interior space that is derived from such an open structure has significant practical applications in the field of catalysis and sieving. In addition, the microporous structure provides a possible system for probing the 2D percolation process because one can accurately control (to one part in  $10^5$ ) the number of open "bonds" in the planar network by controlling the concentration (X) in a mixed ion pillared clay such as  $\text{A}_{1-x}\text{B}_x$ -Vermiculite. This control is especially important near the percolation threshold<sup>7</sup> where fractal<sup>8</sup> behavior dominates the structural arrangement of the intercalated species.

Mixed ion compounds of the type,  $A_{1-x}B_x$ -Vermiculite also provide a system for the study of the dynamics of 2D molecular crystals formed by the intercalant. Such a study can give information about the pillaring mechanism. One expects that the molecular motion can be separated into two parts, the external modes related to displacements of and rotations about the molecular center of mass, and the internal modes of much higher frequency, related to vibrations with respect to the center of mass. Neutron scattering is a powerful tool to elucidate these properties.

Vermiculite is built up from sheets of corner shared  $\text{SiO}_4$  tetrahedra and sheets of edge shared  $\text{AlO}_6$  octahedra to form a 2:1 layer structure such as that shown in Fig. 5.1. Such a clay has a cation exchange capacity which depends upon the substitution of lower valent atoms for aluminium in the octahedral sheet. The 2:1 clay layers are thus negatively charged because of this and charge neutrality is provided by the cations which are present in the galleries. Note that unlike graphite which is amphoteric, the clay layers have a fixed negative charge. The intercalation process in these compounds is equivalent to ion exchange but does not involve charge transfer between the guest and host species. The basal oxygen layers are arranged in a Kagome lattice whose hexagonal pockets form a triangular lattice of gallery sites. In the interlayer galleries of vermiculite as well as other clays chemical reactions can be selective, specific, and quite distinct compared with the corresponding reaction in the free space.

: Recently, attention has been focused<sup>9-11</sup> on the structural and dynamical properties of the ternary CIC  $A_{1-x}B_x$ -vermiculite,  $0 \leq x \leq 1$ , with A = trimethylammonium =  $(\text{CH}_3)_3\text{NH}^+$  and B = tetramethylammonium =  $(\text{CH}_3)_4\text{N}^+$ . The guests in this system are sufficiently robust to be considered as pillars but structurally tractable enough to elucidate the physics of the pillaring

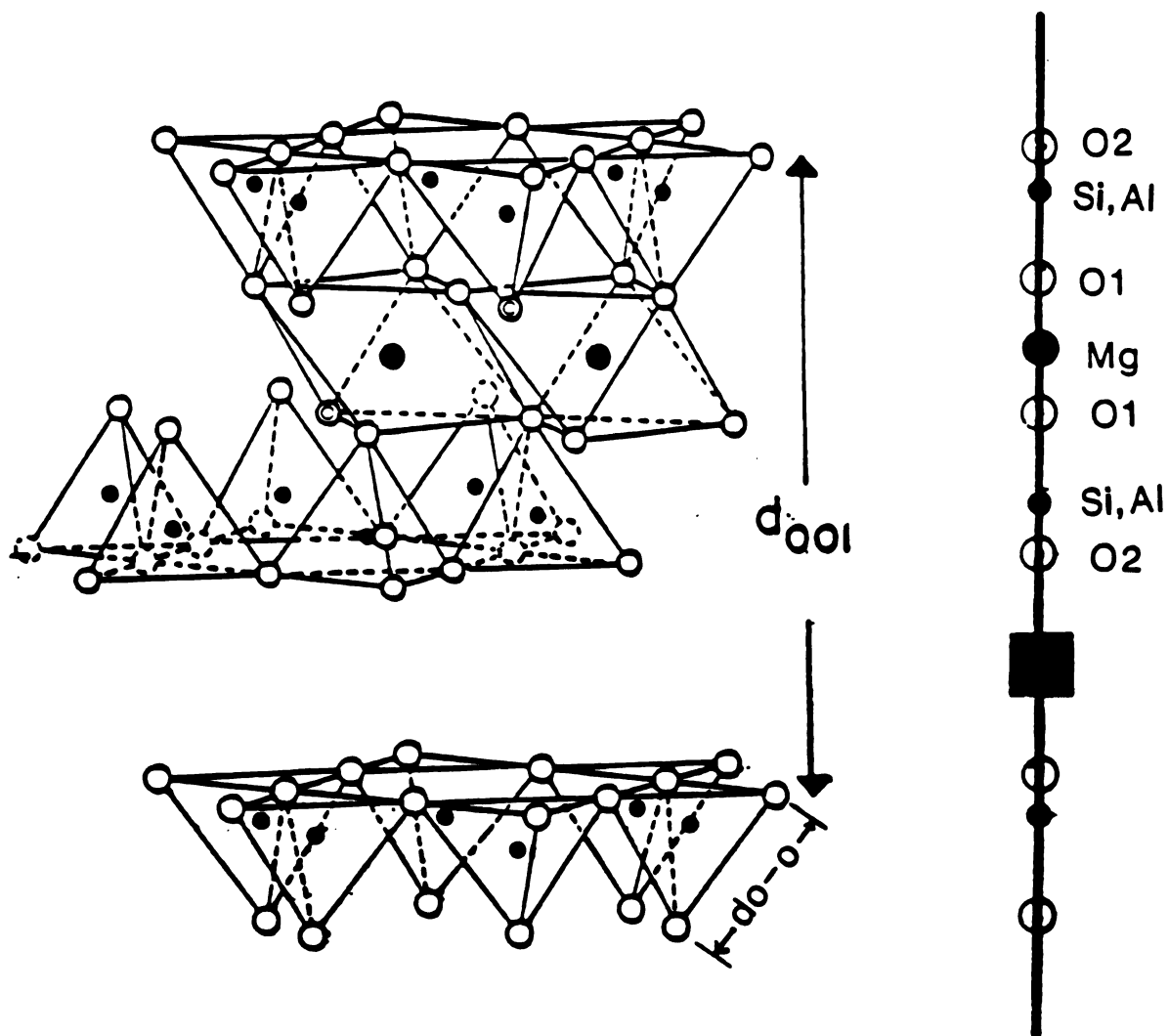


Fig. 5.1 A schematic illustration of the tetrahedral and octahedral sites in a 2:1 layered silicate (after ref [3]). Open circles are oxygen, closed circles are cations in the tetrahedral (Si,Al) and octahedral (Al, Fe, Mg, Li) positions. Hydroxyl groups are represented by double circles. On the right side, the structure seen by  $[00\alpha]$  defraction is shown. The scattering length of each layer is treated as a fitting parameter  $B_1$  and the position of each layer can be derived from the O-O distance  $d_{0-0}$  shown in table 5.1.

process. The concentration dependence of the normalized basal spacing  $d_n(x)$  of pillared vermiculite has been measured<sup>11</sup> for the mixed layer system  $[(\text{CH}_3)_4\text{N}^+]_x[(\text{CH}_3)_3\text{NH}^+]_{1-x}$ -Vermiculite compared with that of  $\text{Cs}_{1-x}\text{Rb}_x$ -Vermiculite. A phenomenological model which relates  $d_n(x)$  to layer rigidity and the binding energies of gallery and defect (non gallery) sites yields excellent fits to the basal spacing data. However, the micromechanism which determines the layer rigidity and the binding energies of the gallery and defect sites remains to be clarified.

Theoretical<sup>10,12</sup> and experimental lattice dynamical studies of intercalated layered silicates have been reported. Gupta, et al.<sup>12</sup> investigated the lattice dynamics of  $\text{Cs}_{1-x}\text{Rb}_x$ -Vermiculite using a force constant model which included both central and angular force and the virtual crystal approximation. Experimentally, Raman scattering studies of the torsional modes of the tetrahedral sheets of  $\text{Cs}_{1-x}\text{Rb}_x$ -Vermiculite<sup>4</sup> and  $[(\text{CH}_3)_3\text{NH}^+]_{1-x}[(\text{CH}_3)_4\text{N}^+]_x$ -Vermiculite<sup>9</sup> have been reported.

From the molecular crystal point of view, the multimethylammonium-vermiculite clays are closely related to multimethylammonium halides. The internal modes of multimethylammonium would, therefore, be expected to be similar for these two type of materials, and their differences would reflect the different environment of the multimethylammonium. Numerous studies have been reported on the vibrational spectra of multimethylammonium halides using IR, Raman and neutron scattering<sup>13-17</sup>.

In this chapter, we will present an elastic neutron scattering study of the structure of trimethylammonium-Vermiculite intercalation compounds. We also address the internal mode properties of the guest species using the inelastic neutron scattering and IR spectroscopic techniques.

## 5.2 EXPERIMENTS

The  $[(\text{CH}_3)_3\text{NH}^+]$ -Vermiculite used in this study was made from natural Mg-Vermiculite from Llano, Texas, by using an ion exchange method. Selected crystals of Mg-V were ground into powder in which the crystallites were a few microns in size.  $[(\text{CH}_3)_3\text{NH}^+]$ -Vermiculite was prepared from this powder by ion exchanging with  $(\text{CH}_3)_3\text{NH}^+$  in the presence of the EDTA anion and then sedimenting the exchanged particles on a glass plate to form a self-supporting oriented film with its c-axis perpendicular to the plate. Water was removed by heating the sample in an oven over 12 hours at a temperature of 100 C°. The large film was cut into many smaller pieces of size about  $2 \times 3 \text{ cm}^2$  and these were mechanically stacked together with their c-axes well aligned. A total weight of the sample was about 3gm. The deuterated sample was prepared with same method using  $(\text{CD}_3)_3\text{ND}^+$  instead of  $(\text{CH}_3)_3\text{NH}^+$ . The typical mosaic spread of the crystallite c-axes for both samples was about 30°.

All neutron scattering results presented here were obtained using a triple axis spectrometer (BT4) located at the National Bureau of Standard Reactor. The elastic scattering was acquired with a fixed energy of 13.7 mev and a collimation of 40'-20'-40'-40'. A one inch PG filter was used in front of an analyzer to remove high order contamination. The diffraction patterns of hydrogenated and deuterated trimethylammonium vermiculite were obtained at room temperature and are shown in Figs. 5.2 and 5.3 respectively.

The vibrational density of states was obtained from the inelastic neutron scattering data using the incoherent approximation, that is, we can replace the dynamic coherent scattering function with its incoherent

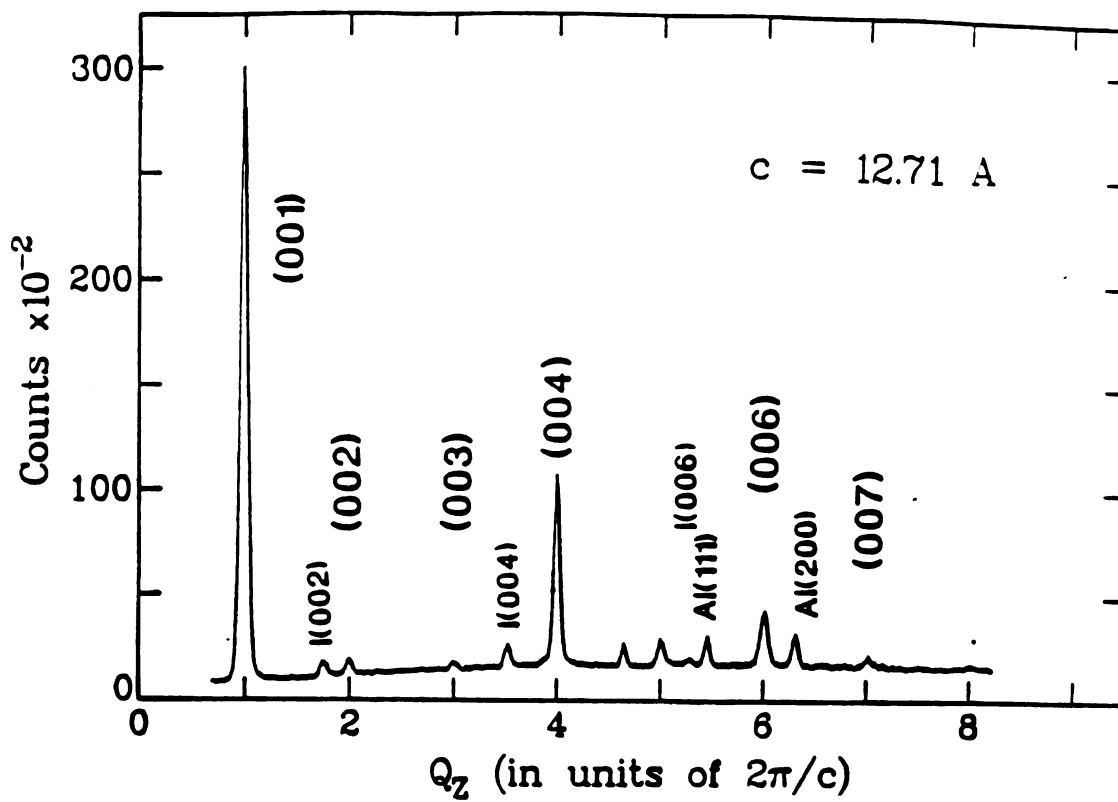


Fig. 5.2 The elastic neutron scattering pattern in the [00 $l$ ] direction for hydrogenated trimethylammonium-vermiculite. The peaks labeled by I(00 $n$ ) are associated with an impurity phase. The horizontal axis is normalized to the first Brillouin zone which corresponds to a lattice period of 12.71Å. Peaks labeled Al are from the aluminum sample holder.

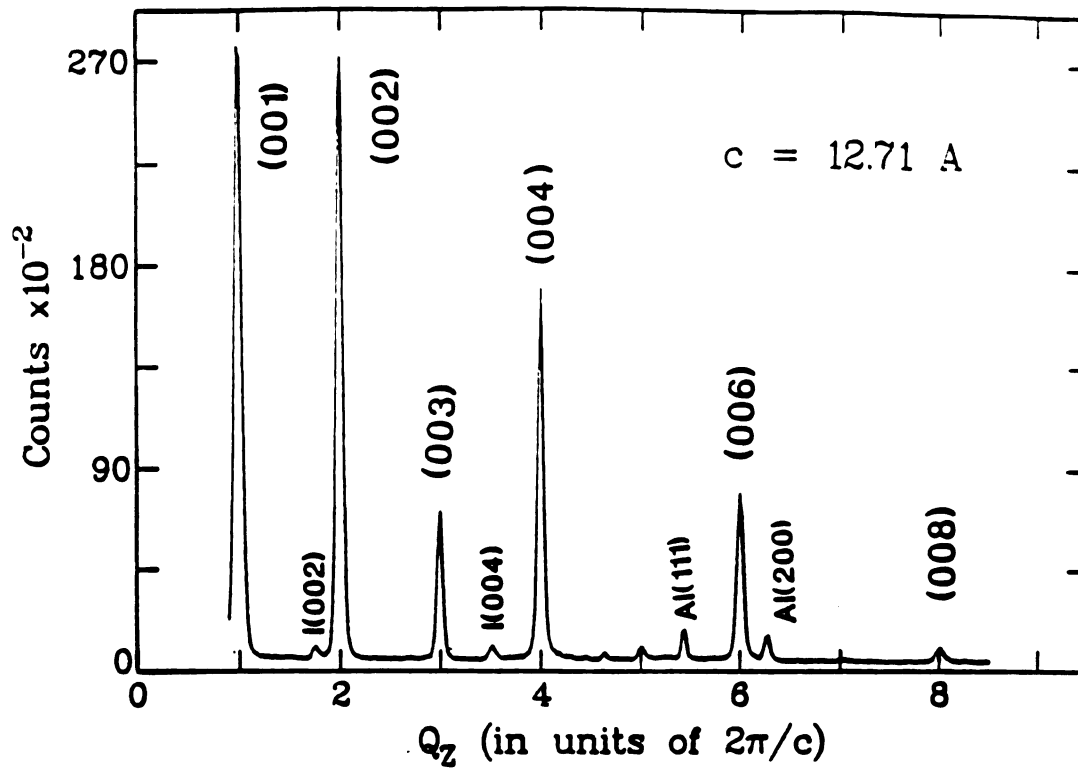


Fig. 5.3 The elastic neutron scattering pattern in the  $[00z]$  direction for deuterated trimethylammonium-vermiculite. The peaks labeled by  $I(00n)$  are associated with an impurity phase. The horizontal axis is normalized to the first Brillouin zone which corresponds to a lattice period of  $12.71\text{\AA}$ . Peaks labeled Al are from the aluminum sample holder.

counterpart<sup>18,19</sup>. Within this formulism, the scattering function is given by<sup>20</sup>

$$\frac{d^2\sigma}{d\Omega dE} \propto \frac{k'}{k} \frac{n(\omega)+1}{\omega} \left\{ \sum_i x_i I_i(\omega) g_i(\omega) \right\}, \quad (5.1)$$

where  $I_i(\omega)$  is defined by

$$I_i(\omega) = \frac{\sigma_i}{m_i} \langle (\vec{Q} \cdot \vec{\epsilon}_i)^2 e^{-2W_i} \rangle. \quad (5.2)$$

Here  $k$  and  $k'$  are the magnitudes of the incident and final neutron wave vectors,  $n(\omega)$  is the Bose occupation factor for a vibrational state of energy  $\omega$ , and  $x_i$ ,  $m_i$ ,  $\sigma_i$ , and  $\epsilon_i$  are the atomic concentration, nuclear mass, total scattering cross section and displacement vector of the  $i$ th atomic species, respectively;  $W_i$  is the Debye-Waller factor, which can be assumed to be negligible at the sample temperatures in this study. The angle brackets indicate an average over all sites of type  $i$  and over all modes of energy  $\omega$ . Finally,  $g(\omega_i)$  represents the density states for the  $i$ th type of atom, which is defined by

$$g(\omega_i) = \sum_{\alpha} \delta(\omega - \omega_{i,\alpha}), \quad (5.3)$$

where the sum is taken over all normal modes. Therefore, the scattering does contain information about the vibrational density of states; however, the contributions from different species are weighted by the value of  $I_i(\omega)$ . From Eqs. (5.1) and (5.2), we see that the scattering cross section is proportional to  $x_i \sigma_i / m_i$ , thus, for our system the scattering from hydrogen will be dominant in the spectra.

The vibrational spectra were obtained using a Be-graphite-Be filter analyzer assembly (the "trash" analyzer). The analyzer was placed at a scattering angle of  $90^\circ$  allowing  $Q$  to vary as a function of energy. For the energy range from 20 to 40 meV, pyrolytic graphite [(002) reflection] was used as a monochromator. The collimation was  $40'-20'-20'-40'$ , yielding a

resolution of about 2-3 meV. At large energy transfer ( $35 \text{ meV} \geq E \geq 140 \text{ meV}$ ), a Cu monochromator [(220) reflection] was used with a collimation of 60'-40'-20'-40', yielding a energy resolution of about 2-5 meV. Since the samples have a very large mosaic, out-of-plane vibrational mode measurements, i.e.,  $\vec{Q}$  parallel to the c-axis, were made with the sample fixed with the c-axis parallel to the incident beam. For the in-planar modes, i.e., with  $\vec{Q}$  perpendicular to the c-axis, it was rotated by 90°. The spectra for both samples were obtained at liquid nitrogen temperature.

The contribution to the scattering from fast neutrons was measured and subtracted. The scattering from the sample can was found to be negligible and the multiphonon and multiple scattering were sufficiently featureless to be ignored. A single vibrational density of state was obtained by scaling the two different energy ranges according to the overlapping energy regions. The "trash" analyzer spectrum of hydrogenated trimethylammonium with  $\vec{Q}$  perpendicular to the c-axis of vermiculite is given in Fig. 5.4 and that with  $\vec{Q}$  parallel to the c-axis is given in Fig. 5.5. The patterns for deuterated trimethylammonium-vermiculite are given in Figs. 5.6 and 5.7 for  $\vec{Q}$  perpendicular to the c-axis and  $\vec{Q}$  parallel to the c-axis respectively.

The IR spectra were obtained on a IBM PC-AT based IR/44 infrared spectrometer. The peak positions are given by a built in data processor. The IR spectra of the hydrogenated and deuterated samples are shown in Fig. 5.8. All IR data were collected at room temperature.

### 5.3 DISCUSSIONS

#### Elastic scattering

The elastic neutron scattering pattern along the [001] direction for both the deuterated and hydrogenated are shown in Fig. 5.2 and Fig. 5.3,

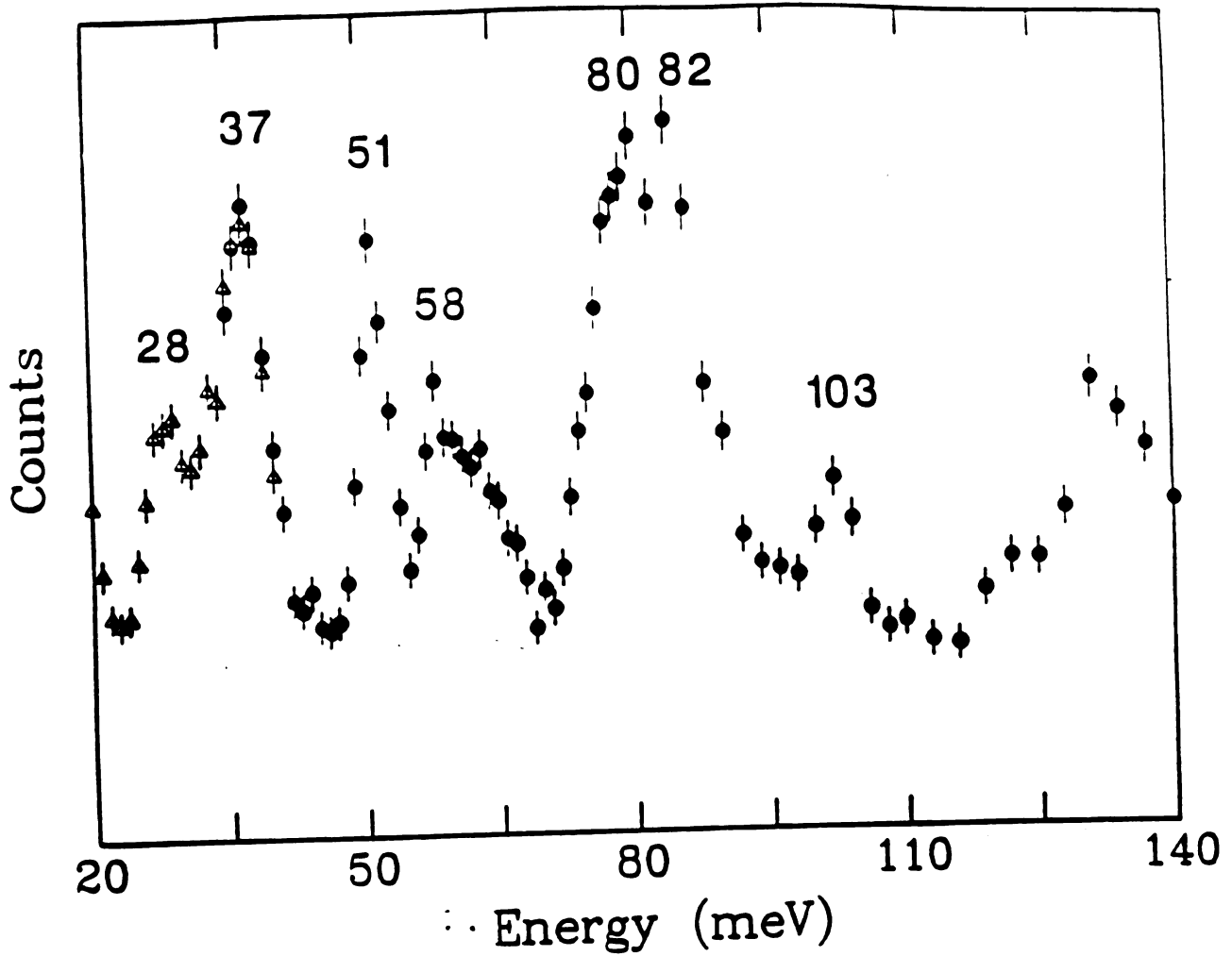


Fig. 5.4 The spectrum of vibrational density of state of hydrogenated trimethyl ammonium vermiculite with scattering vector  $\vec{Q}$  parallel to the basal plane of the silicate sheet.

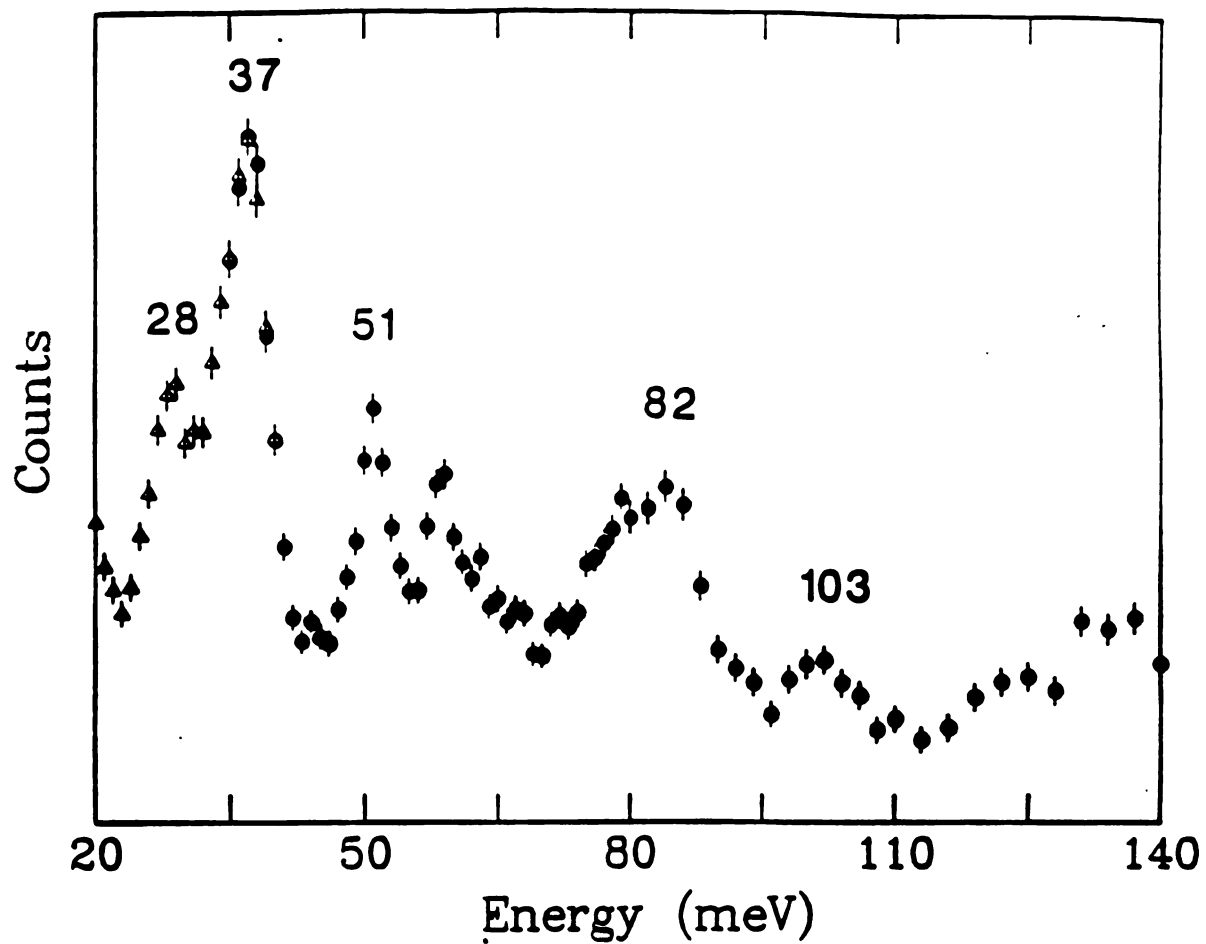


Fig. 5.5 The spectrum of vibrational density of state of hydrogenated trimethyl ammonium vermiculite with scattering vector  $\vec{Q}$  perpendicular to the basal plane of the silicate sheet.

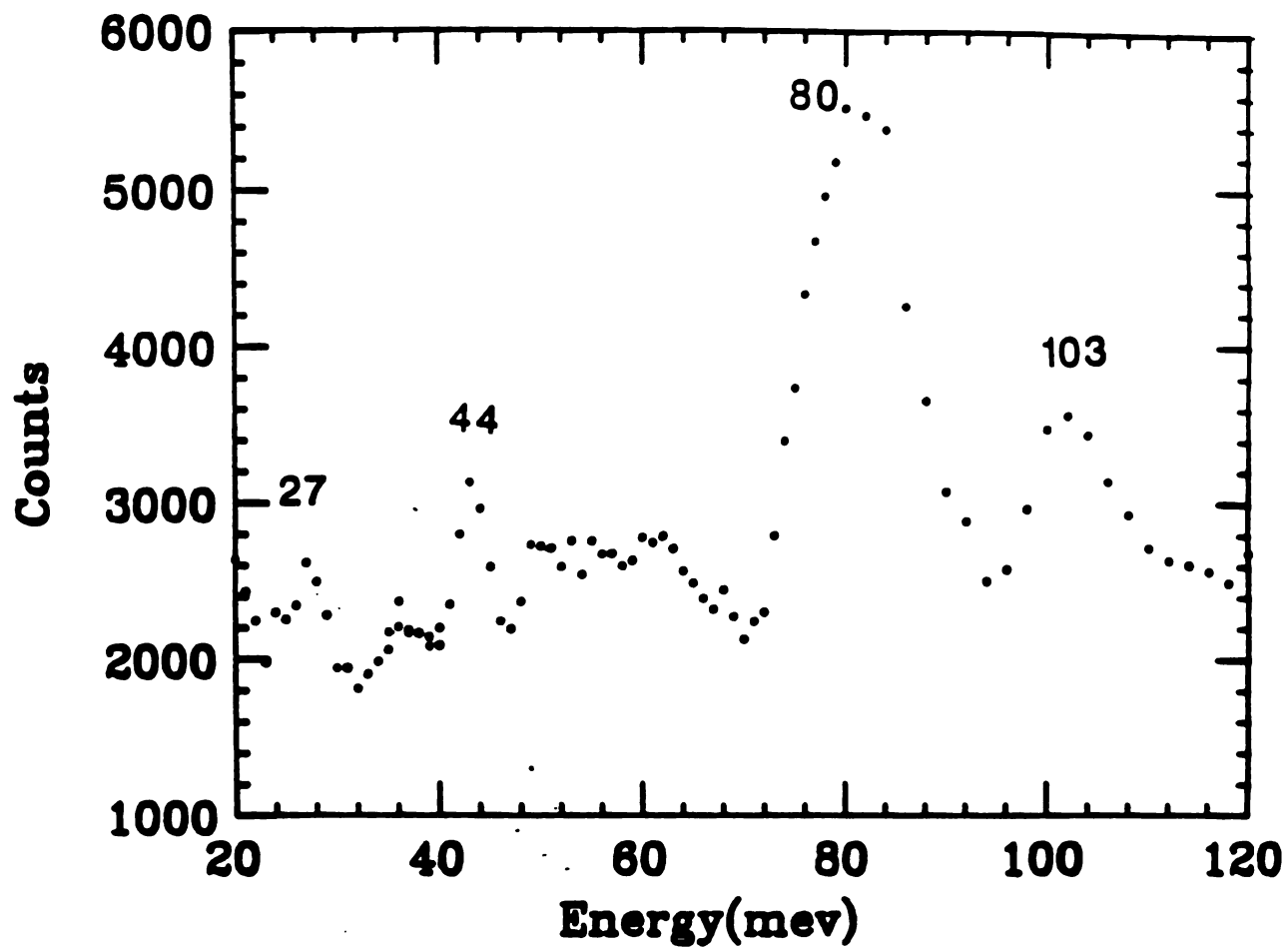


Fig. 5.6 The spectrum of vibrational density of state of deuterated trimethyl ammonium vermiculite with scattering vector  $\vec{Q}$  parallel to the basal plane of the silicate sheet.



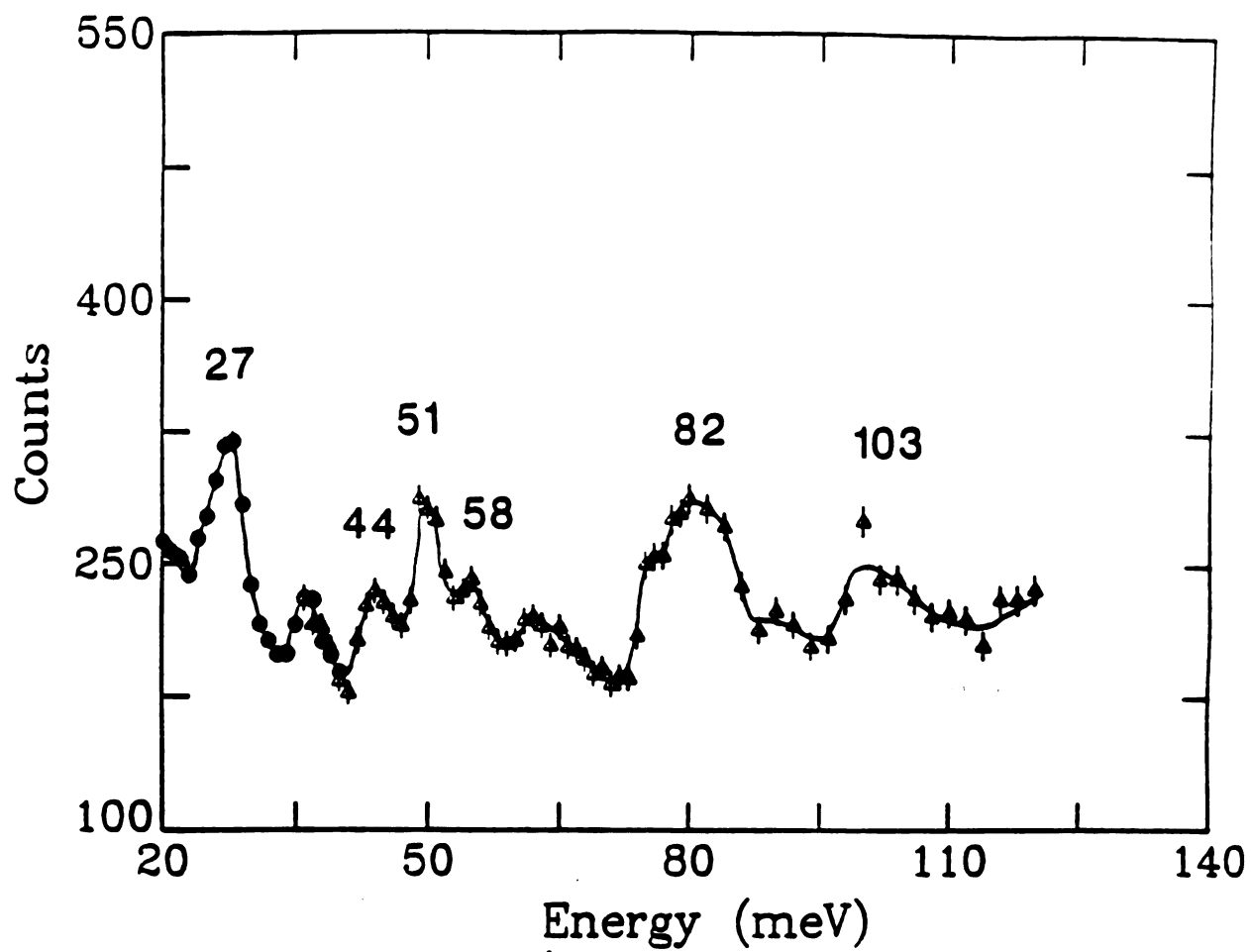


Fig. 5.7 The spectrum of vibrational density of state of deuterated trimethyl ammonium vermiculite with scattering vector  $\vec{Q}$  perpendicular to the basal plane of the silicate sheet.

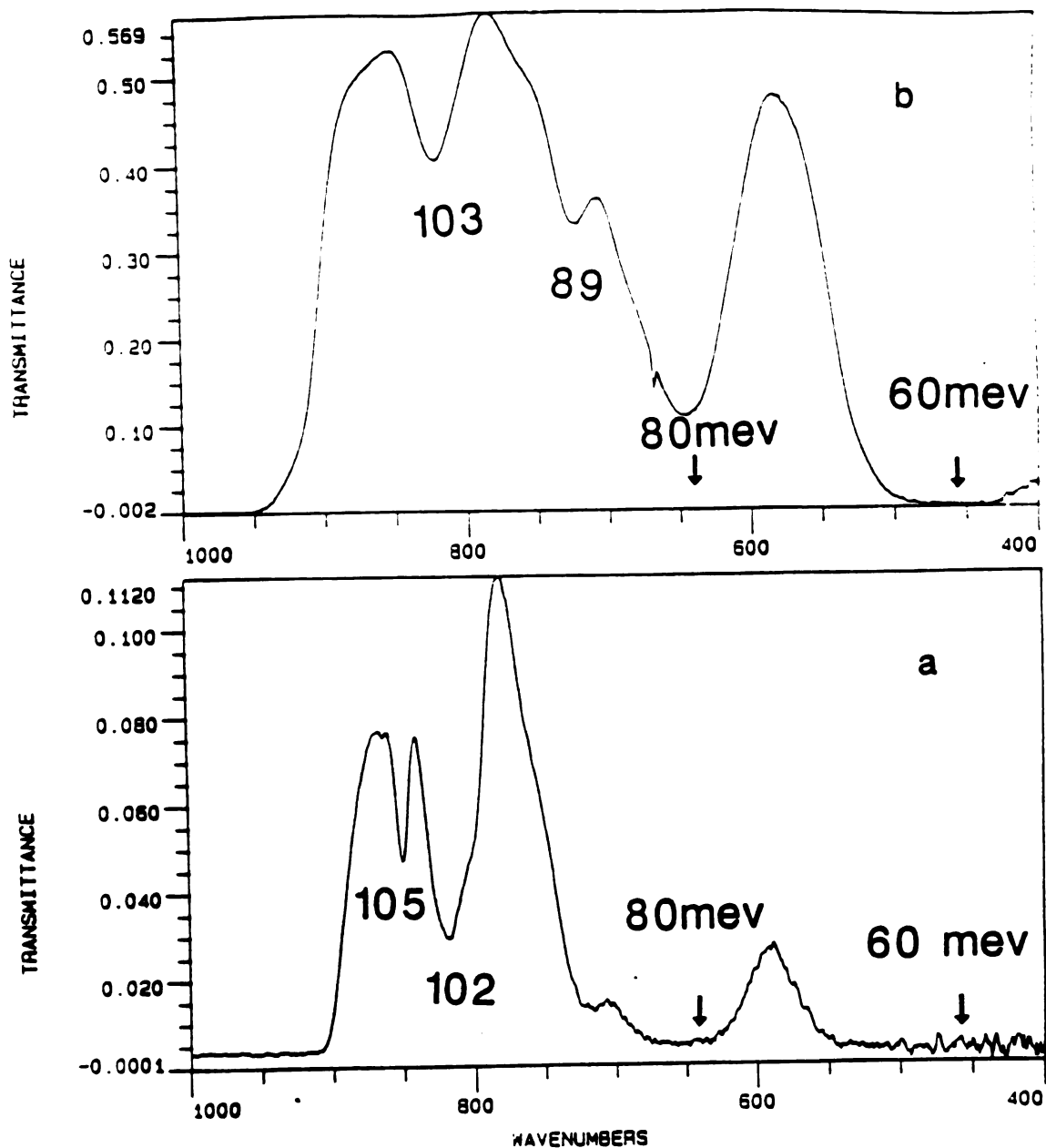


Fig. 5.8 The IR spectrum for deuterated (a) and hydrogenated (b) trimethyl ammonium vermiculite at room temperature. The adsorption band around 60 meV ( $484 \text{ cm}^{-1}$ ) is associated with the brucite layer optical modes, the band around 80 meV ( $646 \text{ cm}^{-1}$ ) is due to the inplane modes of the silicate sheet.

re

re

of

pe

l.

m

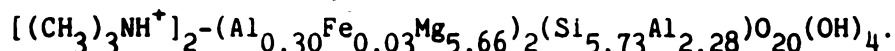
t

v

v

respectively. The horizontal-axes of these diagrams are normalized to the reciprocal lattice in the c-direction which corresponds to a repeat distance of 12.71 Å. The peaks at 5.4 and 6.30 are identified as the (111) and (200) peaks from the sample can. Notice that there is another set of Bragg peaks labeled as I(00n) which refers to an impurity phase from the original clay mineral<sup>11</sup>. The peak at 4.6 has not yet been identified, but is probably due to an inplanar peak leaking into [001] direction since our samples have a very large mosaic. All Bragg peaks have an instrumental resolution limited width indicating that the layers are well ordered in the c-direction. In order to obtain c-axis structural information, the structural form factor is calculated according to the structure shown in Fig. 5.1.

The unit cell composition of trimethylammonium-vermiculite is



The form factor can be written as

$$F(Q) = \sum_{i,j} b_j n_{ij} \exp(QR_i)$$

where the sum is taken over all layers in a unit cell,  $n_{ij}$  is the number of atoms of type  $j$  in  $i$ th layer,  $b_j$  is the scattering length of the type  $j$  atom and  $R_i$  is the distance of the  $i^{\text{th}}$  layer from the origin. In this calculation the Mg layer was chosen to be the origin.

Let  $B_i = \sum_j b_j n_{ij}$  which represents the total scattering length of layer  $i$  in a unit cell. Then

$$F(Q) = \sum_i B_i \exp(QR_i).$$

The  $B_i$  and  $R_i$  are listed in Table 5.1 for the ideal clay structure. The integrated intensities of the Bragg peaks are related to the form factor as follows



Table 5.1 A comparison between the calculated total scattering lengths  $B_i$  of layer  $i$  in a unit cell of the ideal structure shown in Fig. 5.1 and that derived from a fit to the data of Figs 5.2 and 5.3 using a model described in the text.

$B_i$	Calculation	fit
$B_{Mg}$	6.15	5.90
$B_{O1}$	2.73	2.83
$B_{Si,Al}$	1.60	1.89
$B_{O2}$	3.48	3.37
$B_{I(H)}$	-1.63	2.63
$B_{I(D)}$	19.19	8.50
$R_I$	1.50	1.54
$d_{o-o}$	2.64	2.64

All  $B_i$ 's are in units of  $10^{-12}$  cm,  $R_I$  and  $d_{o-o}$  are in units of Å.

he

this

we

Since

re

has

sph

mod

the

we

fi

ti

a

s

i

n

F

t

c

c

.

$$I_{\text{int}}(Q) \propto |F(Q)|^2. \quad (5.2)$$

The integrated intensities were corrected for the Lorentz factor, which in this case is approximately<sup>21</sup>

$$L \propto \frac{1}{\sin\theta} = \frac{A}{Q} \quad (5.3)$$

where A is a factor independent of Q and can be treated as scaling factor. Since the trimethylammonium is expected to be rotating in the gallery at room temperature<sup>17</sup>, it is not a point scatterer and a molecular form factor has to be used in the calculation. We treat the trimethylammonium as a spherical molecule (many other models have been tried and the spherical model is the best choice) with a radius of  $R_I$  (see Table 5.1). Therefore the molecular form factor can be written as

$$F(Q) = B_{\text{TMA}} \frac{3j_1(QR_I)}{QR_I} \quad (5.4)$$

where  $R_I$  is the radius of trimethylammonium.

However, the calculation according to this ideal clay structure cannot fit the observed experimental results, therefore we treat the  $B_i$ 's as fitting parameters. Since the fitting parameters are correlated for deuterated and hydrogenated samples, these two sets of data have been fitted simultaneously<sup>21</sup>.

The best fit to the integrated intensities of the Bragg peaks are shown in Figs. 5.9a and 5.9b for the deuterated and hydrogenated sample, respectively. The fitting parameters are also given in Table 5.1 for comparison with the ideal structure. As can be seen from Figs. 5.9a and 5.9b, the fits are reasonably good, and the parameters derived from these fits are comparable to those for the ideal structure except for the intercalant concentration. This deviation can be explained by the assumption that the trimethylammonium has not fully substituted the ions which were originally

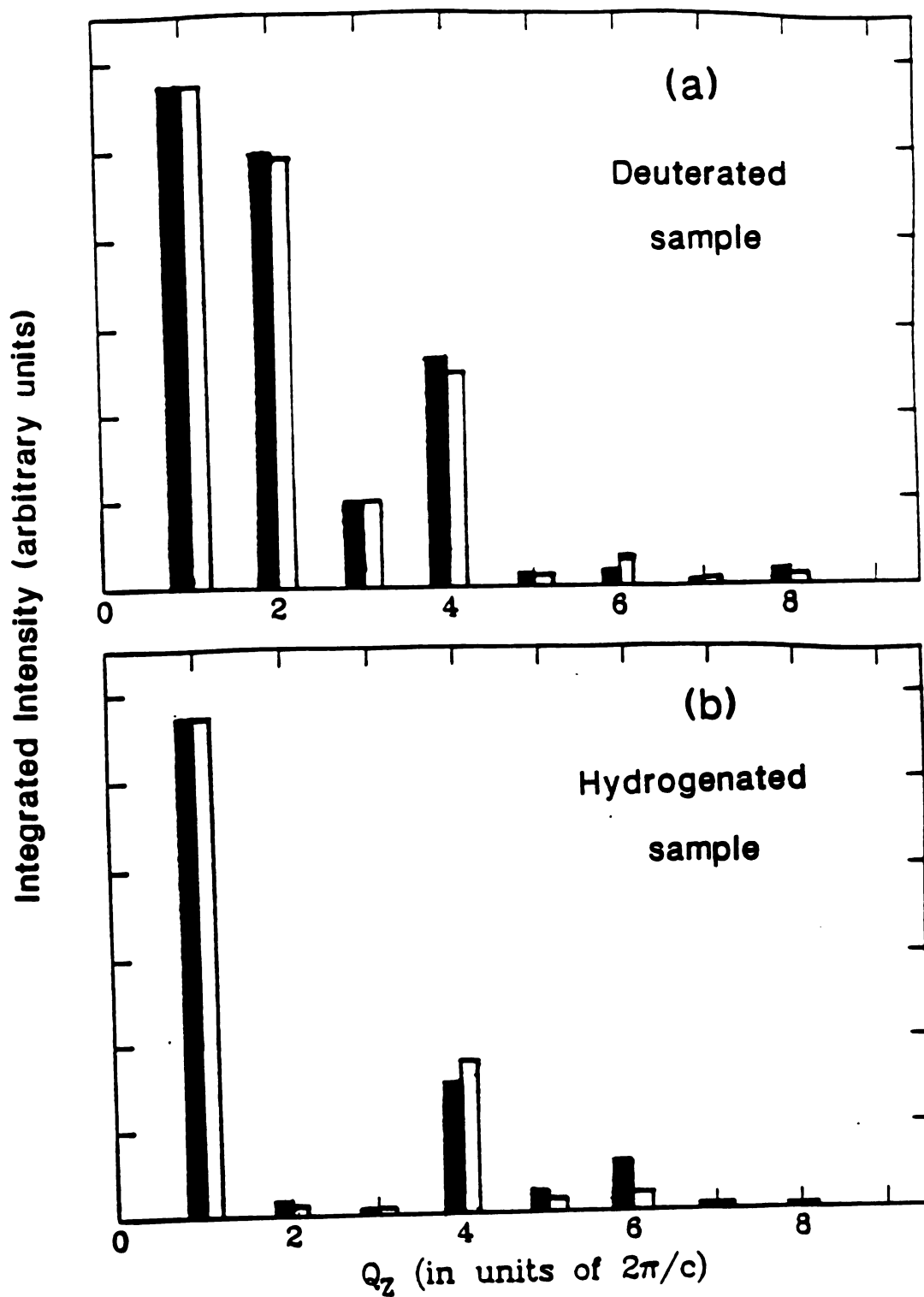


Fig. 5.9 A comparison between the integrated intensities obtained by the neutron scattering measurements shown in Figs. 5.2 and 5.3 (solid bar) and that from the best fit (open bar) using a model discussed in the text.

in the gallery. The percentage  $x$  of trimethylammonium intercalated into the clay gallery and the total scattering length of remaining ion  $B_{\text{to-rem}}$  in a unit cell can be found by solving the following equations

$$B_{\text{to-rem}} + B_{\text{H,calc}} x = B_{\text{H,Fit}}$$

$$B_{\text{to-rem}} + B_{\text{D,calc}} x = B_{\text{D,Fit}}$$

i.e.

(5.5)

$$B_{\text{to-rem}} + 2 \times (-0.815)x = 2.63$$

$$B_{\text{to-rem}} + 2 \times 9.59x = 8.50$$

These equations give a solution  $B_{\text{to-rem}} = 3.1$  and  $x = 28\%$ . This result is consistent with the recent x-ray experiment and calculation that the percentage of nongallery sites in trimethylammonium is 70%<sup>11</sup>.  $B_{\text{to-rem}} = 3.1$  corresponds to about one Mg plus one Fe ion remaining in the gallery, which is very likely the case. Thus we conclude that the concentration of trimethylammonium is about 30%, and that the ion exchange is not complete.

#### Inelastic scattering

The spectra of the hydrogenated trimethylammonium-vermiculite for two  $\vec{Q}$  directions are given in Figs. 5.4 and 5.5. In comparing them we see that the peaks at 28 meV and 37 meV are isotropic whereas the peaks in the rest of the spectrum are mostly associated with inplane modes. In fact, some of the peaks for  $\vec{Q}$  parallel to the c-axis (Fig. 5.5) are simply the leakage from the  $\vec{Q}$  perpendicular configuration into  $\vec{Q}$  parallel. This can be shown simply as follows. The scattering intensity is proportional to  $(\vec{Q} \cdot \vec{e})^2$  where  $\vec{e}$  is the polarization direction of the mode. Assume that the mosaic has a Gaussian distribution and that the mode measured is totally inplane. We can calculate the ratio,  $R$ , of the peak intensities for the two directions.

$$R = \frac{\left(\frac{d\sigma}{d\Omega}\right)_{\parallel}}{\left(\frac{d\sigma}{d\Omega}\right)_{\perp}} = \frac{\int \sin^2\theta \exp(-\theta^2/\theta_d^2) d\theta}{\int \cos^2\theta \exp(-\theta^2/\theta_d^2) d\theta} \quad (5.6)$$

For a mosaic of  $35^\circ$ ,  $\theta_d = 0.734$  and we obtain  $R = 0.3$ . This value is about the same as the measured peak intensity ratio for all peaks above 50 meV. So we conclude that the peaks above 50 meV in the  $\vec{Q}$  parallel spectrum are indeed leakage peaks and the bands at 80 meV and 102 meV are from inplane mode. Moreover, the bands around 51 meV are partially polarized.

By comparing the spectra of the hydrogenated and deuterated samples, we see that the peaks at 28 meV, 37 meV, 51 meV and 58 meV are absent from the deuterated sample indicating that those peaks are associated with trimethylammonium. Since the peaks above 80 meV are present in both samples they are associated with the vermiculite host. The broad peak at 27 meV in Fig. 5.7 is of the same origin as the peak at 37 meV in Fig. 5.5 but is isotope down shifted due to the heavier deuteron mass. The peak at 44 meV in Fig. 5.7 is also isotope down shifted from the 58 meV peak in Fig. 5.4. The peaks at 80 meV and 102 meV are also observed in the IR measurements for both hydrogenated and deuterated samples. The fact that their positions are independent of the isotope indicates that they are associated with the host. Until now, we have identified the internal modes of the trimethylammonium guest in terms of their nonhost origin and their polarization.

Since the intramolecular interaction is much stronger than the intermolecular interaction, the intramolecular modes are effected very weakly by the coupling between different molecule. Therefore, a comparison with other solids which contain trimethylammonium will be helpful to identify the nature of the internal modes of the ion in a clay host. The trimethylammonium ion has  $C_{3v}$  point group symmetry as do the methyl groups from which it is composed. The internal modes of this ion have been heavily studied in the

ionic salts which it forms<sup>13</sup>. The methyl groups are known to execute torsional oscillations about their threefold axis with a characteristic energy of typically 30 meV. In addition, the torsional mode coupling between these methyl group rotors gives rise to a 5 meV splitting of the torsional mode into components with a relative intensity ratio of 1/2 for the low energy band relative to the high energy band. We have observed a similar effect in the inelastic neutron scattering spectra of  $(\text{CH}_3)_3\text{NH}^+$ -vermiculite. Notice that the 28 and 37 meV bands of hydrogenated trimethylammonium vermiculite (see Figs. 5.4 and 5.5) have the requisite average energy  $\approx 30$  meV and a 1:2 intensity ratio for us to confidently assign them to the torsional split mode. Specifically, we assign the 28 meV band as the  $\nu(\text{A}_2)$  torsion mode with  $\text{A}_2$  symmetry and the 37 meV band as another torsion mode  $\nu(\text{E})$  with E symmetry. Again by comparison with the salts of trimethylammonium, we can also assign other (non torsional) modes. The 51 meV band is assigned as the  $\nu(\text{E}, \delta\text{NC}_3)$  bending mode of the N-C bonds with E symmetry and the peak at 58 meV is assigned as the  $\nu(\text{A}_1, \delta\text{NC}_3)$  bending mode. These trimethylammonium modes have also been reported by several authors for other materials<sup>13-15</sup>. A summary of the above specified mode assignments is given in Table 5.2. As can be seen, the splitting between the torsional modes increases considerably in trimethylammonium (TMA)-Vermiculite relative to that in the trimethylammonium halides. The splitting comes from the coupling of top-top interaction of the methyl groups and thus reflects the strength of this interaction. The enhancement of the splitting in vermiculite could be caused by the following reasons: first, the intercalated trimethylammonium has changed its shape so that the top-top distance is effectively reduced and this in turn increases the coupling; second, the indirect interaction mediated by the clay layer has

Table 5.2 A comparison of the internal modes of trimethylammonium in different materials. The splitting of the torsional modes in trimethylammonium-vermiculite has increased relative to that in trimethylammonium salts.

	torsional modes		bending modes		Torsional mode splitting
	$\nu(A_2)$	$\nu(E)$	$\nu(E, \delta NC_3)$	$\nu(A_1, \delta NC_3)$	$\nu(E) - \nu(A_2)$
This work $(CH_3)_3NH^+ - V$	28.0	37.0	51.0	58.0	9.0
$(CH_3)_3NHCl^a$	30.9	36.4	49.3	57.7	5.5
$(CH_3)_3NHCl^b$	32.6	37.7	50.1		5.1

<sup>a</sup> from Ref. 13, <sup>b</sup> from Ref. 16.

increased. Whatever its origin, it is surprising that these interactions are stronger in the clay intercalation compounds than in the halide salts.

Since the lack of the detailed mode calculations on trimethylammonium-vermiculite have not yet been carried out, we draw insight from mode calculations on the alkali vermiculites<sup>12</sup>. According to these calculations, the bands near 60 meV are due to the optical modes of brucite layer of the host and the bands above 80 meV are assigned to inplane optical modes of the silicate sheet. The large intensity of these peaks in our spectra is a consequence of the fact that the oxygen layers contain OH groups which enhance the scattering cross section.

The IR spectra for both the deuterated and hydrogenated samples in the same energy range as the neutron measurements are shown in Fig. 5.8. The absorption band near 65 meV correspond to the inelastic neutron scattering peaks around 60-70 meV which are associated with the brucite layer modes. Another strong absorption band from 80-90 meV also corresponds to peaks around 80-90 meV in the neutron spectra. These bands are due to the inplane optical modes of the silicate sheet. The peak at 102 meV in the neutron spectra is also observed in the IR measurement. The two features at 102 and 105 meV in the IR spectra correspond to the broad peak at 103 meV in Figs. 5.5 and 5.6, but are not resolved due to the poor resolution of neutron spectra in that energy range.

#### 5.4 Conclusions

The elastic neutron scattering study shows that the trimethylammonium-vermiculite clay has a c-axis repeat distance of 12.71 Å. However, its structure has not been determined unambiguously. There is evidence that trimethylammonium has only partially substituted (30% of full exchange) for the cations in the gallery of natural clay host. In order to determine the structure unambiguously, additional Bragg peaks at higher Q values are required. The inelastic neutron scattering data shows that the internal modes of trimethylammonium in vermiculite are consistent with the measurements for trimethylammonium halides, but the top-top coupling interaction of the methyl groups is stronger in vermiculite than in halide salts. In addition, the host modes determined from inelastic neutron scattering data are in qualitative agreement with theoretical calculations.

References

1. S.A. Solin, in Intercalation in Layered Matials ed by M.S. Dresselhaus, (Plenum, New York, 1986) P.145.
2. R.E. Grimm, Clay Minerology, (McGraw Hill, New York, 1968).
3. T.J. Pinnavaia, Science 220, 365 (1983).
4. B.R. York, S.A. Solin, N. Wada, R. Raythatha, I.D. Johnson, and T. J. Pinnavaia, Solid State Comm., 54, 475 (1985).
5. S. Lee, H. Kim, S.A. Solin, and T.J. Pinnavaia, Chem. Phys. of Intercalation, (A.P.Legrand, ed.), Nato ASI, 1987, (to be published).
6. N. Wada, R. Raythatha, and S. Minomura, Solid State Comm., 63, 783 (1987).
7. R. Zallen, The Physics of Amorphous Solids, Wiley, New York, 1983, Chap. 4.
8. P. Wong, J. Howard, J. Lin, Phys. Rev. Lett. 57, 637 (1986).
9. S.A. Solin, H.X. Jiang, H. Kim, and T.J. Pinnevaia, to be published.
10. W. Jin, S.D. Mahanti, S.A. Solin and H.C. Gupta, Mat. Res. Soc. Symp. Proc. Vol. 111. (1988).
11. H. Kim, W. Jin, S. Lee, P. Zhou, T.J. Pinnavaia, S.D. Mahanti, and S.A. Solin, Phys. Rev. Lett. 60, 2168 (1987).
12. H.C. Gupta, S.D. Mahanti, and S.A. Solin, Physics and Chemistry of Minerals, to be published.
13. C.I. Ratcliffe and T.C. Waddington, J. Chem. Soc. Faraday Transactiona 2, 72, 1935 (1976).
14. Y. Imai, K. Aida, Ken-ichi Sohma, F. Watari, Polyhedron, Vol.1, No.4, 397 (1982).
15. P.V. Houg and M. Schlaak, Chem. Phys. Lett. 27, 111 (1974).

16. M. Sclaak, M. Couzi, J.C. Lassegues, W. Drexel, Chem. Phys. Lett. 45, 111 (1977).
17. M. Sclaak, Mol. Phys. 33 125 (1977).
18. M.M. Bredov, B.A. Kotov, N.M. Okuneva, V.S. Oskotskii, and A.L. Shakh-Bugadov, Fiz. Tverd. Tela. (Leningrad) 9, 287 (1967) [Sov. Phys. Solid State 9, 214 (1967)].
19. V.S. Oskotskii, Fiz. Tverd. Tela. (Leningrad) 9, 550 (1967) [Sov. Phys. Solid State 9, 420 (1967)].
20. N. Lustig, J.S. Lannin, J.M. Carpenter, and R. Hasegawa, Phys. Rev. B32, 2778 (1985).
21. J.D. Axe and J.B. Hastings, Acta Cryst. A39, 593 (1983).
22. Functions  $f(x, \vec{a}, \vec{B})$  and  $g(x, \vec{a}, \vec{Y})$  have same fitting parameters  $\vec{a}$ , and the best fit of  $f(x, \vec{a}, \vec{B})$  to data  $(f_i, x_i)$  ( $i=1, 2, \dots, n$ ) gives fitting parameters  $\vec{a}_1$ . Usually,  $g(x, \vec{a}_1, \vec{Y})$  can not fit data  $(g_i, x_i)$  ( $i=1, \dots, n$ ) no matter what  $\vec{Y}$  used. In this case, simultaneously fit is needed (varying one set of  $\vec{a}$  to fit both functions instead of fitting them sequentially).